AD-A194 961 FINITE-DIFFERENCE SIMULATIONS OF RAYLEIGH-WAVE 1/2
SCATTERING BY SHALLOW HETE..(U) TELEDYNE GEOTECH
ALEXANDRIA VA ALEXANDRIA LABS K L MCLAUGHLIN ET AL.
UNCLASSIFIED NOV 87 TGAL-87-02 AFGL-TR-87-0322 F/G 8/11 NL

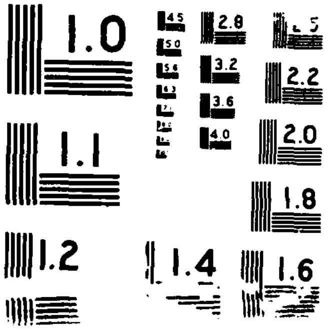
1.0
4.5
5.0
5.6
2.8
3.2
3.6
4.0
2.5
2.2
2.0
1.1
1.8
1.2
1.4
1.6

①

AFGL-TR-87-0322 TGAL-87-02

FINITE-DIFFERENCE SIMULATIONS OF RAYLEIGH-WAVE SCATTERING BY SHALLOW HETEROGENEITY

Keith Lynn McLaughlin
Rong-Song Jih

Teledyne Geotech Alexandria Laboratories
314 Montgomery Street
Alexandria, VA 22314-1581

November 1987

Scientific Report #1

APPROVED FOR PUBLIC RELEASE; DISTRIBUTION UNLIMITED

AIR FORCE GEOPHYSICS LABORATORY
AIR FORCE SYSTEMS COMMAND
UNITED STATES AIR FORCE
HANSCOM AIR FORCE BASE, MASSACHUSETTS 01731

Sponsored by:
Defense Advanced Research Projects Agency
Nuclear Monitoring Research Office
DARPA Order No. 5307

Monitored by:
Air Force Geophysics Laboratory
Under Contract No. F19628-86-C-0054

"This technical report has been reviewed and is approved for publication."

JAMES F. LEWKOWICZ
Contract Manager

HENRY A. OSSING
Chief, Solid Earth Geophysics Branch

FOR THE COMMANDER

DONALD H. ECKHARDT
Director
Earth Sciences Division

This report has been reviewed by the ESD Public Affairs Office (PA) and is releasable to the National Technical Information Service (NTIS).

Qualified requestors may obtain additional copies from the Defense Technical Information Center. All others should apply to the National Technical Information Service.

If your address has changed, or if you wish to be removed from the mailing list, or if the addressee is no longer employed by your organization, please notify AFGL/DAA, Hanscom AFB, MA 01731. This will assist us in maintaining a current mailing list.

Do not return copies of this report unless contractual obligations or notices on a specific document requires that it be returned.

Unclassified
SECURITY CLASSIFICATION OF THIS PAGE

REPORT DOCUMENTATION PAGE

Form Approved
OMB No 0704-0188
Exp Date Jun 30, 1986

1a REPORT SECURITY CLASSIFICATION Unclassified	1b RESTRICTIVE MARKINGS
2a SECURITY CLASSIFICATION AUTHORITY	3 DISTRIBUTION/AVAILABILITY OF REPORT Approved for public release; Distribution unlimited.
2b DECLASSIFICATION/DOWNGRADING SCHEDULE	
4 PERFORMING ORGANIZATION REPORT NUMBER(S) TGAL-87-02	5. MONITORING ORGANIZATION REPORT NUMBER(S) AFGL-TR-87-0322

6a NAME OF PERFORMING ORGANIZATION Teledyne Geotech	6b OFFICE SYMBOL (If applicable) TGAL	7a NAME OF MONITORING ORGANIZATION Air Force Geophysics Laboratory
6c. ADDRESS (City, State, and ZIP Code) 314 Montgomery Street Alexandria, VA 22314		7b ADDRESS (City, State, and ZIP Code) Hanscom AFB, MA 01731-5000
8a NAME OF FUNDING/SPONSORING ORGANIZATION Air Force Geophysics Laboratory	8b OFFICE SYMBOL (If applicable) DSO/GSD	9. PROCUREMENT INSTRUMENT IDENTIFICATION NUMBER F19628-86-C-0054

8c. ADDRESS (City, State, and ZIP Code)
Hanscom AFB, MA 01731-5000

10 SOURCE OF FUNDING NUMBERS

PROGRAM ELEMENT NO	PROJECT NO.	TASK NO	WORK UNIT ACCESSION NO
62714E	6A10	DA	BC

11 TITLE (Include Security Classification) Finite-Difference Simulations of Rayleigh-wave Scattering by Shallow Heterogeneity

12. PERSONAL AUTHOR(S) K. L. McLaughlin and R.-S. Jih

13a TYPE OF REPORT	13b. TIME COVERED	14. DATE OF REPORT (Year, Month, Day)	15 PAGE COUNT
Scientific #1	FROM Feb 86 TO Feb 88	November 1987	108

16 SUPPLEMENTARY NOTATION

17 COSATI CODES

FIELD	GROUP	SUB-GROUP

18 SUBJECT TERMS (Continue on reverse if necessary and identify by block number)

Finite Difference, Rayleigh Wave, Heterogeneity, Scattering, Attenuation, Coda

19 ABSTRACT (Continue on reverse if necessary and identify by block number)

Rayleigh waves normally incident upon 2-D shallow heterogeneity are simulated by the linear finite-difference method to study attenuation, transmission, and reflection of Rayleigh waves and to measure the Rayleigh-to-P and -SV body wave conversion. Transmission, reflection, and scattering depend on the depth, average scale size of the heterogeneity and the amplitude of the spatial fluctuation of velocity. As expected, larger spatial variation in velocity attenuates Rayleigh waves more than smooth media and the attenuation is roughly proportional to the variance of the velocity fluctuation. The attenuation and scattering due to shallow heterogeneity is weaker than attenuation due to moderately rough topography.

20 DISTRIBUTION/AVAILABILITY OF ABSTRACT ☐ UNCLASSIFIED/UNLIMITED ☐ SAME AS RPT ☐ DTIC USERS	21. ABSTRACT SECURITY CLASSIFICATION Unclassified	
22a NAME OF RESPONSIBLE INDIVIDUAL James F. Lewkowicz	22b TELEPHONE (Include Area Code) (617) 377-3028	22c OFFICE SYMBOL AFGL/LWH

DD FORM 1473, 84 MAR

83 APR edition may be used until exhausted
All other editions are obsolete

SECURITY CLASSIFICATION OF THIS PAGE
Unclassified

(19. continued)

Scattered body wave energy is studied as a function of frequency, scattering angle, and wave type (P or SV). Attenuation of Rayleigh waves by scattering from 2-D shallow velocity heterogeneity is dominated by conversion to body waves and in particular SV energy. Low frequency P and SV energy is scattered in a backwards direction, high frequency P and SV energy is scattered in a forward direction.

As with scattering from rough topography, much of the converted SV energy will be trapped in the crustal waveguide at Lg phase velocities. Therefore, Rayleigh (Rg) to SV body wave conversion by shallow heterogeneity and topography should contribute to formation of Lg by explosions, quarry blasts, and shallow earthquakes.

A comparison is made with results for P-coda from Greenfield (1971). The comparison indicates that self-similar and Gaussian models could be derived with rms velocity variations between 7 and 15% in the upper 3 km of the crust that would produce the observed P-coda/P power levels indicated by Greenfield (1971).

SUMMARY

Rayleigh waves normally incident upon 2-D shallow heterogeneity are simulated by the linear finite-difference method to study attenuation, transmission, and reflection of Rayleigh waves and to measure the Rayleigh-to-P and -SV body wave conversion. Transmission, reflection, and scattering depend on the depth, average scale size of the heterogeneity and the amplitude of the spatial fluctuation of velocity. As expected, larger spatial variation in velocity attenuates Rayleigh waves more than smooth media, and the attenuation is roughly proportional to the variance of the velocity fluctuation. The attenuation and scattering due to shallow heterogeneity is weaker than attenuation due to moderately rough topography.

Scattered body wave energy is studied as a function of frequency, scattering angle, and wave type (P or SV). Attenuation of Rayleigh waves by scattering from 2-D shallow velocity heterogeneity is dominated by conversion to body waves and in particular SV energy. Low frequency P and SV energy is scattered in a backwards direction, and high frequency P and SV energy is scattered in a forward direction.

As with scattering from rough topography, much of the converted SV energy will be trapped in the crustal waveguide at Lg phase velocities. Therefore, Rayleigh (Rg) to SV body wave conversion by shallow heterogeneity and topography should contribute to the formation of Lg by explosions, quarry blasts, and shallow earthquakes.

A comparison is made with results for P-coda from Greenfield (1971). The comparison indicates that self-similar and Gaussian models could be derived with rms velocity variations between 7 and 15% in the upper 3 km of the crust that would produce the observed P-coda/P power levels observed by Greenfield (1971).

TABLE OF CONTENTS

INTRODUCTION

A significant fraction of the elastic energy generated by a shallow explosion is contained in short-period Rayleigh waves. These short-period Rayleigh waves are the largest phase on the near-source seismogram. Although short-period Rayleigh or Rg are commonly seen on regional seismograms from shallow sources such as quarry blasts, they are attenuated rather rapidly with spatial Q's at 1 Hz in the range of 50 to 200 (Kafka, 1987; and personal communication).

Attenuation can be due to intrinsic shear attenuation in the near surface, or it can be accomplished by scattering from shallow heterogeneity and topography. If the energy is scattered then it must be observed as coda in the near-source, regional, and/or teleseismic seismogram. Scattering of Rayleigh waves has been hypothesized to produce teleseismic P-wave coda from Novaya Zemlya explosions by Greenfield (1971). Gupta *et al.* (1985) and Gupta and Blandford (1987) propose a model that suggests that P-wave coda is largely composed of scattered Rayleigh waves and therefore coda should contain information about the depth of burial of an explosion. They suggest that P-wave coda by nature of its averaging properties gives a more precise measure of yield than the direct P wave. However, since we have no accepted model for the generation of P-coda by explosions, such a relationship must be established empirically for each testing area.

In support of the Gupta *et al.* (1985) model for Rayleigh to P-wave coda generation, Lay (1987a) observed frequency dependence of the temporal energy centroid from Pahute Mesa. Recently, Lay (1987b) has attempted to image scattered Rayleigh waves at Pahute Mesa assuming that short-period (1 Hz) teleseismic P-wave coda is produced by conversion from Rayleigh waves initially generated by the explosions. He finds that 1 Hz coda does have some spatial patterns reminiscent of the focusing-defocusing patterns of direct P-waves at Pahute

Mesa. Cormier (1987) puts forth a model for coda generation that hypothesizes that coda only partially averages the focusing-defocusing near the source and near the receiver.

McLaughlin *et al.* (1983) examined coda of the near-source seismogram at Pahute Mesa. Although they found that the major transverse motion observed in the near-field appeared to arise directly from the explosion, much of the transverse coda energy was characteristic of scattered phases, and the important scale lengths of shallow heterogeneity at Pahute Mesa were in the 0.5 to 1 km range. Such scale lengths should be optimal for scattering the 1 to 2 Hz Rayleigh waves at Pahute Mesa. However, since the mesa has both topographic relief as well as considerable geologic complexity, it is uncertain at this time as to what structures are responsible for the teleseismic P-coda.

In a related matter, Key (1967 and 1968) observed P to Rayleigh scattering by specific isolated topographic features in the vicinity of the EKA array. Since this is the reciprocal problem of Rayleigh to P wave scattering, one can consider this as additional motivation for studying the phenomenon. Also using array techniques, Dainty (1986) observed that much of the locally generated P-coda at NORSAR is characterized by energy with Rayleigh wave phase velocities. Sometimes the NORSAR coda could be seen to arrive from a specific direction, but it was often isotropic. Der *et al.* (1984) concluded using deconvolution techniques at arrays that the vertical P-wave coda consisted of approximately 50% locally generated response to plane waves arriving near the receiver and of approximately 50% that arrived from the source region as plane waves across the array at the same slowness as the direct P wave.

The fact that explosion transverse Lg is on average just as large as the radial or vertical component of Lg serves to highlight our lack of understanding of the scattering problem. Gupta and Blandford (1983) proposed that P-to-SV and SV-to-SH scattering was responsible for the growth of the transverse Lg with distance, and Baumgardt (1985) has proposed that P-coda at NORSAR can be observed scattered from "Lg" crossing the Ural mountains. Both of these problems have in common the need to quantify the conversion efficiency of modal waves to body waves and vice versa.

The generation of SV-Lg by explosions is an important problem not only because it is poorly understood but because Lg is commonly used to estimate the yield of explosions (as in Nuttli, 1986a, 1986b, 1987a, and 1987b). The attenuation correction for the Lg amplitude is derived by an analysis of the Lg coda as if it were backscattered Lg modal waves. This Lg coda analysis is questioned by Der *et al.* (1987). They claim that the Lg coda is converted fundamental Rayleigh and not proper "Lg".

Aki and Chouet (1975) proposed models for the generation of coda as the backscattering of S waves and/or surface waves. Their coda model of S-wave single backscattering has become a frequently used paradigm; however, their observations that coda levels were higher at stations located on alluvium and in valleys suggest that much of the coda is surface-wave related. Phillips and Aki (1986) found additional evidence for surface waves at a number of such stations. Estimates for generation of surface waves by incident SV waves and backscattering cross-sections for Rayleigh waves upon topography and shallow heterogeneity would be useful in the modeling of coda. Since coda Q inferred from the coda of seismograms is often interpreted as the crustal shear-wave Q, it is important that the correct model for the creation and propagation of coda be determined.

Frankel and Wennenberg (1987) propose a model for coda that stresses the multiple scattering nature of coda and emphasizes the observed energy flux. Their model questions several important assumptions inherent in the Aki and Chouet (1975) single backscattering "Born approximation" model. Central to these questions of the single scattering model is the issue of conversion between body and surface wave modes of propagation. Dainty *et al.*

(1987) argue that late arriving coda (> 10 to 15 sec) from local earthquakes is horizontally propagating modal or Lg energy. Der *et al.* (1984) propose that a significant portion of the Lg coda is composed of short-period fundamental Rayleigh waves that concentrate energy near the surface and are multiply scattered, contributing to long Lg coda on regional seismograms.

In this report we conduct simulations of fundamental scattering experiments of Rayleigh waves incident upon shallow heterogeneity. Our goal is to determine some basic quantities such as scattering strength and conversion efficiency as well as backscattering strength of shallow heterogeneities. These quantities are needed in order to compose models for coda observed near the surface of the Earth. McLaughlin and Jih (1986b) examined the interaction of incident Rayleigh waves upon 2-D topography using two-dimensional linear elastodynamic finite difference method (LFD). In this report, we explore the stability of planar Rayleigh waves incident upon a 2-D shallow heterogeneous layer of various thicknesses, scale lengths, and rms velocity fluctuations embedded in a homogeneous half space using the same method of analysis. All of the geometries simulated in this work represent planar Rayleigh waves incident upon 2-D heterogeneity.

We first examine the problem of transmission and the partitioning of energy by the scattering process. It is demonstrated as expected that larger scale variations in velocity produce larger attenuation. Reflection (backscattering) is observed to be an inefficient process for all cases examined except for folded media. In this way we characterize shallow heterogeneity by a spatial Q for the transmitted Rayleigh waves and examine the partitioning of energy into scattered body waves. We use the converted body wave field at depth in the half-space as a measure of the simulated far-field P and S coda. Compared to the strong attenuation of short-period fundamental Rayleigh waves due to moderately rough topography, we find that shallow heterogeneity generates fewer Rayleigh-to-body wave conversions, and hence attenuation is less for shallow heterogeneity than for rough topography. Examination of the converted body wave field in the half-space leads us to conclude that much of the SV enrgy will be trapped in the crust as Lg. Conversely, it can be argued that incident SV and P waves will generate Rayleigh waves that propagate as coda on the surface.

We have chosen LFD modeling out of convenience and consistency. The method has the advantages that the solution contains all conversions (P-SV, SV-P) and all orders of multiple scattering. We use the 2nd order formulation of Kelley *et al.* (1976) with absorbing boundary conditions described by Clayton and Engquist (1977) and 1st order free-surface boundary conditions for topographic surfaces described by Jih *et al.* (1986). The method permits examination of fairly general 2-D models. Surface waves are introduced as initial conditions within the half-space grid. There is now a considerable body of work covering many aspects of scattering using 2-D LFD methods (as reviewed by by Frankel, 1987).

THE FINITE-DIFFERENCE SCHEME

The 2-D linear finite-difference scheme popularized by Kelly *et al.* (1976) is used with the absorbing boundary conditions (Clayton and Engquist, 1977; Emerman and Stephen, 1983) on both the sides and the bottom of the grid. Even with the absorbing boundary conditions, the simulations are run with large enough grids such that for the duration of the simulations reflections from the sides do not seriously contaminate the results.

The shallow heterogeneous layers used in these experiments consist of 3 types:

1. Gaussian media created by convolving a 2-D white noise field with 2-D Gaussian filters with specified sizes of the dominant scatterers (*i.e.* mean grain size, a), which turn out to be proportional to the mean spatial correlation distance.

2. folded layers with sinusoidal shape of specified wavelength, amplitude and velocity profile.

3. self-similar media generated by modulating the wavenumber-wavenumber spectra of a white velocity field with the 2-D Fourier transform, $\frac{a^2}{1 + k^2a^2}$, of a special Von Karman correlation function.

These heterogeneous media are then embedded into a homogeneous half-space with P- and S-wave velocities of 5.0 and 2.96 km/sec respectively, corresponding to a Poisson's ratio of 0.35 and a Rayleigh wave velocity, γ, of 2.71 km/sec. Similar random media have been widely used in modeling the scattering of either acoustic or elastic wave by the finite-difference method (Frankel and Clayton, 1984,1986; Levander and Hill, 1985; Levander, 1985; Frankel and Wennerberg, 1987; McLauglin *et al.* 1987a,c)

The formulation generating the incident fundamental Rayleigh wave packet in the homogeneous portion of the medium is analogous to that of Boore (1970) or Munasinghe and Farnell (1973), which has been used extensively by Martel *et al.* (1977), Fuyuki and Matsumoto (1980), Fuyuki and Nakano (1984), Levander (1985), McLaughlin and Jih (1986b). The initial waveform is the fundamental mode Rayleigh wave in the homogeneous half-space with a Ricker wavelet shape. Figures 1 through 3 show the displacement eigenfunctions of the fundamental mode Rayleigh wave (Figure 1), the Ricker wavelet and its wavenumber spectrum (Figure 2), and the near-surface retrograde particle motion (Figure 3). Most of the energy of the incident wave is concentrated in the frequency band below 0.9 cycle/km $\approx$ 2.4 Hz (Figure 2). To reduce the grid dispersion, we have oversampled the incident wave packet by choosing the dominant wavelength to be 3.2 km = 32 Δx, where Δx =0.1 km is the grid spacing. The whole grid has dimension 390 by 260, with the heterogeneous media embedded in the center part near the surface.

NUMERICAL EXPERIMENTS

LFD simulations were first performed for 24 combinations of shallow Gaussian heterogeneities with 4 rms velocity fluctuations (5%, 7%, 10% and 20%), 2 dominant scatterer sizes (1km and 2km), and 3 different depths of the heterogeneous layer (1km, 2km, and 3.2km). 10 fixed seismograms are used to record the near surface displacements and strains. Figures 6A through 6H show snapshots of the displacement fields due to a Rayleigh wave propagating in media with shallow heterogeneity of fixed thickness h and various velocity fluctuations ν and mean scatterer sizes a. Successive frames are separated by intervals of 2 seconds. The reflection and transmission coefficients of Rayleigh waves incident upon such media are dependent on all these factors: ν, a, h. Here we define the energy transmission coefficient, T, as $T(f) = \dfrac{Power_{trans}(f)}{Power_{inc}(f)}$. The reflection coefficient, R, is defined in an analogous way: $R(f) = \dfrac{Power_{refl}(f)}{Power_{inc}(f)}$. Power spectra were used to compute the coefficients so as not to be biased by the dispersion effects. The strain in each case was "measured" one grid point below the flat surface away from the heterogeneity in question.

McLaughlin and Jih (1986b) conducted experiments to justify that, in the case of a homogeneous half-space, the grid dispersion only modulates the spectra of the propagating Rayleigh wave. They also showed that spectral ratios can be used to estimate the scattering attenuation due to random topography. We computed the attenuation, Γ, for the shallow heterogeneities in a similar way as did McLaughlin and Jih (1986b): $\Gamma(f) \equiv Q^{-1}(f) \equiv -ln(T(f))(\dfrac{\gamma}{2\pi f\Delta})$ where γ = 2.71 km/sec is the group velocity of the incident Rayleigh wave and where Δ the total length of the heterogeneity, which is fixed to be 12 km in all our experiments. Table 1 below gives the effective Q at 0.78 Hz measured with vertical displacement near the surface. The attenuation factor, $1/Q$, plotted as a function of frequency, is shown in Figure 8 for these eight cases.

TABLE 1. Q measured at $f = 0.78$Hz

f	v	a	Q_V
.78	5%	1	617
.78	7%	1	248
.78	10%	1	127
.78	20%	1	38 ± 18%
.78	5%	2	1471
.78	7%	2	394
.78	10%	2	185
.78	20%	2	58 ± 9%

For larger velocity variation (*e.g.* 10% or 20%), the attenuation tends to be insensitive to the thickness of the heterogeneity, and the Q measurement would be more accurate. Frankel and Clayton (1984) and McLaughlin *et al.* (1987a) reported that Q^{-1} was proportional to the variance of the random medium for body waves in media where the scatterers are comparable to the seismic wavelength. This is consistent with result shown in Table 1 in which Q_V varies in a manner essentially proportional to v^2.

A standard (least-squares) regression calculation is performed assuming that the attenuation factor is proportional to a power of the equivalent scattering energy-flux, ξ, (see Appendix):

$$\Gamma \equiv \frac{1}{Q(f)} = \Gamma_o \ \xi^y \tag{1}$$

The equivalent scattering energy-flux of the medium, ξ, is defined as

$$\xi \ \equiv \ < \int (f_u^2 + f_w^2) \, dz > \tag{2}$$

where the equivalent scattering forces, f_u and f_w, are derived from a perturbation analysis to the equations of motion due to the perturbations in the elastic moduli, $\delta(\lambda+2\mu)$ and $\delta\mu$,

$$f_u \equiv \delta(\lambda + 2\mu) \, [U_{xx} + W_{xz}] + \delta\mu \, [U_{zz} - W_{xz}] \tag{3a}$$

$$f_w \equiv \delta(\lambda + 2\mu)\,[U_{xz} + W_{zz}] + \delta\mu\,[W_{xx} - U_{xz}] \quad \text{(3b)}$$

and where U_{xx}, U_{zz}, U_{zz}, *etc*, are the 2nd order spatial derivatives of the displacement eigenfunction of the fundamental Rayleigh wave in a homogeneous half space. A more detailed derivation of the above formulas is contained in the Appendix. Under the assumption that the medium has constant density, ρ, across the grid, $\delta(\lambda + 2\mu)$ and $\delta\mu$ reduce to the velocity fluctuations $\alpha^2 - \alpha_o^2$ and $\beta^2 - \beta_o^2$ respectively.

For fixed *ka*, the attenuation factor, $1/Q$, increases with the energy-flux of the medium (Figure 9). But the rate of increase depends on *ka*. We see that a first order perturbation analysis of the body-forces should be sufficient to describe the attenuation of the Rayleigh waves for heterogeneity up to 20% rms velocity variation. The eigenfunctions $U(z)$ and $W(z)$ do not appear to be perturbed by the random heterogeneity to the extent that the scaling of equation (1) breaks down. The attenuation is therefore dependent upon a kernel that depends only on the distribution of the scatters with depth and the unperturbed eigenfunctions as a function of depth (equations 2 and 3a,b).

A horizontal array of 64 sensors are equally spaced ($\Delta x = 0.5$ km) near the bottom of the grid to record the converted P (dilatation) and SV (rotation) strain fields. Figures 10A through 10F show the seismic sections recording the converted P wave (dilatational strain, upper) and S wave (rotational strain, lower) at every other sensor of the horizontal arrays. The coda lasts as long as it takes the Rayleigh wave to propagate across the medium.

A frequency-wavenumber analysis technique is used to produce F-K plots of the scattered dilatational and rotational body wavefield as observed near the bottom of the grid (Figures 11A through 11F). Note that at 3 and 4 Hz, the body waves are mostly forward-scattered waves. The spectra of the body waves reflect the spatial attenuation spectra, $Q^{-1}(f)$, of the Rayleigh wave.

Several observations can be made immediately. From 0.5 to 2 Hz the power level increases as *h* or ν increases. That those media with smaller grain sizes *a* would cause more scattering loss is also consistent with the Q measurements, *i.e.*, Gaussian media with smaller grain sizes produce lower Q's. Also, the converted SV waves contain substantially more high frequency components (2 Hz) than the P waves.

For Gaussian media with the same ν and *a*, the power ratios of converted P to S waves appears to be a monotone function of the thickness of the heterogeneity, *h*. At 1 Hz, P/SV ratio decreases as *h* increases, while at 2 Hz, P/SV ratio increases with *h*.

For comparison, several LFD experiments were done with folded layers as well as random media with different spatial autocorrelation structures. Each folded homogeneous sinusoidal layer has wavelength 2km, (peak-to-peak) amplitude 2.5km, and thickness 0.5km. The velocity profile has a normal distribution with mean of 5 km/sec and standard deviation of *10%. An interesting phenomenon is obvious from the snapshots* (Figure 6J), namely that the converted body wavefields are relatively clean as compared to all other cases. Multiplely scattered Rayleigh waves, both reflected and transmitted ones, are generated while the incident wave propagates across the layered structure. There was no head wave generated (Figure 7J), and the attenuation measured is insignificantly small. This is the only model which obviously generates more back scattered body waves at 1Hz (Figure 10J, 11J).

While for the Gaussian or exponential media cases, the correlation distance *a* is proportional to the dominant size of the scatterers, von Karman media contain scatterers with size smaller than *a*, and they are referred to in Frankel and Clayton (1986) as *self–similar* media. A rudimentary comparison indicates that the thickness of the self-similar media *significantly* affects the attenuation. It is not surprising that self-similar media attenuate the Rayleigh wave more than Gaussian media of the same velocity fluctuation, ν, and depth.

DISCUSSION AND CONCLUSIONS

In order to use the results that we have generated from the LFD simulations, we need to develop an approximate theory for the prediction of coda by the scattering of Rayleigh waves. In order to do this we will use the dilatation and rotational strain sensors located near the bottom of the grid and the attenuation estimates for the Rayleigh wave to give an estimate of the energy radiated by the scatterers per unit distance for an incident Rayleigh wave of unit vertical amplitude at the surface. We will use a perturbation approach to replace the scatterers by a surface layer of equivalent sources. The concepts loosely follow the formalism of Greenfield (1971).

For our purposes it is convenient to think of the simulation as though we had a continuous wave (CW) source radiating Rayleigh waves from the left side of the grid and that we observe the power level of coda in the far-field along the array of dilatational and rotational "sensors" near the bottom of the grid. The total energy of the incident Rayleigh wave packet in our simulation is known, and the simulation lasts long enough for the wave packet to completely clear the area of scatterers. We estimate the P coda power levels in the far-field with respect to the incident power by computing power spectra and correcting the power levels for the appropriate time windows. The ratio of the observed P-wave or S-wave coda power spectra to the input power spectrum of the Rayleigh wave of known amplitude then gives us a measure of the scattering of the heterogeneity as a function of frequency.

The dilatational "sensors" are omnidirectional detectors of traveling P waves such that the dilatation, $\theta(\omega)$, is proportional to the P-wave amplitude, $u(\omega)$.

$$\theta^2 = (k_P u)^2 = (\frac{\omega u}{\alpha})^2$$

For a given frequency, the average P-coda power density, E_{Pc} (energy per unit volume), observed at a dilatational sensor near the bottom of the grid is related to the velocity signal power and hence ultimately to the observed dilatational signal power,

$$E_{Pc} = \rho v^2 = \rho\omega^2 u^2 = \rho\omega^2 k^{-2}\theta^2 = \rho\alpha^2\theta^2$$

In our simulation, the Rayleigh waves were normalized such that the Rayleigh wave vertical amplitude at the surface at each frequency was unit amplitude times the spectral amplitude of the Ricker wavelet. Therefore, the power spectral ratios shown in Figures 12A through 12E relate the average dilatational power in the far-field (distance ~ $26*10^5$ cm) as a function of frequency for an incident planar Rayleigh wave with amplitude of 10^5 cm, incident upon $12*10^5$ cm length of shallow heterogeneity. We must also adjust for the fact that the Rayleigh-wave packet is 4 seconds long whereas the coda lasts approximately 12 seconds as the Rayleigh-wave packet passes through the 12 km of heterogeneity. The correction for the attenuation of the planar Rayleigh wave in 12 km is of second order in our simulations ($e^{-(\frac{\pi f \Delta}{Q\gamma})} > 0.6$ for $Q > 30$, $f \sim 1$ Hz, $\Delta = 12$ km). We correct the coda power density to a distance of 3.2 km from the surface of the half-space as if it were radiated by a distribution of line scatterers along the free-surface. This correction is simply a factor of $\frac{r}{r_0} \sim 26/3.2 \sim 8$. Therefore, the P-coda energy levels radiating from the bottom of the layer of heterogeneity at a depth of 3.2 km in Figures 12A-E are in units of $3.4*10^{-5}$ $erg/sec/cm^3/(cm$ of heterogeneity)/(cm^2 incident Rayleigh wave). Similarly, the S-wave coda power ratios are in units of $1.2*10^{-5}$ $erg/sec/cm^3/(cm$ of heterogeneity)/(cm^2 incident Rayleigh wave). We will give these two quantities the designation, $\zeta_P(\omega)$, and $\zeta_S(\omega)$. In our simulations, the S-wave coda energy density level is generally about equal to the P-wave coda energy density level. Since body vector forces generate S-wave/P-wave amplitude ratios proportional to $(\alpha/\beta)^2$ and body stresses generate S-wave/P-wave amplitude ratios proportional to $(\alpha/\beta)^3$, we see that the equivalent sources required to describe the scatterers can not be simply described as either body forces or body stresses. The answer may lie in the multiple scattering and the free surface conversion of P to S and S to P. This implies that we will require a separate set of equivalent sources for the P-coda and S-coda until a self-consistent model can be constructed.

For example, we use the results from the simulation with 20% rms velocity variation, Gaussian scale length of 1 km, in a surface layer 3.2 km thick. The P-coda energy level at 1 Hz is $2.6*10^{-6}$ $erg/sec/cm^3/cm/cm^2$. This is equivalent to an explosive point-source with rms moment-rate of $0.2*10^{20}$ dyne-cm/sec at a distance of 3.2 km.

In order to predict the Rayleigh to P-coda energy density we must predict the Rayleigh-wave amplitude at a given distance from the epicenter. The Rayleigh-wave vertical displacement amplitude from an explosive point source at depth, h, observed at a distance, Δ, can be written as (Hudson and Douglas, 1975)

$$u_z(\omega) = A(\alpha,\beta)\, B(\alpha,\beta,\rho,\omega)\, \Delta^{-1/2}\, exp(-\omega h\eta/\gamma)\, exp(-\frac{\pi f\Delta}{Q_R\gamma})\, m(\omega)$$

$$B(\alpha,\beta,\rho,\omega) = \sqrt{\frac{\omega^3\gamma}{2\pi\beta}}\frac{1}{8\rho\alpha^2\beta^{3/2}}$$

$$A(\alpha,\beta)=\frac{2-\gamma^2/\beta^2}{2-\gamma^2/\beta^2-\eta\eta'-(\eta'/\eta+\eta/\eta')/2}$$

Where α, β, and γ are the P-, S-, and Rayleigh-wave velocities and where $\eta = (1-\gamma^2/\alpha^2)^{1/2}$ and $\eta' = (1-\gamma^2/\beta^2)^{1/2}$. Q_R is the Rayleigh wave quality factor. For example, a 10^{20} dyne-cm explosive source buried 0.5 km will produce $3*10^{-4}$ cm of 1 Hz motion at 10 km distance for our model half-space. So, our previous example becomes an equivalent explosive source density of $6*10^{-15}$ dyne-cm/sec/cm or $6*10^{20}$ dyne-cm/sec/km.

We can now form a simple approximate model for the production of teleseismic P coda from an explosion. As Greenfield (1971) pointed out, the P-coda/P power ratio can be predicted as a function of time if the conversion efficiency (scattering cross-section) is known for short-period Rayleigh to downward scattered P-wave energy. For teleseismic paths, the geometrical spreading for P-coda and the direct P approximately cancel in the P-coda/P ratio. The important factors are the relative excitation of P-wave amplitude and Rayleigh-wave amplitude by the coda sources and the explosion source, respectively, integrated over the scattering volume per unit time.

For the case of the Rayleigh wave spreading out from a point source, the volume is replaced by the surface area at time $t = \frac{\Delta}{\gamma}$ contributing equivalent scattering sources; $dA = 2\pi\Delta d\Delta = 2\pi\gamma^2 t dt$. We assume that the energy is additive from the scattering surface and that to first order the scattering is isotropic. We can modify this assumption later by the introduction of a radiation pattern for the equivalent scatterers and the computation of numerical integrals over the area swept out in each increment in time by the Rayleigh wave. However, to first order we can write that the P-coda power received in a time interval dt and frequency interval $d\omega$ normalized to the direct P-wave is given by

$$\frac{<u_{Pc}^2>}{u_P^2} dt d\omega = A^2(\alpha,\beta) B^2(\alpha,\beta,\rho,\omega)\, \zeta_P(\omega)\, e^{-(\frac{2\omega h\eta}{\gamma})} (\gamma t)^{-1} e^{-(\frac{\omega t}{Q_R(\omega)\gamma})} 2\pi\gamma^2 t \, dt d\omega$$

We see that if the scatterers are evenly distributed then the time decay of the P-coda generated in this manner is controlled by the Q_R of the short-period Rayleigh, while the frequency dependence is determined by the depth of burial, h, and the frequency dependence of the scattering $\zeta(\omega)$. This suggests that if all P-coda were generated in this manner, we could determine the Q from the coda time decay. Since there is coda generated by other mechanisms, this is probably not a very helpful procedure. Also, since the direct P spectra may be contaminated by P+pP interference effects, we should more properly consider the normalization factor as a more idealized explosion source spectrum. The actual level of generated P-coda is a complicated function of ζ, h, and the functions A and B. For layered media we can expect that the dependence will become even more complicated.

For the 20% rms Gaussian model with 1 km scale length heterogeneity in the upper 3.2 km, we can predict the P-coda/P signal energy as a function of time. Greenfield (1971) computed the average coda signal power in the 10 to 40 second window from a bandpass filter normalized to the total energy in the first 10 seconds of the P wave, W_0, given by

$$W_0 = \frac{1}{30}\frac{\int_{10}^{40} S^2(t)dt}{\int_{0}^{10} S^2(t)dt}$$

His W_0 estimates for 1 Hz from two Novaya Zemlya explosions of 21 Oct 1967 and 27 Oct 1966 on LASA beams were about 0.0085 and 0.015 respectively. Since the beams reject local coda this is probably as reasonable a measure of the near source generated coda as can be obtained. Our 20% rms Gaussian model predicts W_0 = 0.011, which is in the right neighborhood given the crudeness of our model. Velocity heterogeneity of 20% rms in the upper 3.2 km probably is an upper limit if we consider typical velocity distributions of sedimentary rocks. Since there are other mechanisms of near source scattering, this may not be unreasonable result. We have found that rough topography produces greater Rayleigh-wave scattering than shallow heterogeneity, and therefore perhaps topography is responsible for more scattering at Novaya Zemlya than is shallow heterogeneity.

For comparison, the following table compares predicted W_0 values for several of our shallow heterogeneity models at 1 Hz. "SS1" and "SS2" are the self-similar models with 1 and 2 km scale lengths respectively. The "GA1" and "GA2" models are the Gaussian autocorrelation models with scale lengths of 1 and 2 km respectively. The rms velocity variation, v, is indicated for each model as well as the predicted value of ζ_P and the Rayleigh wave Q. We see that there are several models that predict values of W_0 in a range around 0.01. Since $Q(f)$ and $\zeta(f)$ are roughly flat between 0.5 and 1.5 Hz for most of the models, we would expect that the frequency dependence of the Rayleigh to P-coda ratios would reflect the terms for excitation of the Rayleigh wave, $\omega^{3/2}e^{-(\omega h\eta/\gamma)}$, and the attenuation of the short-period Rayleigh wave, $e^{-(\pi f t/Q_R)}$. Greenfield's LASA beam data for Novaya Zemlya in the 0.5 to 2.0 Hz range suggest a Q_R in the range of 20 to 80 if we assume that the dependence of $W_0(f)$ reflects the dependence of $Q_R(f)$. Either the self-similar models or the Gaussian models with rms velocity variations in the 7 to 15% range and scale lengths in the 1 to 2 km range could be found to match his results. Until such time as more detailed analysis is made of the P-coda/P as a function of frequency and time, there are far too few degrees of freedom to constrain the selection of scattering models. Of particular importance would be array analysis of P-coda using band-pass filters applied to multichannel deconvolution results such as those of Der *et al.* (1987). Also, analysis of the type performed by Lay (1987b) to image scatters using broadband data coupled with forward models would help to delineate the actual nature of the scatterers.

1 Hz W_0 PREDICTIONS				
MODEL	ν	W_0	ζ_P	Q_R
SS1	20%	1.25544e-03	2.14525e-06	19.95
SS1	10%	3.66908e-02	1.86844e-06	70.79
SS1	7%	5.43877e-02	1.55410e-06	104.71
SS1	5%	6.02012e-02	1.35356e-06	128.82
SS2	20%	1.02967e-03	2.14525e-06	19.05
SS2	10%	4.04064e-02	1.70404e-06	79.43
SS2	7%	6.36782e-02	1.62734e-06	114.82
SS2	5%	6.46347e-02	1.35356e-06	138.04
GA1	20%	1.09775e-02	2.57916e-06	35.48
GA1	10%	3.75454e-02	1.91196e-06	70.79
GA1	7%	4.73805e-02	1.62734e-06	91.20
GA1	5%	5.10469e-02	1.41736e-06	107.15
GA2	20%	9.08656e-03	1.17891e-06	44.67
GA2	10%	2.32515e-02	9.80571e-07	79.43
GA2	7%	2.61012e-02	8.15603e-07	97.72
GA2	5%	2.60344e-02	6.47857e-07	117.49

The analysis of the P-coda/P ratio allows us to cancel the propagation term for the P-coda from scatterer to receiver. In order to use the data for analysis of the potential excitation of SV-Lg by the conversion of Rayleigh to SV, Green's functions will be required for the SV-Lg wave packet. This is a somewhat more difficult problem, but it can in theory be done much the same way as we have treated the P-coda problem. This important problem is left for a later analysis.

We see that moderate heterogeneity in a half space does not attenuate short-period fundamental Rayleigh waves nearly so much as rough topography does (McLaughlin and Jih, 1986b), but it can still contribute substantial P-coda and moderate attenuation of Rg. For the Gaussian media used in these simulations, the energy lost due to body wave conversion varies from several percent to 20% in 12 km distance. A significant result of the simulations is that reflection of Rayleigh waves by heterogeneity at normal incidence is in most cases inefficient, as was the case for rough topography. The only exception observed was a folded structure with a resonant response to the incident Rayleigh wave. Therefore we should not expect to see

Rayleigh-wave back-scattering as a significant contributor to the multiple scattering of fundamental Rayleigh waves that populate coda for Gaussian or self-similar media. Backscattering can be significant for media with well defined organized structures such as folded sedimentary structures. In such a case the backscattered wave has a narrow narrow bandwidth reflecting the resonance phenomenon.

More complicated random media contain many scale lengths and introduce broad-band effects. The Rayleigh-wave attenuation is a complicated function of frequency, but it attains a maximum in the range where the characteristic wavelength of the medium matches the wavelength of the incident Rayleigh wave.

At low frequency ($\lambda > a$) the coda dilatational and rotational wavenumber spectra indicate that the scattered P and SV waves are scattered in the forward direction except for strongly folded structures or Gaussian medium with very strong velocity fluctuations (20%). For higher frequencies ($\lambda < a$ *Hz*), *the scattered body waves are always maximum* in the forward direction. A detailed analysis of Rayleigh to P-coda scattering will have to take this effect into account with an effective radiation pattern to the "equivalent scatterer".

The results presented offer a beginning approach to understanding the effects upon surface waves of scattering by lateral heterogeneity. A complete exploration of the problem will require variation of the P and S velocities, near surface velocity gradients, and crustal velocity heterogeneity as a function of depth.

Much of the SV energy scattered by near surface heterogeneities is concentrated at apparent velocities within 150% of the Rayleigh phase velocity. A crust with surface layer with β = 2.96 km/sec as used in these simulations would leak much of the energy to the mantle. However, if the near-surface velocity of the model is lowered, then the slowness space occupied by the scattered waves will scale to the Rayleigh phase velocity and more energy will be trapped in the crust. Other ways of increasing the trapping of the scattered SV energy are increasing the α/β ratio in the near surface, introduction of gradients near the surface to create higher order modes, and introduction of deeper velocity heterogeneity to scatter P and SV energy back into the waveguide. In short, all these mechanisms can act only to increase the Rayleigh-to-Lg coupling. Therfore, we expect that in real seismological situations much of the Rayleigh-wave energy scattered into SV by near-surface heterogeneity will be trapped in the crust and will find a path to the Lg wavepacket.

ACKNOWLEDGEMENTS

This work was supported by DARPA contract F19628-86-C-0054 monitored by the Air Force Geophysics Laboratory. The views and conclusions contained in this work are those of the authors and should not be interpreted as necessarily representing the official policies, either expressed or implied, of the Defense Advanced Research Projects Agency or the U.S. Government.

REFERENCES

Aki, K. and B. Chouet (1975), Origin of coda waves: source, attenuation, and scattering effects, *J. Geophys. Res.* **80,** 3322-3342.

Baumgardt, D. R. (1985), Comparative analysis of teleseismic P coda and Lg waves from underground nuclear explosions in Eurasia: *Bull. Seism. Soc. Am.*, **75,** 1413-1434

Boore, D. (1970), Love waves in nonuniform wave guides: finite-difference calculations, *J. Geophy. Res.*, **75,** 1512-1527,

Clayton, R. and B. Engquist (1977), Absorbing boundary conditions for acoustic and elastic wave equations, *Bull. Seism. Soc. Am.*, **67,** 1529-1540.

Clayton, R. W., D. G. Harkrider, and D. V. Helmberger (1986), Body and surface wave modeling of observed seismic events, *AFGL-TR-86-0021, Semi-Annual Report # 1,* California Institute of Technology, Pasadena, CA 91125. (ADA169413)

Cormier, V. F. (1987), Focusing and defocusing of teleseismic P waves by known three-dimensional structure beneath Pahute Mesa, Nevada test site, *Bull. Seism. Soc. Am.*, **77,** 1688-1703.

Dainty, A. M. (1986), Coda observed at NORSAR and NORESS, *AFGL-TR-85-0199, Final Report,* Georgia Tech Research Institute, Atlanta, GA 30323. (ADA166454)

Dainty, A. M., R. M. Duckworth, and An Tie (1987). Attenuation and backscattering from local coda, *Bull. Seism. Soc. Am. 77,* 1728-1747.

Der, Z. A., M. E. Marshall, A. O'Donnell, T. W. McElfresh (1984), Spatial coherence structure and attenuation of the Lg phase, site effects, and the interpretation of the Lg coda, *Bull. Seism. Soc. Am.*, **74,** 1125-1147.

Der, Z. A., R. H. Shumway, and A. C. Lees (1987), Multi-channel deconvolution of P waves at seismic arrays, *Bull. Seism. Soc. Am.*, **77,** 195-211.

Drake, (1972), Love and Rayleigh waves in nonhorizontally layered media, *Bull. Seism. Soc. Am.*, **62,** 1241-1258.

Emerman, S. and R. Stephen (1983), Comment on "Absorbing boundary conditions for acoustic and elastic wave equations," by R. Clayton and B. Engquist, *Bull. Seism. Soc. Am.*, **73,** 661-665.

Frankel, A. (1987), A review of numerical experiments on seismic wave scattering, *Pure and Appl. Geophys.*, (in press).

Frankel, A. and R. W. Clayton (1984), A finite-difference simulation of wave propagation in 2-dimensional random media, *Bull. Seism. Soc. Am.*, **74,** 2167-2186.

Frankel, A. and R. W. Clayton (1986), Finite-difference simulation of seismic scattering: implications for the propagation of short-period seismic waves in the crust and models of crustal heterogeneity, *J. Geophy. Res.*, **91**, 6465-6489.

Frankel, A. and L. Wennerberg (1987), Energy-flux model of seismic coda: separation of scattering and intrinsic attenuation, *Bull. Seism. Soc. Am.*, 77, 1223-1251.

Fuyuki, M. and Y. Matsumoto (1980), Finite-difference analysis of Rayleigh wave scattering at a trench, *Bull. Seism. Soc. Am.*, **70**, 2051-2069.

Fuyuki, M. and M. Nakano (1984), Finite-difference analysis of Rayleigh wave transmission past an upward step change, *Bull. Seism. Soc. Am.*, **74**, 893-911.

Greenfield, R. J. (1971), Short-period P-wave generation by Rayleigh-wave scattering at Novaya Zemlya, *J. Geophys. Res.*, **76**, 7988-8002.

Gupta, I. N. and R. R. Blandford (1983), A mechanism for generation of short-period transverse motion from explosions, *Bull. Seism. Soc. Am.*, **73**, 571-591.

Gupta, I. N. and R. R. Blandford (1987), A study of P waves from NTS explosions: near-source information from teleseismic observations? *Bull. Seism. Soc. Am.*, **77**, 1041-1056.

Gupta, I. N., R. R. Blandford, R. A. Wagner, and J. A. Burnetti (1985), Use of P coda for explosion medium and improved yield determination, in *The VELA Program*, A. U. Kerr, Editor, Executive Graphic Services, Washington, D.C., 711-720.

Hill, N. R. and A. R. Levander (1984), Resonances of low-velocity layers with lateral variations, *Bull. Seism. Soc. Am.*, **74**, 521-537.

Hudson, J. A. and A. Douglas (1975), Rayleigh wave spectra and group velocity minima, and the resonance of P waves in layered structure, *Geophys. J. R. astr. Soc.*, **42**, 175-188.

Jih, R.-S., K. L. McLaughlin, and Z. A. Der (1986), Boundary conditions for arbitrary polygonal topography in elastic finite-difference scheme for seismogram generation, Section I of Report *AFGL-TR-86-0159, TGAL-86-03,* Teledyne Geotech, Alexandria, VA (ADA183013)

Kafka, A. L. (1987), Rg waves as depth discriminant for earthquakes and explosions in New England, *DARPA/AFGL 9th Seismic Research Symposium*, 15-18 June, 1987, Nantaucket, MA.

Kelly, K. R., R. W. Ward, S. Treitel, M. Alford (1976), Synthetic seismograms: a finite-difference approach, *Geophysics*, **41**, 2-27.

Key, F. A. (1967), Signal-generated noise recorded at Eskdalemuir seismometer array station, *Bull. Seism. Soc. Am.*, **57**, 27-37.

Key, F. A. (1968), Some observations and analyses of signal generated noise, *Geophys. J. R. astr. Soc.*, **15**, 377-392.

Lay, T. (1987a), Analysis of near-source contributions to early P-wave coda for underground explosions. II. Frequency dependence, *Bull. Seism. Soc. Am.*, **77**, 1252-1273.

Lay, T. (1987b), Analysis of near-source contributions to early P-wave coda for underground explosions. III. Inversion for isotropic scatterers, *Bull. Seism. Soc. Am.*, **77**, 1767-1783.

Levander, A. (1985), Finite-difference calculations of dispersive Rayleigh wave propagation, *Tectonophysics*, **113**, 1-30.

Levander, A. R. and N. R. Hill (1985), P-SV resonances in irregular low-velocity surface layers, *Bull. Seism. Soc. Am.*, **75**, 847-864.

Malin, P. E. and R. A. Phinney (1985), On the relative scattering of P and S waves, *Geophys. J. Roy. astr. Soc.* **80**, 603-618.

Martel, L., M. Munasinghe, G. W. Farnell (1977), Transmission and reflection of Rayleigh wave through a step, *Bull. Seism. Soc. Am.*, **67**, 1277-1290.

McLaughlin, K. L., and L. M. Anderson (1987), Stochastic dispersion of short-period P waves due to scattering and multipathing, *Geophys. J. Roy. astr. Soc., 89-3,* 933-963.

McLaughlin, K. L., L. M. Anderson, and Z. A. Der (1987a) Investigation of scattering and attenuation of seismic waves using 2-dimensional finite difference calculations, in the *Symposium on Scattering of Waves in Random Media and Rough Surfaces*, July 1985, Varadan and Varadan, editors.

McLaughlin, K. L., L. M. Anderson, and A. C. Lees (1987b), Effects of geologic structure on Yucca Flats, NTS, explosion waveforms: 2-dimensional linear finite difference simulations, *Bull. Seism. Soc. Am.*, **77**, 1211-1222.

McLaughlin, K. L. and R.-S. Jih (1986a), Scattering from near-source topography: teleseismic observations and numerical 2-D explosive line source simulations, Section III of Report *AFGL–TR*–86–0159, *TGAL*–86–03, Teledyne Geotech, Alexandria, VA 22314 (ADA183013)

McLaughlin, K. L. and R.-S. Jih (1986b), Finite-difference simulations of Rayleigh wave scattering by 2-D rough topography, Report *AFGL–TR*–86–0269, *TGAL*–86–09, Teledyne Geotech, Alexandria, VA 22314 (ADA179190)

McLaughlin, K. L., R.-S. Jih, and Z. A. Der (1987c), Investigation of explosion generated SV Lg waves in 2-D heterogeneous crustal models by LFD simulations, *DARPA/AFGL 9th Seismic Research Symposium*, 15-18 June, 1987, Nantaucket, MA.

K. L. McLaughlin, L. R. Johnson and T. V. McEvilly (1983), Two-dimensional array measurements of near-source ground accelerations, *Bull. Seism. Soc. Am.*, **73**, 349-375.

Menke, W. (1983), A formula for the apparent attenuation of acoustic waves in randomly layered media, *Geophys. J. R. astr. Soc.*, **75**, 541-544.

Momoi, T. (1981), Scattering of Rayleigh wave at a vertical boundary, *J. Phys. Earth*, **29**, 435-485.

Munasinghe, M. and G. Farnell (1973), Finite-difference analysis of Rayleigh wave scattering at vertical discontinuities: *J. Geophy. Res.*, **78**, 2454-2466.

Nuttli, O. W. (1986a), Yield estimates of Nevada Test Site explosions obtained from seismic Lg waves, *J. Geophys. Res.*, **91**, 2137-2151.

Nuttli, O. W. (1986b), Lg magnitudes of selected East Kazakhstan underground explosions, *Bull. Seism. Soc. Am.*, **76**, 1241-1251.

Nuttli, O. W. (1987a), Lg magnitudes of Degelen, East Kazakhstan, underground explosions, *Bull. Seism. Soc. Am.*, **77**, 679-681.

Nuttli, O. W. (1987b), Lg magnitudes and yield estimates for underground Novaya Zemlya nuclear explosions, *Bull. Seism. Soc. Am. (in press).*

Phillips, S. W. and K. Aki (1986), Site amplification of coda waves from local earthquakes in central California, *Bull. Seism. Soc. Am.*, **76**, 627-648.

Richards, P. G. and W. Menke (1983), The apparent attenuation of a scattering medium, *Bull. Seism. Soc. Am.*, **73**, 1005-1022.

Toksoz, M. N., A. M. Dainty, and E. E. Charrette (1986), Development of ultrasonic modeling techniques for the study of seismic wave scattering due to crustal inhomogeneities, *AFGL-TR-86-0078, Final Report*, Earth Resources Laboratory, MA 02139. ADA170062

Toksoz, M. N. (1983), Development of ultrasonic modeling techniques for the study of crustal inhomogeneities, *AFGL-TR-83-0070, Final Report*, Earth Resources Laboratory, MA 02139. ADA134501

Wu, R. S. (1982), Attenuation of short-period seismic waves due to scattering, *Geophys. Res. Letters*, **9**, 9-12.

FIGURE CAPTIONS

Figure 1 Rayleigh wave displacement eigenfunctions for the vertical and horizontal components of motion.

Figure 2A Wavenumber spectrum $S(k) = (k/k_0)^2 exp[1-(k/k_0)^2]$ of Ricker wavelet where k is wavenumber and $k_0 = 0.3125$ cycle/km the dominant (*i.e.* maximum amplitude) wavenumber.

Figure 2B Ricker wavelet in the spatial domain. IFFT was applied on $S(k)$ to speed up the wavelet generation.

Figure 3 The retrograde particle motion near the surface.

Figure 4 Synthetic near-surface vertical displacements (upper) and horizontal displacements (below) for a Rayleigh wave propagating in a homogeneous half-space.

Figure 5 Spectral ratio of the transmitted Rayleigh waves over the incident Rayleigh waves in a homogeneous half-space. Grid dispersion only modulates the spectra.

Figure 6A The snapshots of the displacement field due to Rayleigh wave propagating in a medium with shallow heterogeneity of $\nu = 5\%$, $a = 1km$, $h = 3.2km$. Successive frames, (A) through (H), are separated by 2 sec intervals. Displacements are proportional to the darkness of the plot and are normalized to the maximum in each frame.

Figure 6B Same as Figure A6 except of $\nu = 5\%$, $a = 2km$, $h = 3.2km$. The diffracted wavefield is less complicated as compared to Figure 6A because smaller grain size causes more reflection ((C),(D) of Figure 6A).

Figure 6C Same as Figure 6A except of $\nu = 7\%$, $a = 1km$, $h = 3.2km$.

Figure 6D Same as Figure 6A except of $\nu = 7\%$, $a = 2km$, $h = 3.2km$.

Figure 6E Same as Figure 6A except of $\nu = 10\%$, $a = 1km$, $h = 3.2km$.

Figure 6F Same as Figure 6A except of $\nu = 10\%$, $a = 2km$, $h = 3.2km$.

Figure 6G Same as Figure 6A except of $\nu = 20\%$, $a = 1km$, $h = 3.2km$.

Figure 6H Same as Figure 6A except of $\nu = 20\%$, $a = 2km$, $h = 3.2km$.

Figure 6I Same as Figure 6A except of self-similar medium with $a = 2km$, $h = 3.2km$, $\nu = 10\%$.

Figure 6J Same as Figure 6A except of folded sinusoidal layers with $h = 3.2km$, $\nu = 10\%$, $\lambda = 2km$, peak-to-peak amplitude 2.5km.

Figure 7A Synthetic near-surface vertical displacements (upper) and horizontal displacements (below) for a Rayleigh wave propagating in a medium with shallow heterogeneity of

$\nu = 5\%$, $a = 1km$, $h = 3.2km$.

Figure 7B Same as Figure 7A except of $\nu = 5\%$, $a = 2km$, $h = 3.2km$.

Figure 7C Same as Figure 7A except of $\nu = 7\%$, $a = 1km$, $h = 3.2km$.

Figure 7D Same as Figure 7A except of $\nu = 7\%$, $a = 2km$, $h = 3.2km$.

Figure 7E Same as Figure 7A except of $\nu = 10\%$, $a = 1km$, $h = 3.2km$.

Figure 7F Same as Figure 7A except of $\nu = 10\%$, $a = 2km$, $h = 3.2km$.

Figure 7G Same as Figure 7A except of $\nu = 20\%$, $a = 1km$, $h = 3.2km$.

Figure 7H Same as Figure 7A except of $\nu = 20\%$, $a = 2km$, $h = 3.2km$.

Figure 7I Same as Figure 7A except of self-similar medium with $a = 2km$, $h = 3.2km$, $\nu = 10\%$.

Figure 7J Same as Figure 7A except of folded sinusoidal layers with $h = 3.2km$, $\nu = 10\%$, $\lambda = 2km$, peak-to-peak amplitude 2.5km.

Figure 8A Attenuation factor observed as a function of frequency for 4 Gaussian media ($a = 1km$, $h = 3.2km$) used in the LFD simulations. "x", "+", triangles, and circles correspond to $\nu = 20\%, 10\%, 7\%$, and 5% respectively.

Figure 8B Same as Figure 8A except of $a = 2km$, $h = 3.2km$.

Figure 8C Same as Figure 8A except of self-similar media with $a = 1km$, $h = 3.2km$.

Figure 8D Same as Figure 8A except of self-similar media with $a = 2km$, $h = 3.2km$.

Figure 8E Same as Figure 8A except of folded sinusoidal layers with $h = 3.2km$, $\lambda = 2km$, peak-to-peak amplitude 2.5km.

Figure 9A The attenuation factor 1/Q at 0.78 Hz versus energy-flux ξ. Observations are shown in circles, and fit to the curve $\Gamma = \Gamma_o \xi^{1.2842}$. All 12 random media (with $\nu = 5\%$, 7%, 10% and 20%) have dominant grain size 1 km.

Figure 9B Same as 9A except for grain size 2 km. The smoothed curve is $\Gamma = \Gamma_o \xi^{1.2991}$.

Figure 9C Same as 9A except for attenuation measured at 1.56 Hz. The smoothed curve is $\Gamma = \Gamma_o \xi^{0.3434}$.

Figure 9D Same as 9A except for attenuation measured at 1.56 Hz and all media have grain size 2 km. The smoothed curve is $\Gamma = \Gamma_o \xi^{0.19944}$.

Figure 10A Seismic sections recording the converted P wave (dilatational strain, upper) and S wave (rotational strain, lower) at a line of 32 sensors near the bottom of the grid spaced 1 km apart for the case of $\nu = 5\%$, $a = 1km$, $h = 3.2km$. See Figure 6A for snapshots.

Figure 10B Same as Figure 10A except of $\nu = 5\%$, $a = 2km$, $h = 3.2km$.

Figure 10C Same as Figure 10A except of $\nu = 7\%$, $a = 1km$, $h = 3.2km$.

Figure 10D Same as Figure 10A except of $\nu = 7\%$, $a = 2km$, $h = 3.2km$.

Figure 10E Same as Figure 10A except of $\nu = 10\%$, $a = 1km$, $h = 3.2km$.

Figure 10F Same as Figure 10A except of $\nu = 10\%$, $a = 2km$, $h = 3.2km$.

Figure 10G Same as Figure 10A except of $\nu = 20\%$, $a = 1km$, $h = 3.2km$.

Figure 10H Same as Figure 10A except of $\nu = 20\%$, $a = 2km$, $h = 3.2km$.

Figure 10I Same as Figure 10A except of self-similar medium with $a = 2km$, $h = 3.2km$, $\nu = 10\%$.

Figure 10J Same as Figure 10A except of folded sinusoidal layers with $h = 3.2km$, $\nu = 10\%$, $\lambda = 2km$, peak-to-peak amplitude 2.5km.

Figure 11A Log-power horizontal wavenumber spectra for the dilatational (upper) and rotational (lower) wavefields recorded across the bottom linear array for the case of $\nu = 5\%$, $a = 1km$, $h = 3.2km$. Power spectra at 1, 2, 3, 4Hz are normalized to the maximum. Normally incident waves have a horizontal wavenumber of zero. Wavenumbers are indicated for horizontally propagating P waves. Forward-scattered waves have negative wavenumbers, backscattered waves have positive wavenumbers. The dilatational and rotational strain energy are largely confined to P wave and S wave slowness across the array respectively.

Figure 11B Same as Figure 11A except of $\nu = 5\%$, $a = 2km$, $h = 3.2km$.

Figure 11C Same as Figure 11A except of $\nu = 7\%$, $a = 1km$, $h = 3.2km$.

Figure 11D Same as Figure 11A except of $\nu = 7\%$, $a = 2km$, $h = 3.2km$.

Figure 11E Same as Figure 11A except of $\nu = 10\%$, $a = 1km$, $h = 3.2km$.

Figure 11F Same as Figure 11A except of $\nu = 10\%$, $a = 2km$, $h = 3.2km$.

Figure 11G Same as Figure 11A except of $\nu = 20\%$, $a = 1km$, $h = 3.2km$.

Figure 11H Same as Figure 11A except of $\nu = 20\%$, $a = 2km$, $h = 3.2km$.

Figure 11I Same as Figure 11A except of self-similar medium with $a = 2km$, $h = 3.2km$, $\nu = 10\%$.

Figure 11J Same as Figure 11A except of folded sinusoidal layers with $h = 3.2km$, $\nu = 10\%$, $\lambda = 2km$, peak-to-peak amplitude 2.5km.

Figure 12A Gaussian autocorrelation models, a= 1 km, h = 3.2 km. Power spectral ratios of the dilatational and rotational strain signals observed 24 km deep within the grid to the vertical displacement of the incident Rayleigh wave. Units are $3.4*10^{-5}$ and $1.2*10^{-5}$ $erg/sec/cm^3/(cm$ of heterogeneity)/(cm^2 incident Rayleigh wave) for the P-wave and S-wave coda power density at a depth of 3.2 km in the grid. P-wave coda is lower set of values, S-wave coda is upper set of values. v varies from 20% (top), 10%, 7%, to 5% (bottom).

Figure 12B Gaussian autocorrelation models with a= 2 km. See Figure 12A caption.

Figure 12C Self-similar autocorrelation models with a= 1 km. See Figure 12A caption.

Figure 12D Self-similar autocorrelation models with a= 2 km. See Figure 12A caption.

Figure 12E Folded models. See Figure 12A caption.

APPENDIX

We start with the 2-D equation of motion for the vertical component of motion,

$$\rho\omega^2 U = (\lambda + 2\mu)(U_{xx} + W_{xz}) + \mu(U_{zz} - U_{xz}). \tag{A1}$$

U and W are the horizontal and vertical displacement components of motion and U_{xx}, U_{xz}, and U_{zz} are the second order partial derivatives of the motion with respect to range, x, and depth, z. The derivation proceeds in a similar manner for the horizontal component of motion, which is left to the reader. The kinetic energy density in the vertical component field is given by $E = \frac{1}{2}\rho\omega^2 U^2$. It follows from the Virial theorem that for linear elastic systems the average potential energy is equal to the average kinetic energy in the system, so the total energy is $\rho\omega^2 U^2$. We will equate the total energy to the sum of the incoherent scattered and coherent incident field, and we will assume that energy flows from the coherent to the incoherent field.

We let the vertical displacement field be given by

$$U = U_0 + U_1, \tag{A2}$$

where U_0 is referred to as the "background" field and U_1 is the "scattered" field. The elastic modulus fields are given by

$$(\lambda + 2\mu) = \overline{(\lambda + 2\mu)} + \delta(\lambda + 2\mu) \tag{A3}$$

and

$$\mu = \overline{\mu} + \delta\mu. \tag{A4}$$

Then to first order we have for the background field that

$$\rho\omega^2 U_0 = \overline{(\lambda + 2\mu)}(U_{0xx} + W_{0xz}) + \overline{\mu}(U_{0zz} - U_{0xz}). \tag{A5}$$

and

$$\rho\omega^2 U_1 = \delta(\lambda + 2\mu)(U_{0xx} + W_{0xz}) + \delta\mu(U_{0zz} - U_{0xz}) \qquad \text{A6}$$
$$+ \overline{(\lambda + 2\mu)}(U_{1xx} + W_{1xz}) + \overline{\mu}(U_{1zz} - U_{1xz}).$$

The first term in (A6) is a source term that represents the "equivalent" forces that give rise to the scattered field. The second term is easily recognized as the right side of the propagation equation from (A1). If to first order the scattered field and the incident field are not correlated,

$$<U_1 U_0> \approx 0,$$

then we can express the total energy as the energy of the scattered field plus the energy of the incident (or coherent) field,

$$E = \rho\omega^2 <U^2> = \frac{1}{2}\rho\omega^2[U_0^2 + U_1^2]. \qquad \text{A7}$$

Since the energy in the scattered field must arise from the coherent field, we see that the source of energy must be proportional to the square of the source term in (A6),

$$f_u^2 = [\delta(\lambda + 2\mu)(U_{0xx} + W_{0xz})]^2. \qquad \text{A8}$$

Similarly, we have that

$$f_w^2 = [\delta(\lambda + 2\mu)(U_{0xz} + W_{0zz}) + \delta\mu(W_{0xx} - U_{0xz})]^2. \qquad \text{A9}$$

The assumption is that energy transfer is unidirectional from the coherent field to the scattered field, so $Q^{-1} \sim \frac{\delta E_0}{E_0}$ and $\delta E_0 \sim -\delta E_1$. Naturally, if the heterogeneity modifies the mode of the incident wave then replacement of U_1 by the eigenfunction of the half-space Rayleigh wave is not acceptable. Also, if energy passes from the scattered field back to a forward propagating Rayleigh wave mode (as may be the case for the folded layers) then resonance is established and this perturbation method is inadequate.

In order to compute the total equivalent scattering energy-flux for our 2-D model, we integrate over the depth and range for which the velocity perturbations are non-trivial. We divide by the range in order to obtain a range-independent quantity. This assumes spatial stationarity so that integration over range is the same as propagation over a suite of random media with the same statistics.

$$\xi = \frac{1}{\Delta}\iint (f_u^2 + f_w^2)\,dz\,dx \approx <\int (f_u^2 + f_w^2)\,dz>. \qquad \text{A10}$$

The result that attenuation is not directly proportional to ξ for fixed *ka* implies that some multiple scattering is present and that a simple energy flow from the slowly decaying Rayleigh wave into body waves is not an entirely adequate conceptual model. Also, we have assumed that the weak velocity heterogeneity does not perturb on average either the Rayleigh-wave phase velocity nor the eigenfunctions.

(THIS PAGE INTENTIONALLY LEFT BLANK)

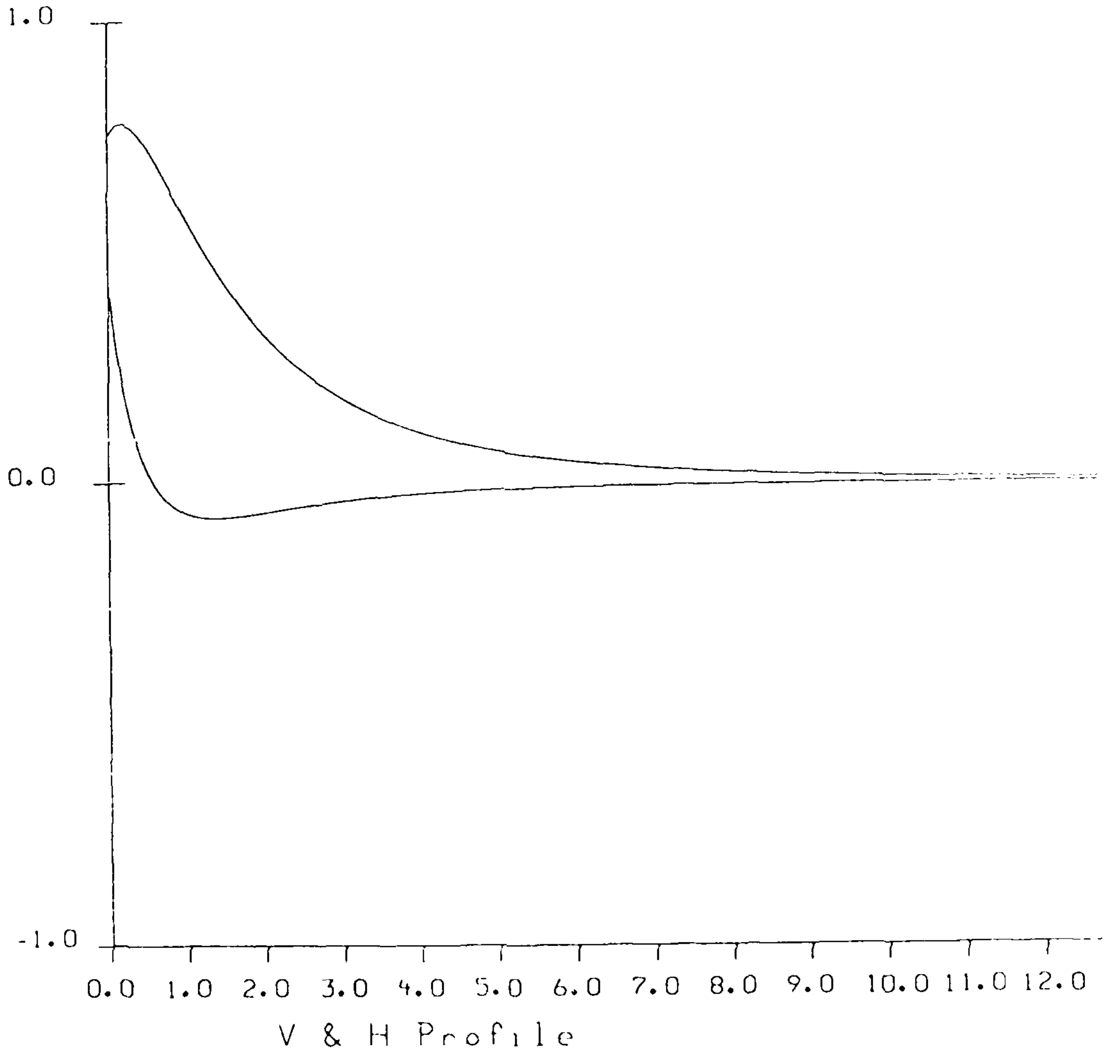

Fig.1

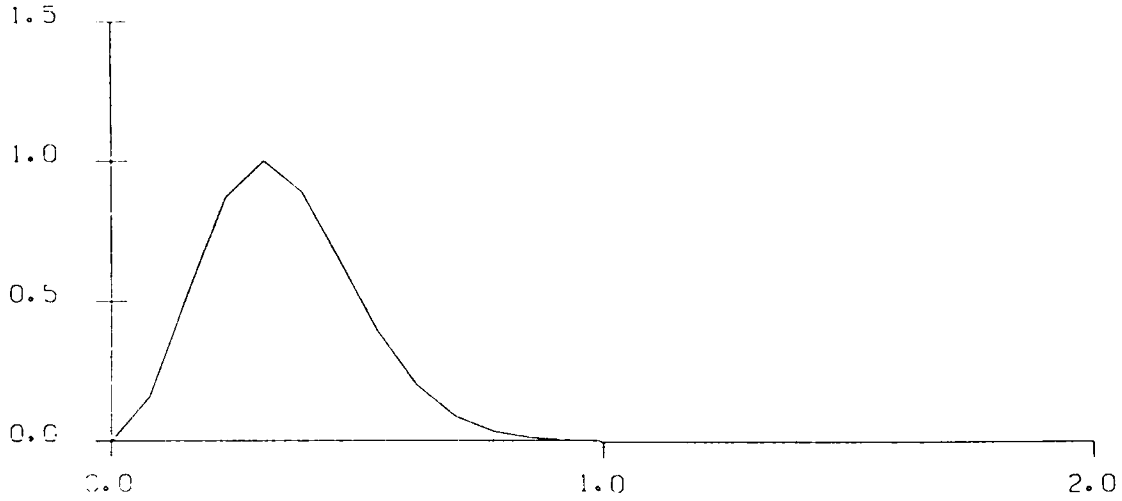

AMPLITUDE vs WAVENUMBER(Cycles/km)

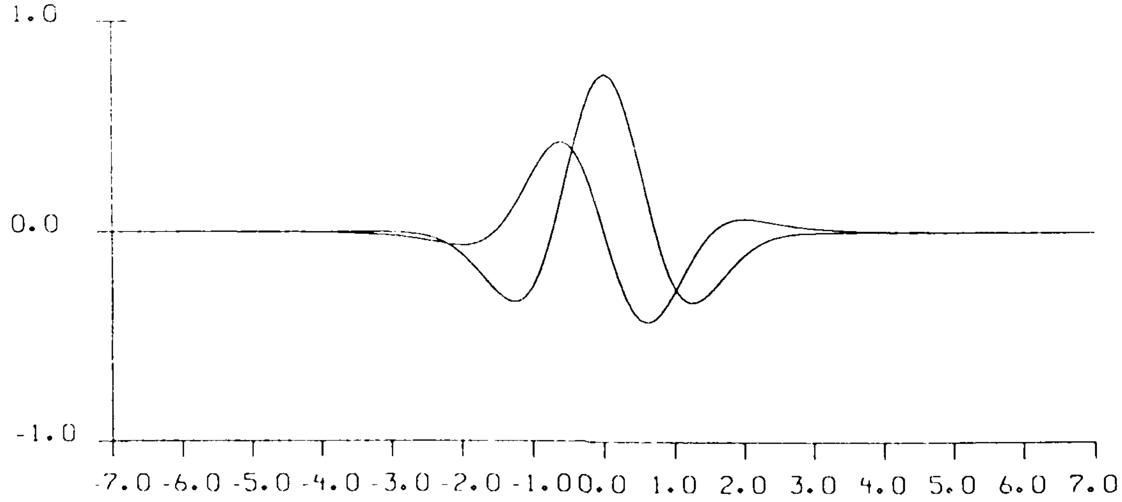

SPATIAL WAVEFORMS (V & H)

Fig.2

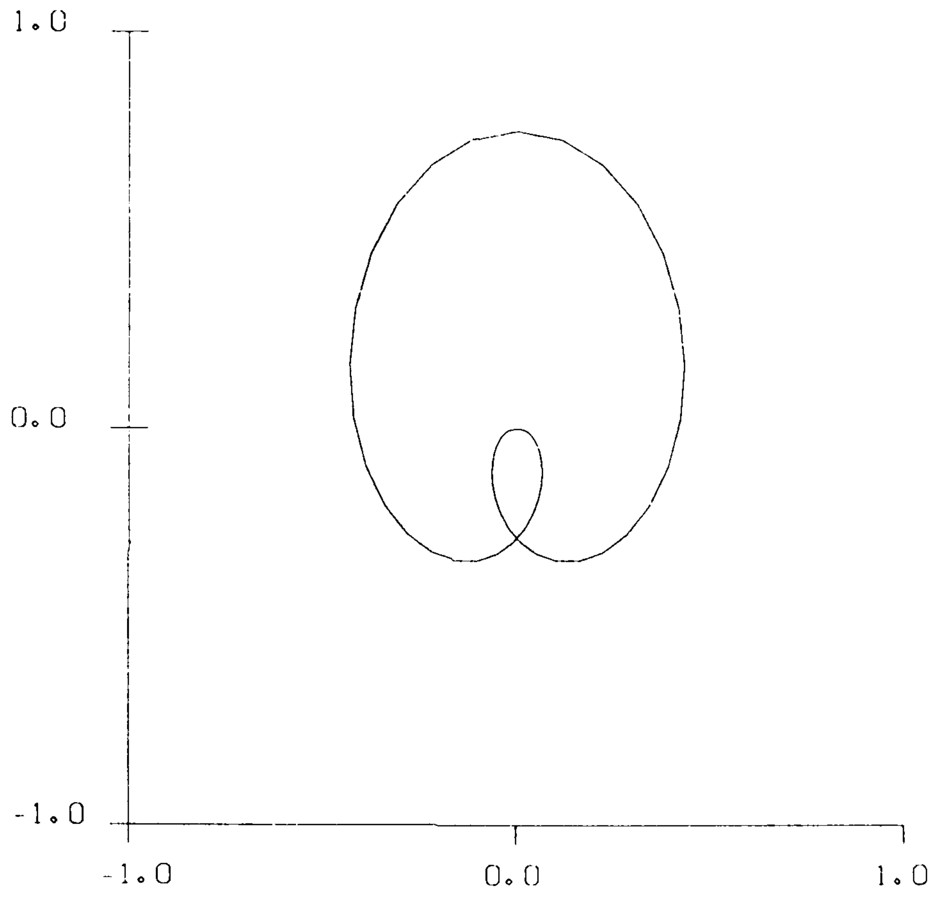

Particle Motion Fig.3

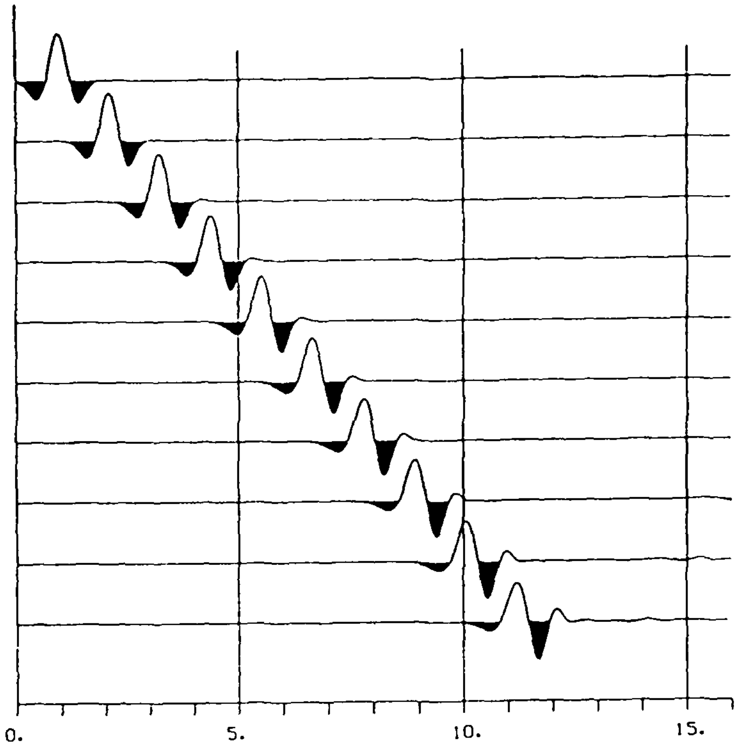

VERT,Half-Space,3km

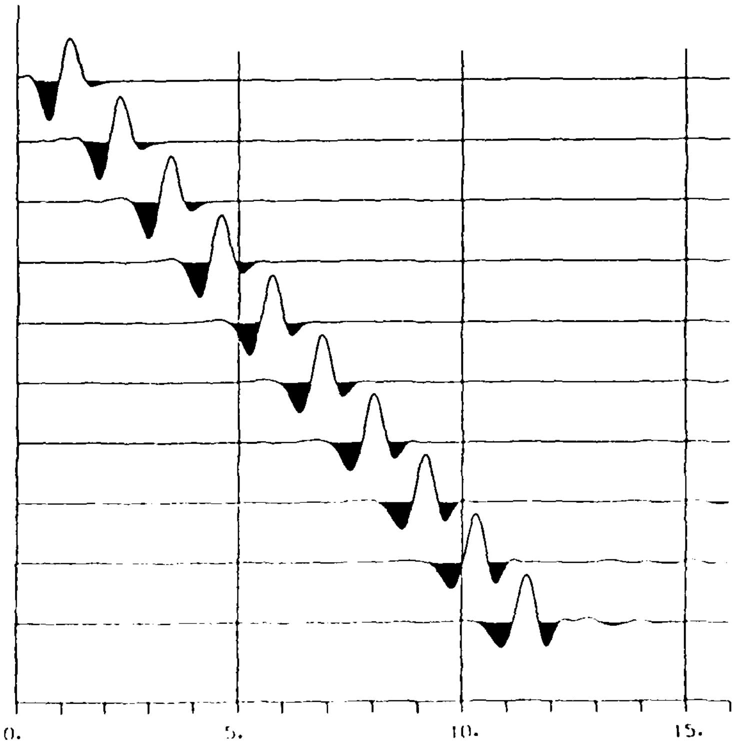

HORI,Half-Space,3km

Fig.4

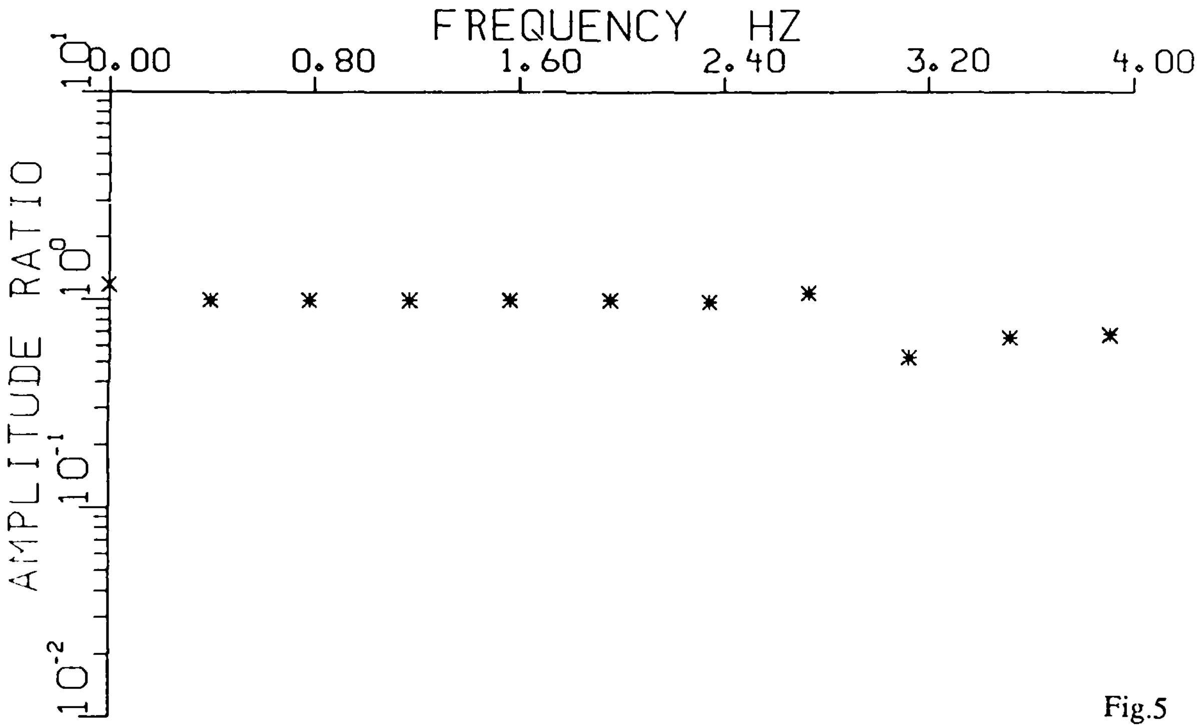
FREQUENCY HZ
0.00
0.80
1.60
2.40
3.20
4.00
AMPLITUDE RATIO
10^{1}
10^{0}
10^{-1}
10^{-2}

Fig.5

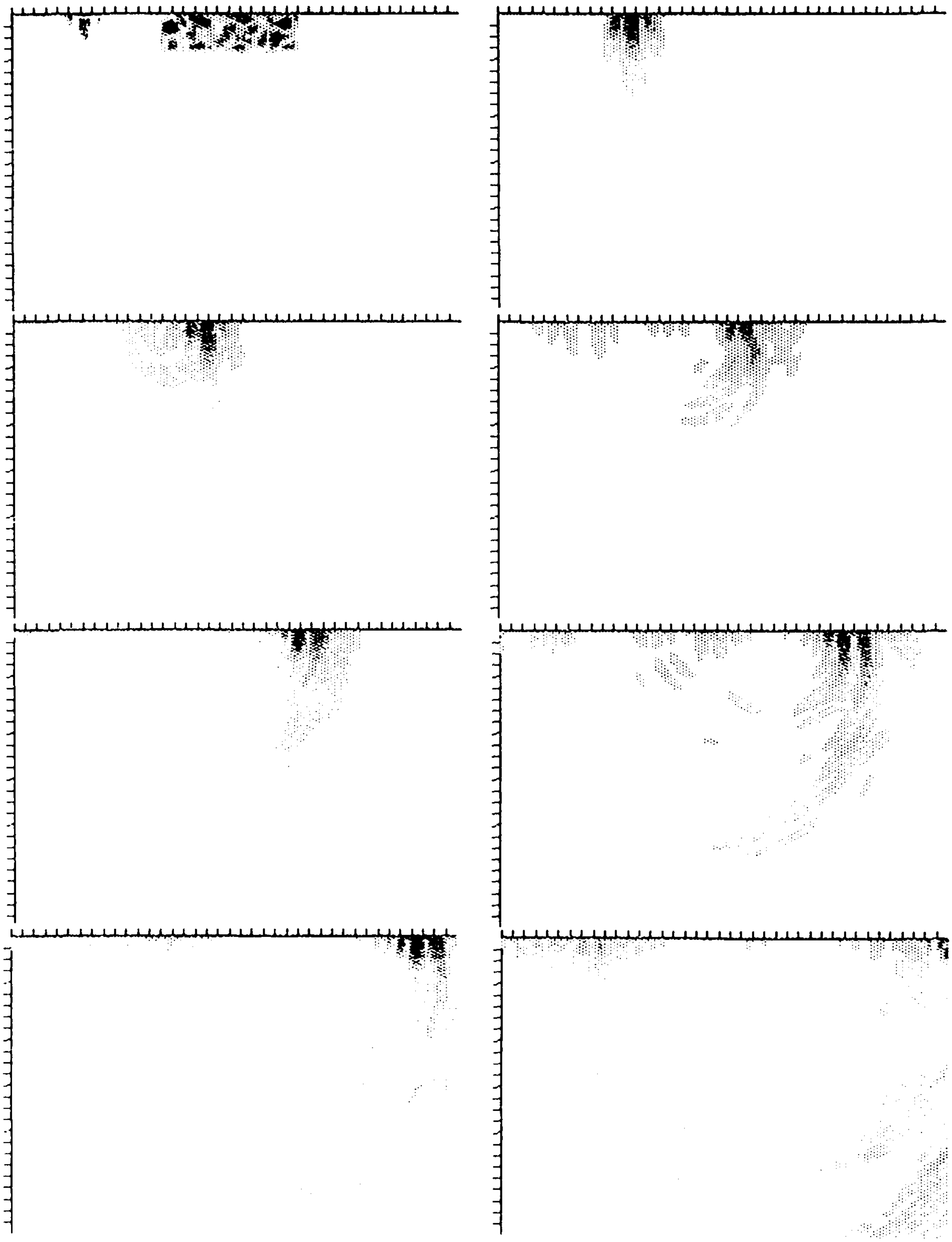

Fig.6A

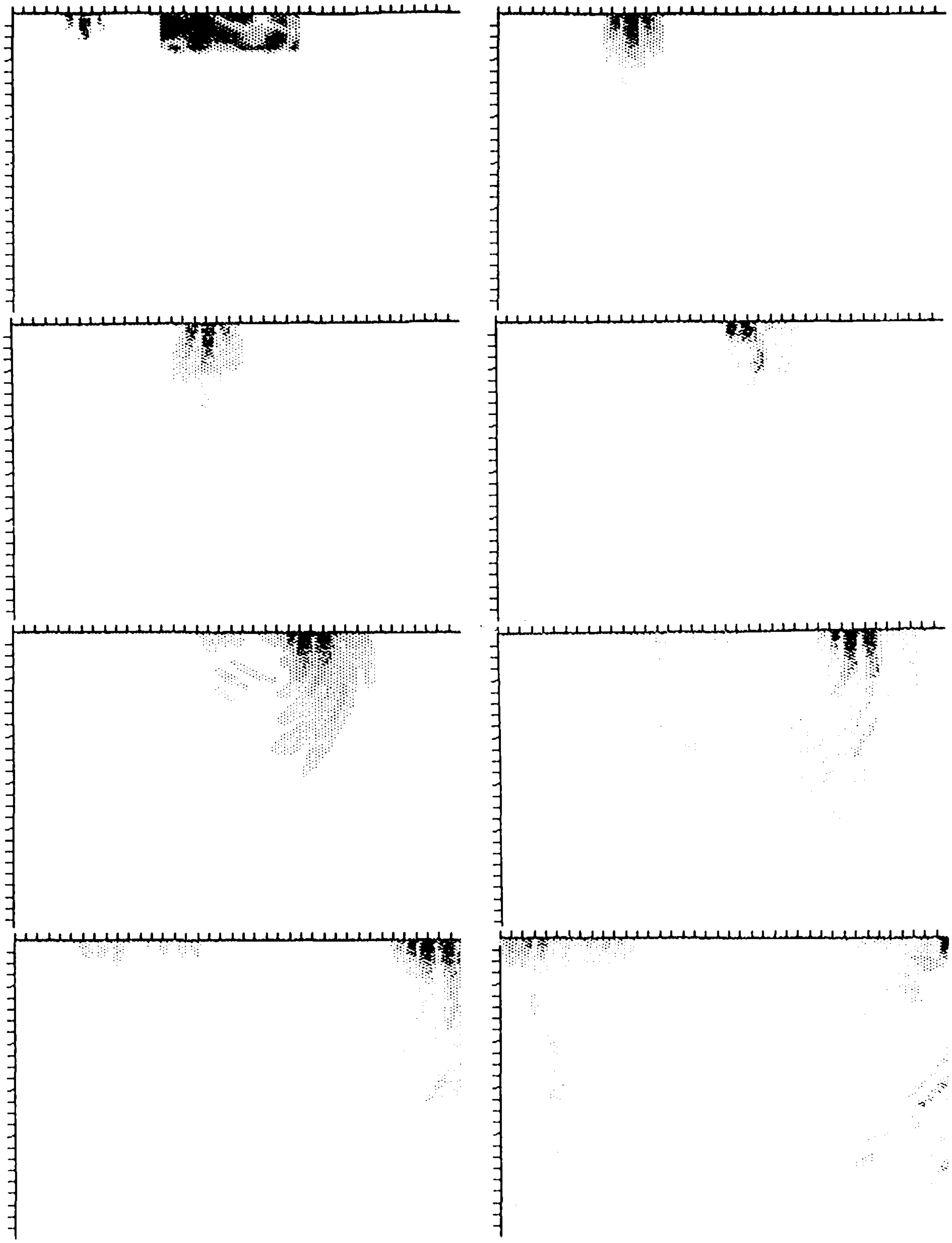

Fig.6B

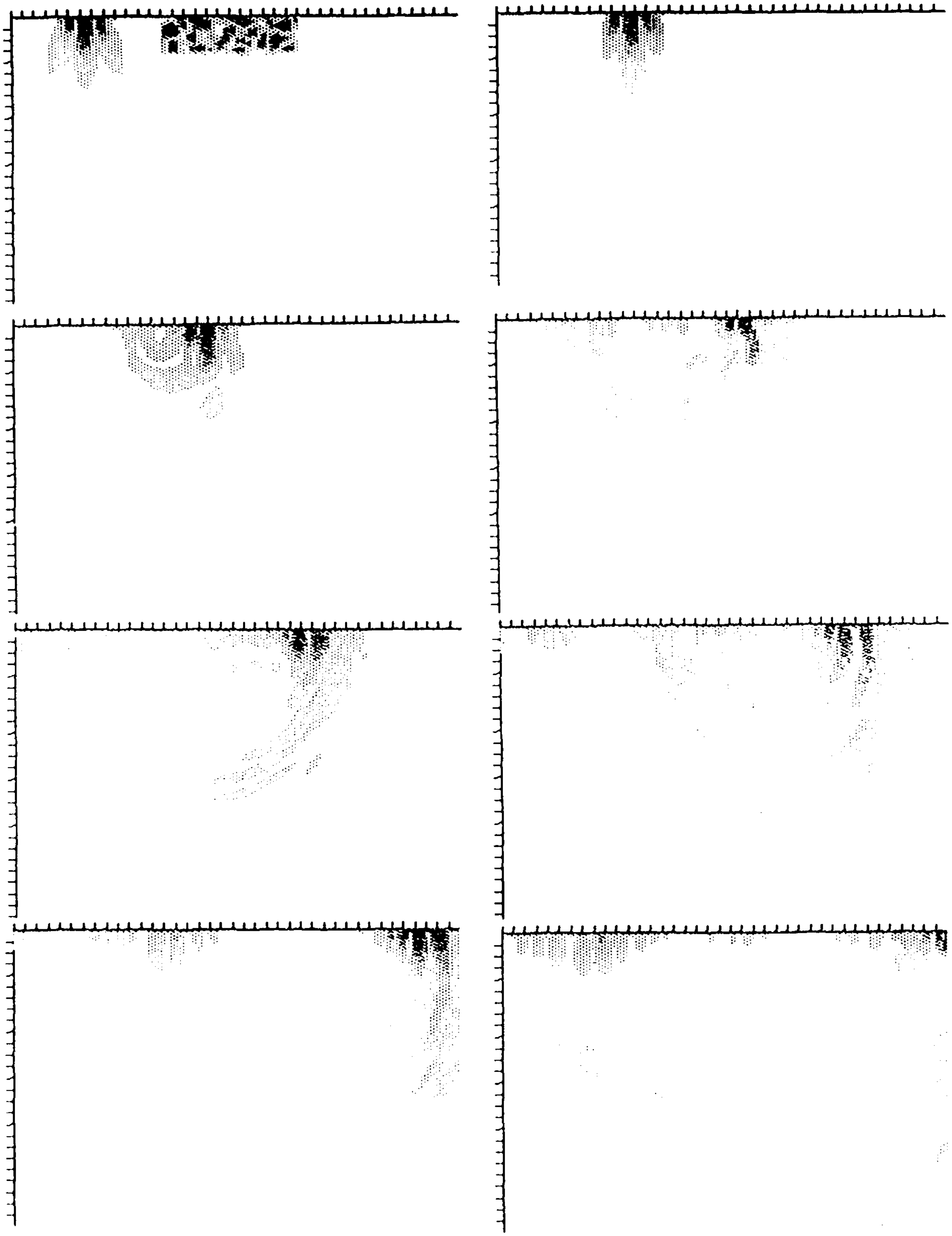

Fig.6C

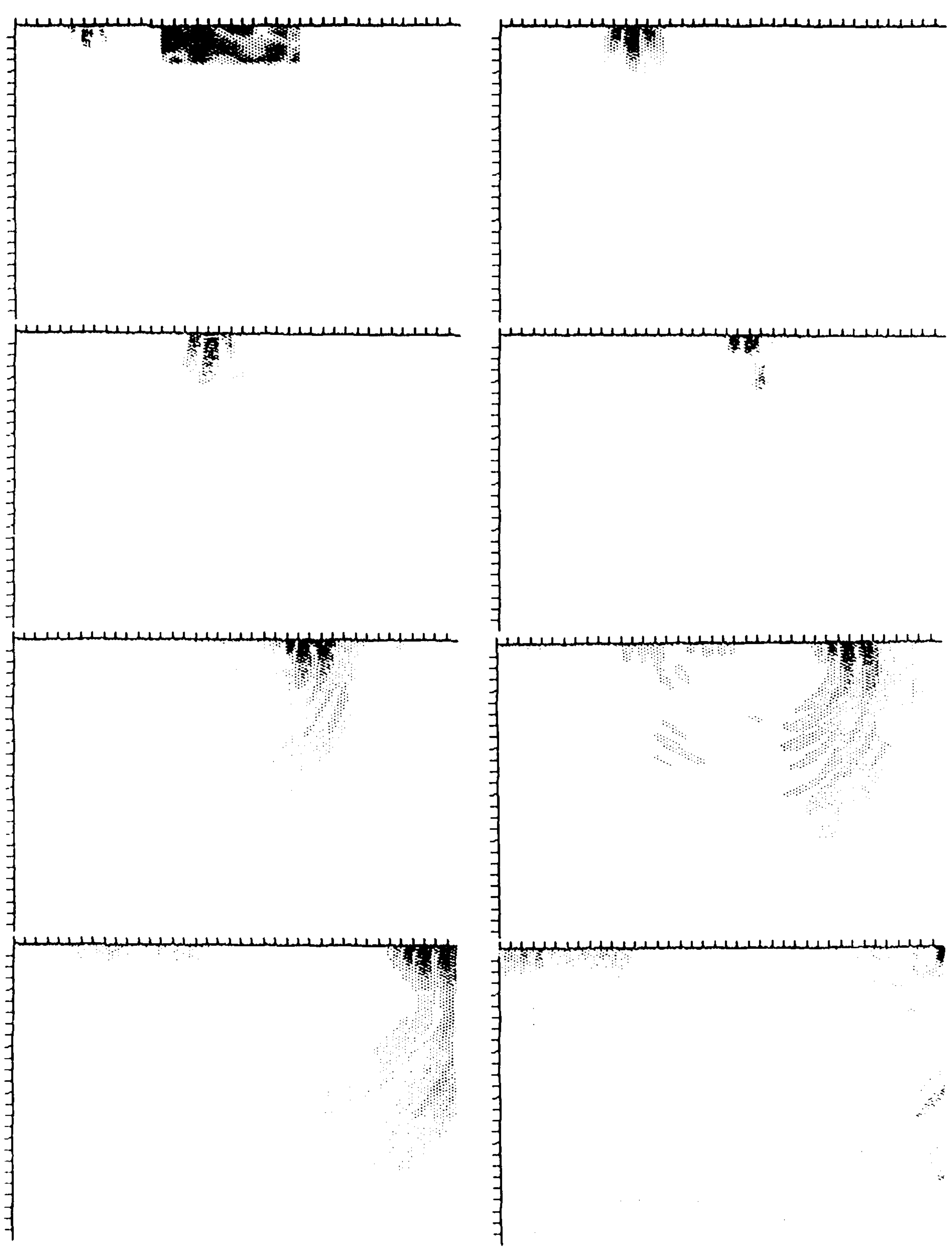

Fig.6D

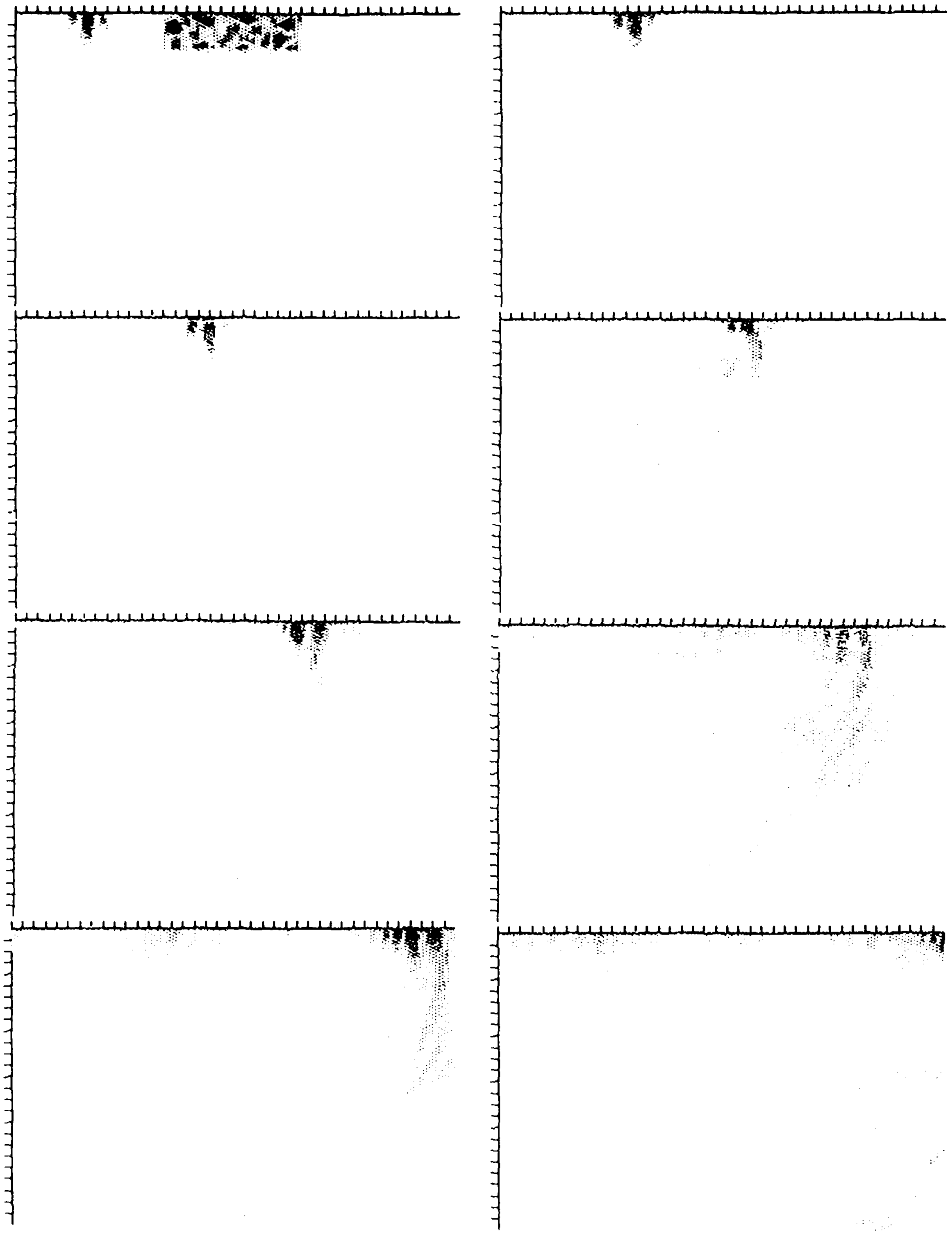

Fig.6E

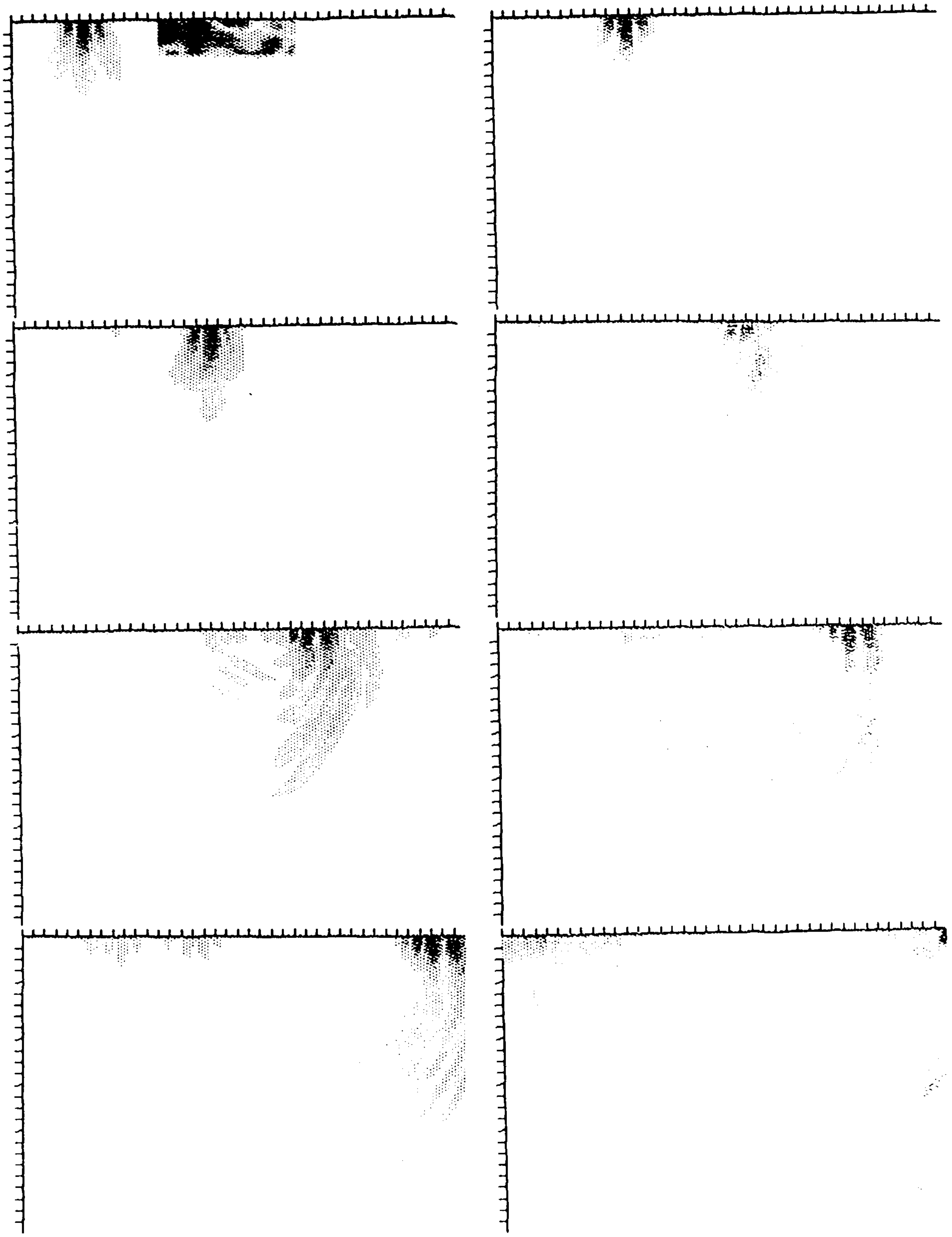

Fig.6F

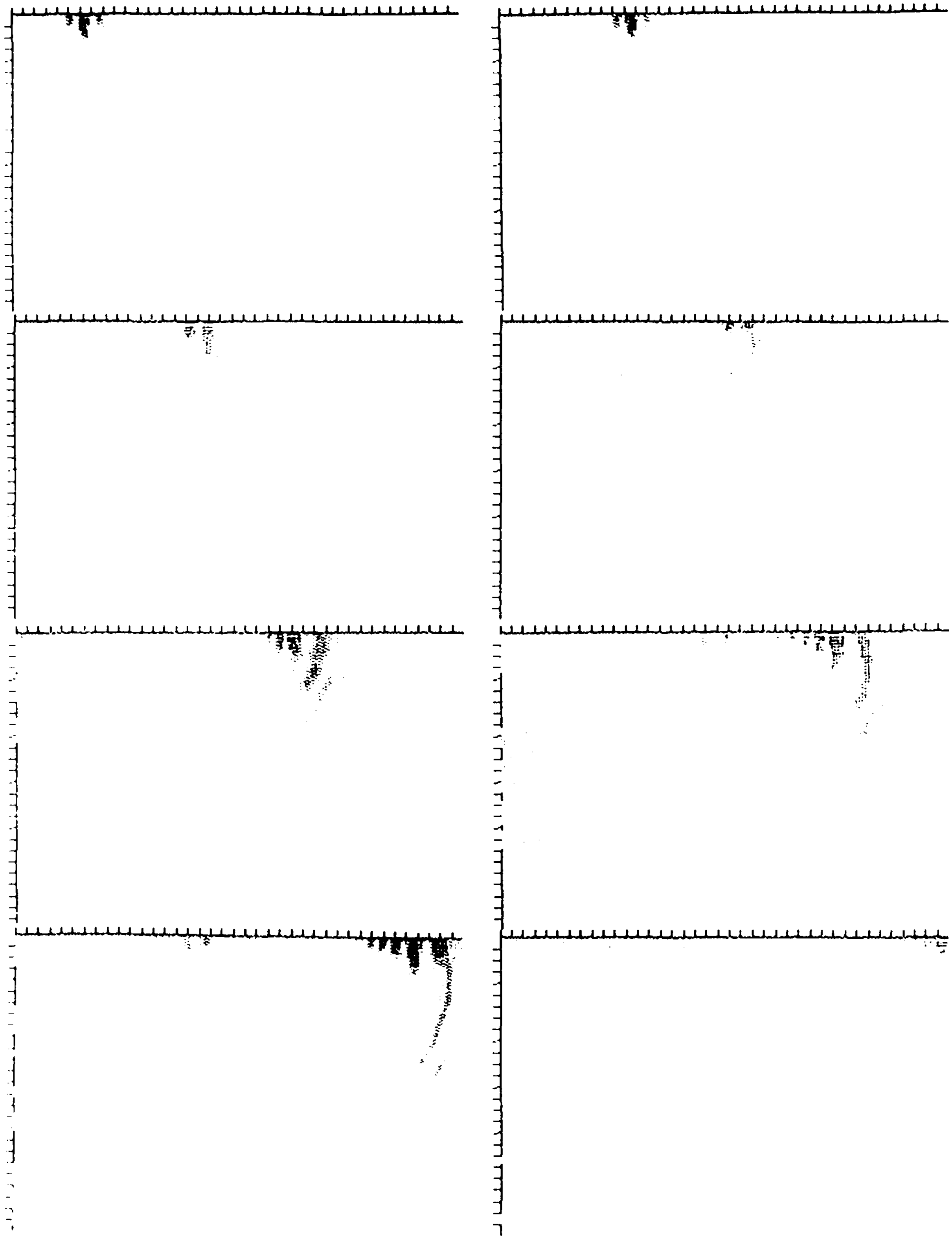

Fig.6G

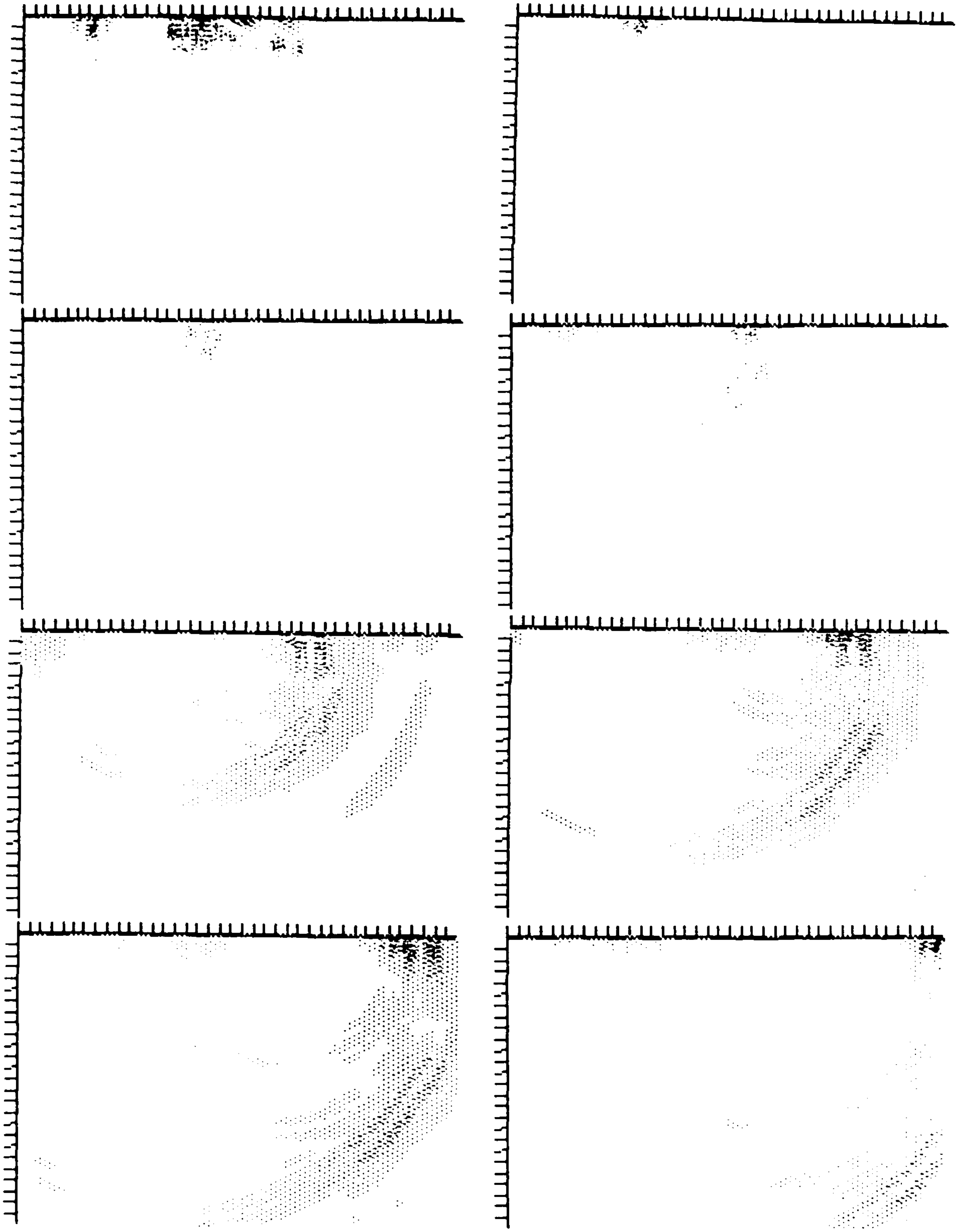

Fig.6H

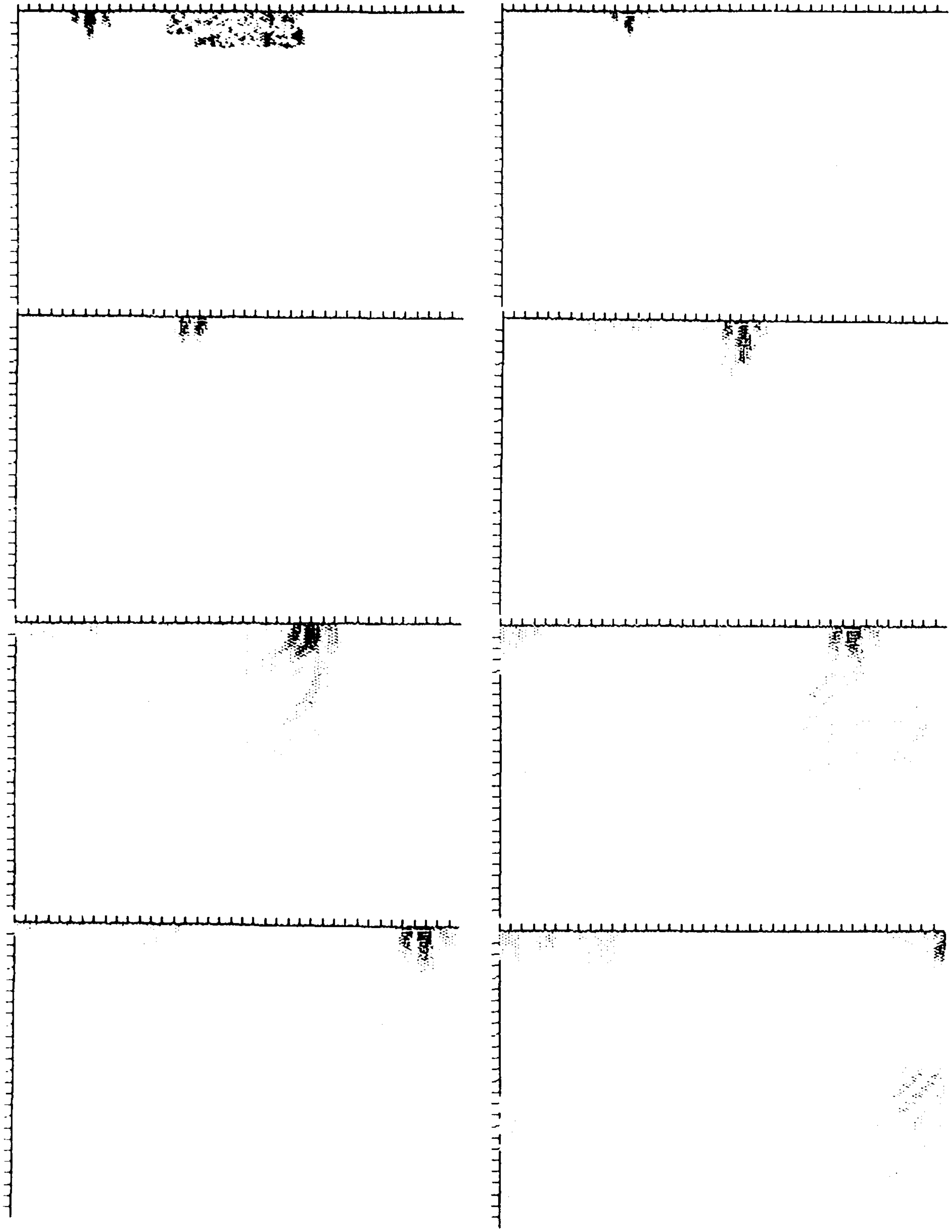

Fig.6I

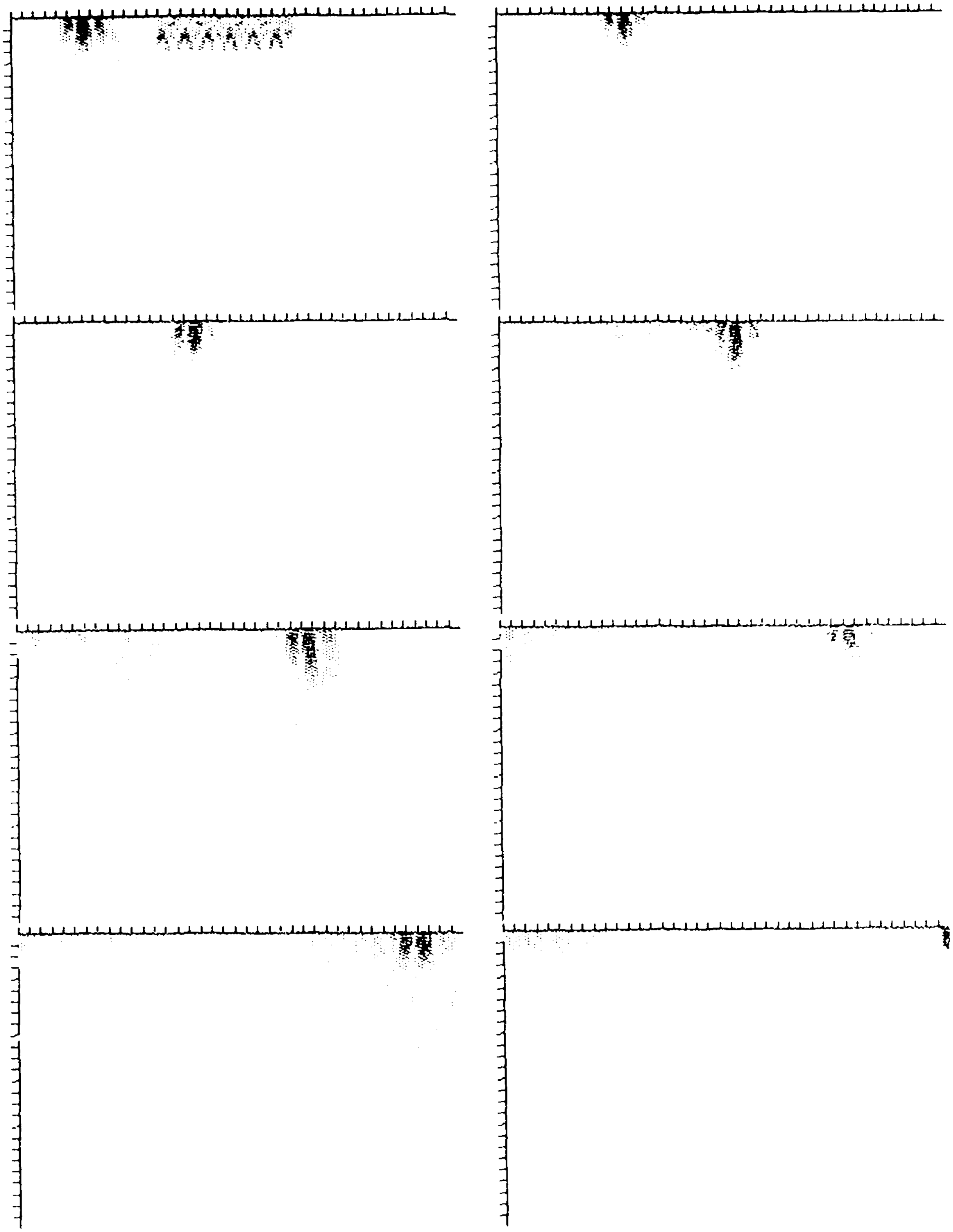

Fig.6J

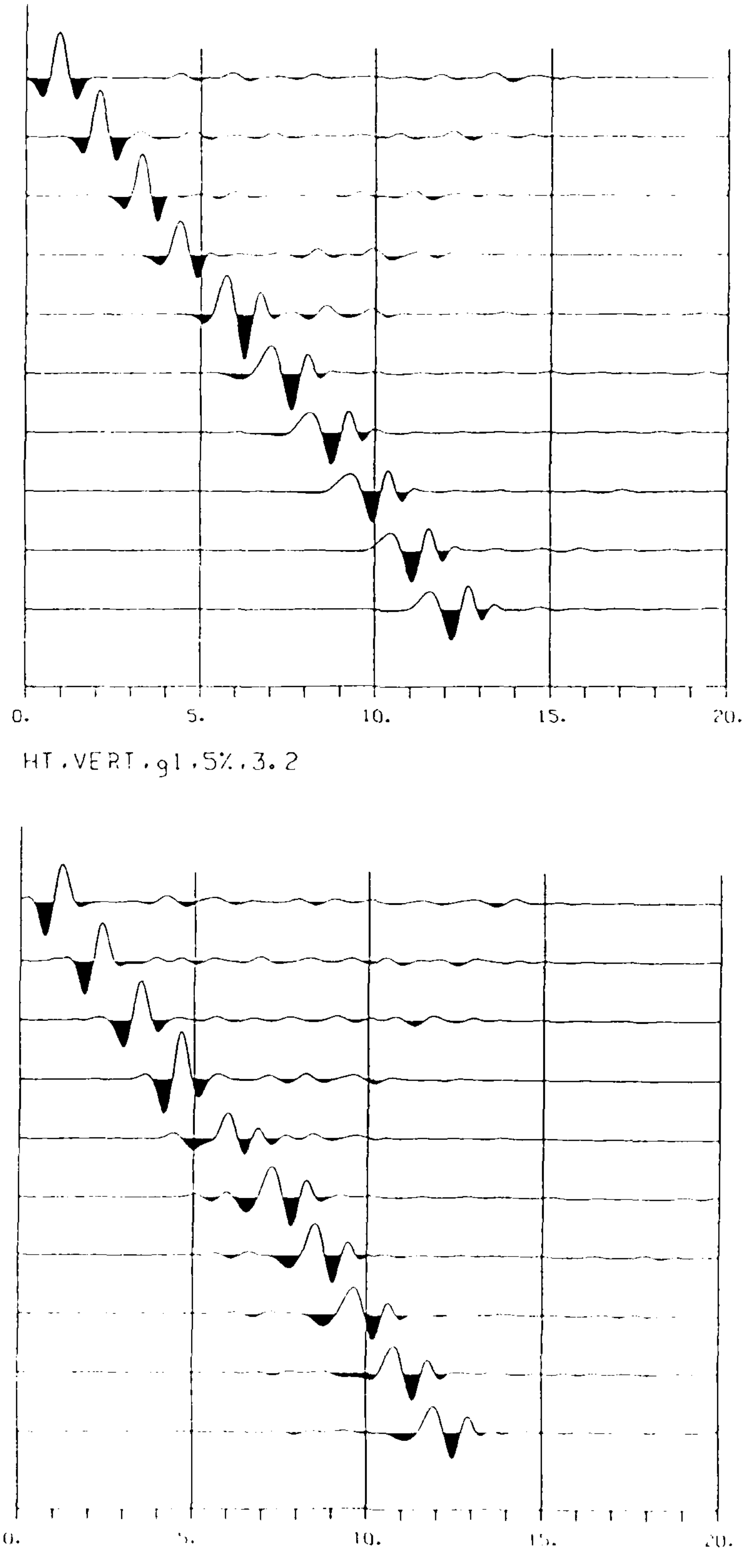

Fig.7A

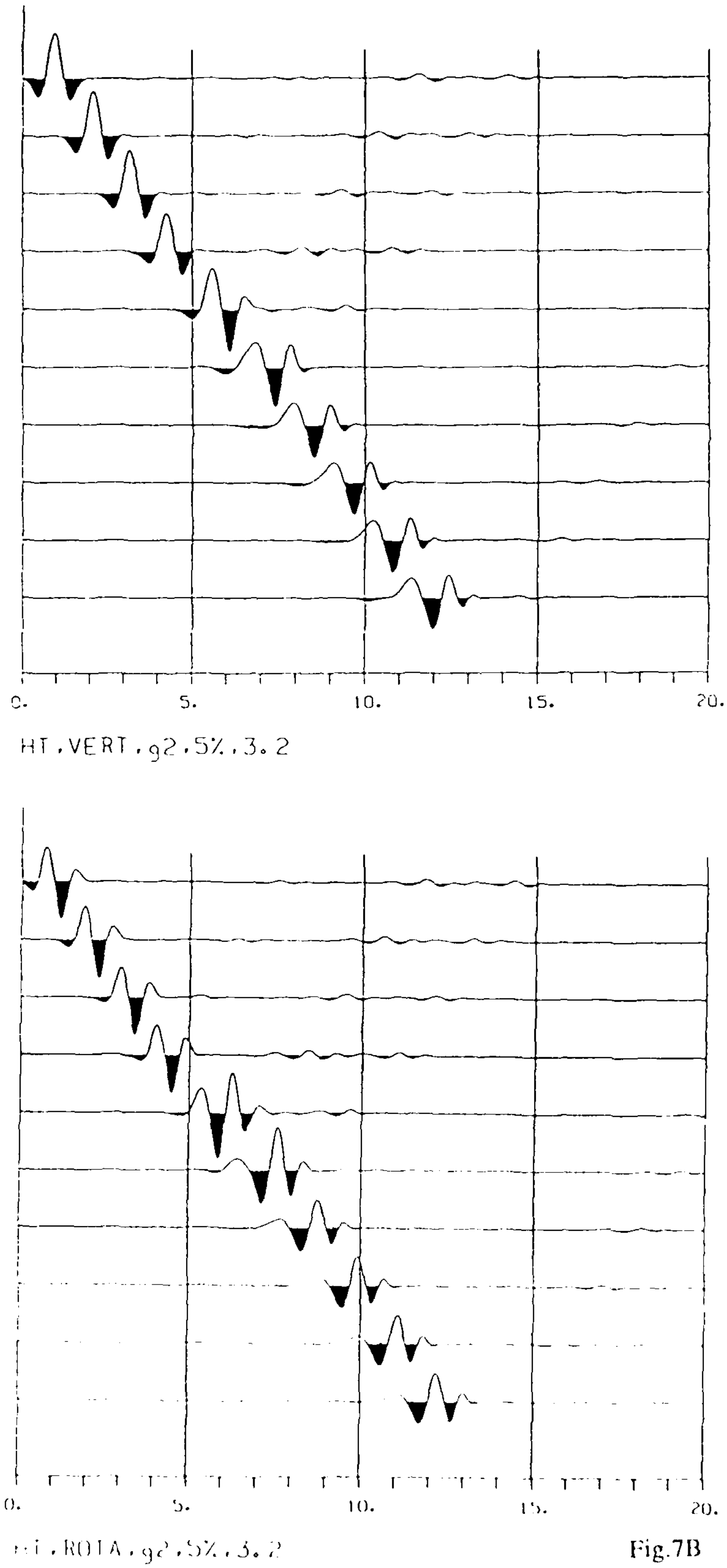

Fig.7B

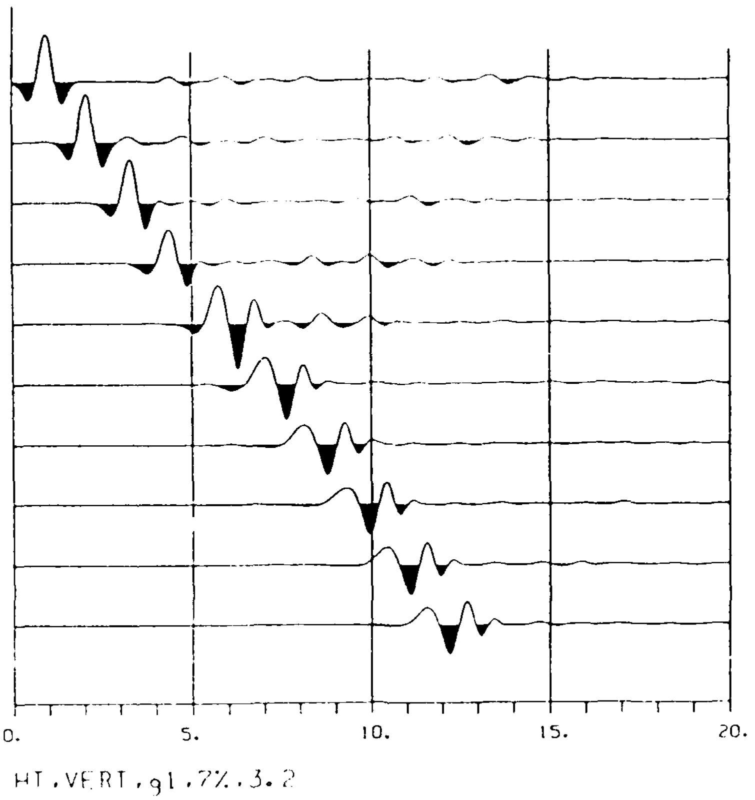

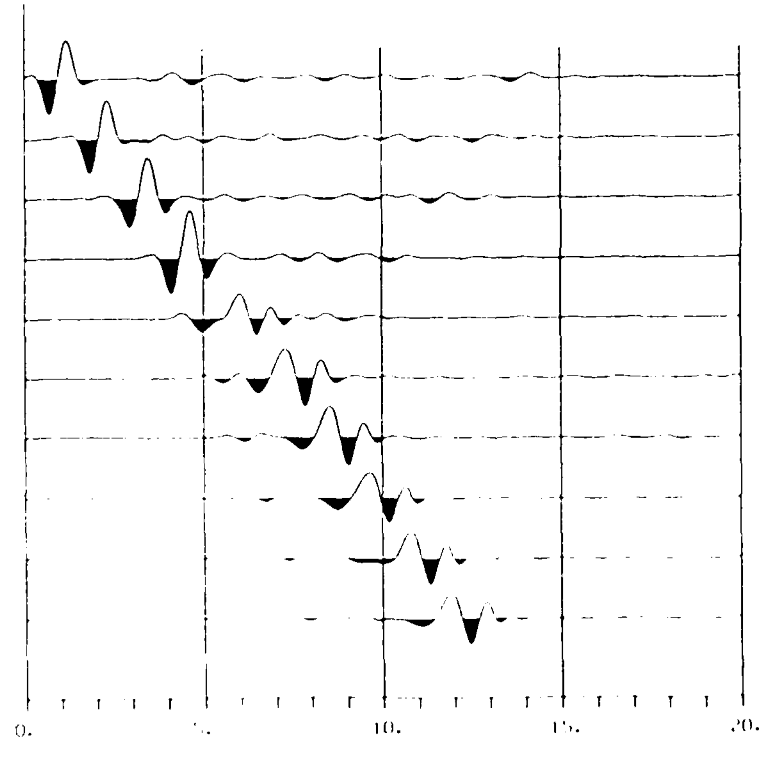

Fig.7C

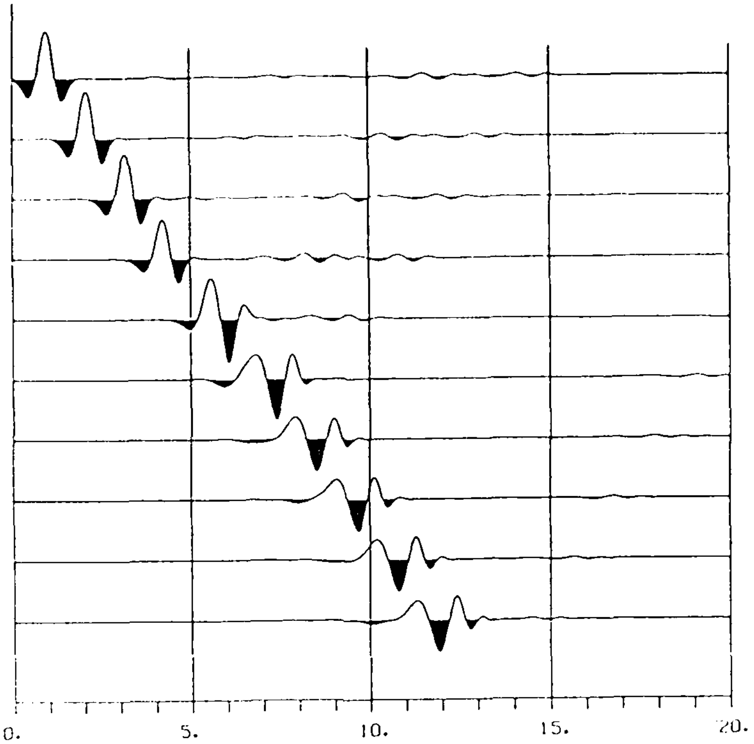

HT,VERT,g2,7%,3.2

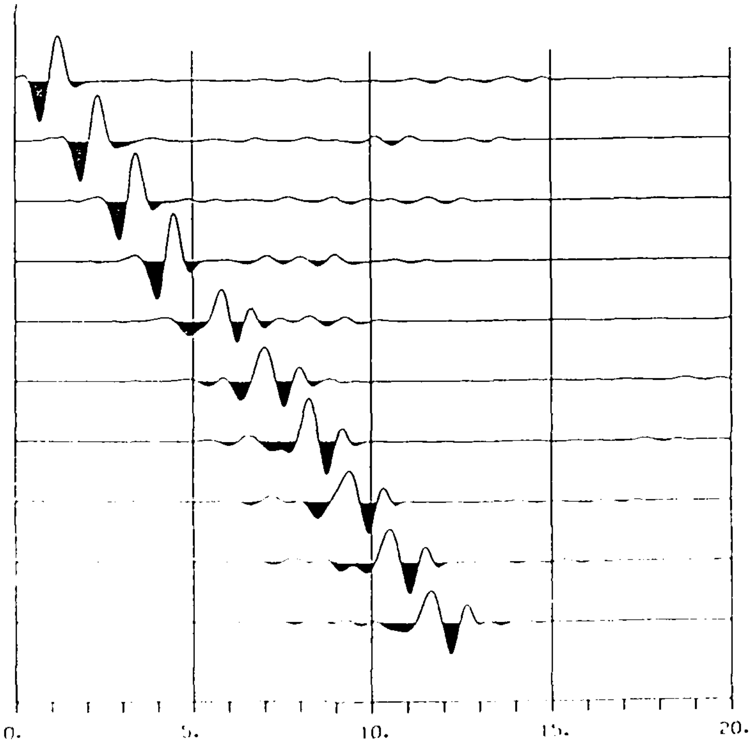

HT,HORI,g2,7%,3.2

Fig.7D

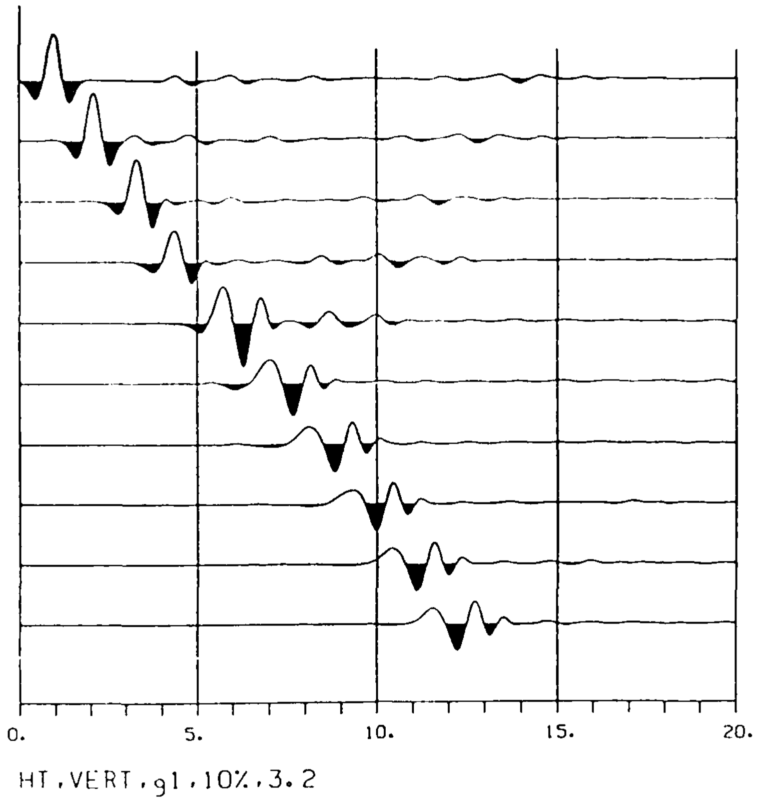

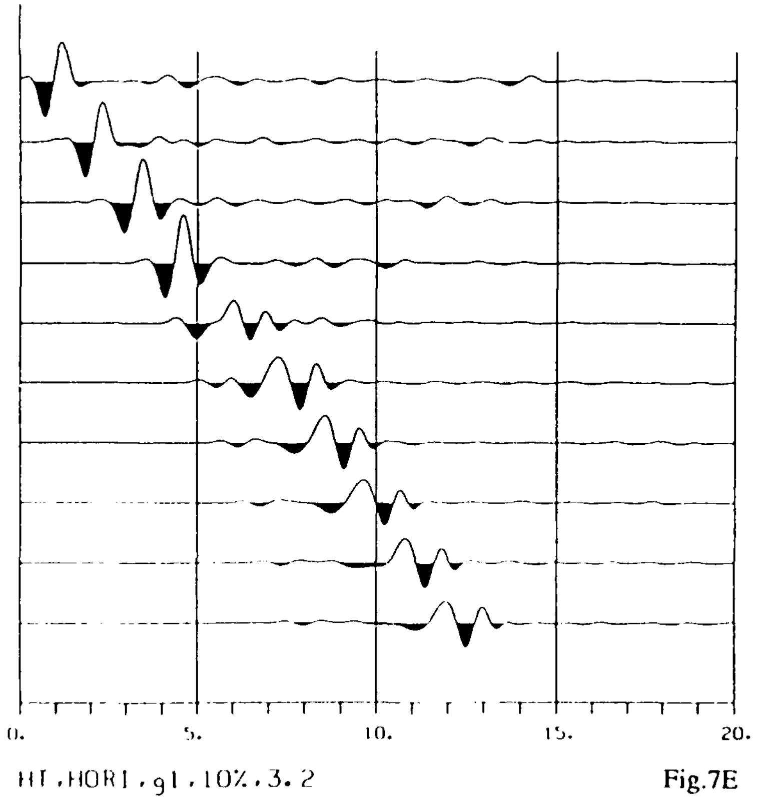

Fig.7E

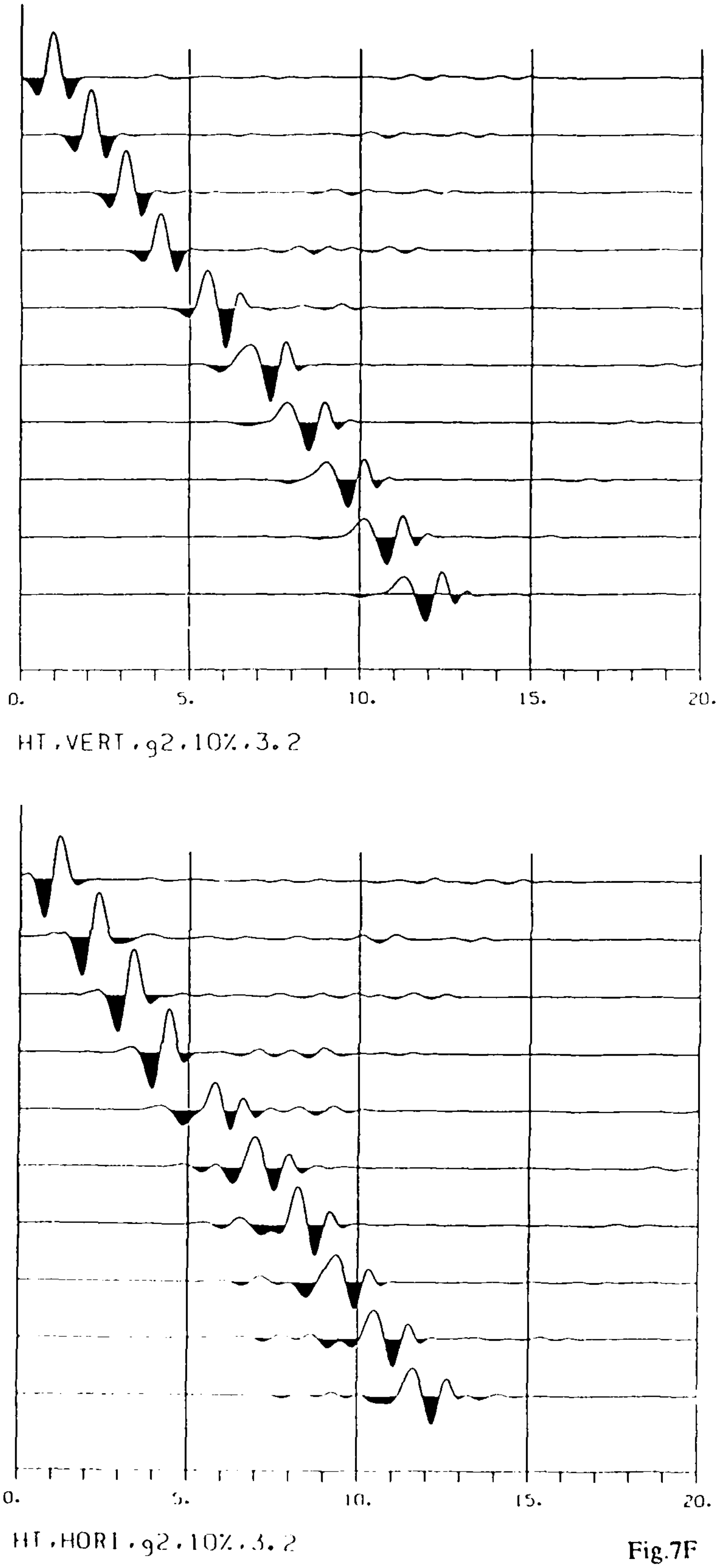

Fig.7F

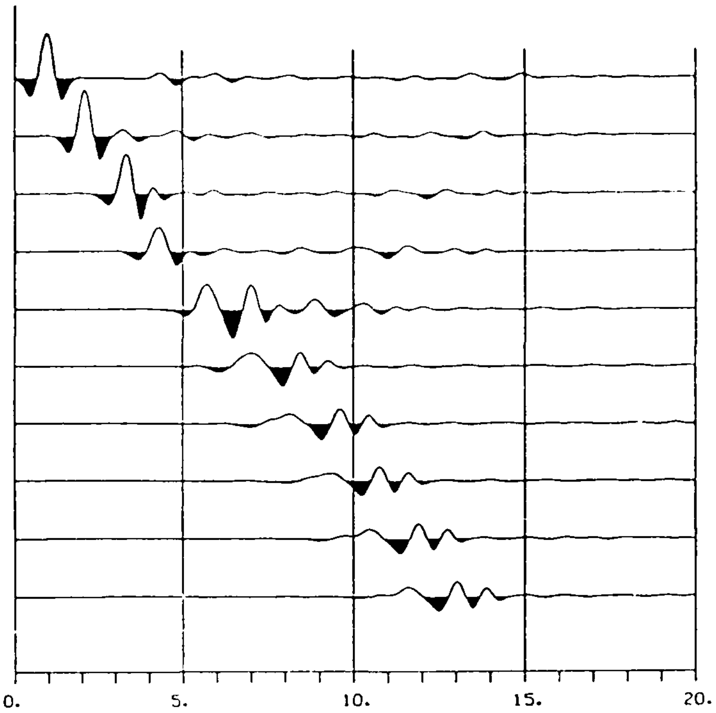

HT.VERT.g1.20%.3.2

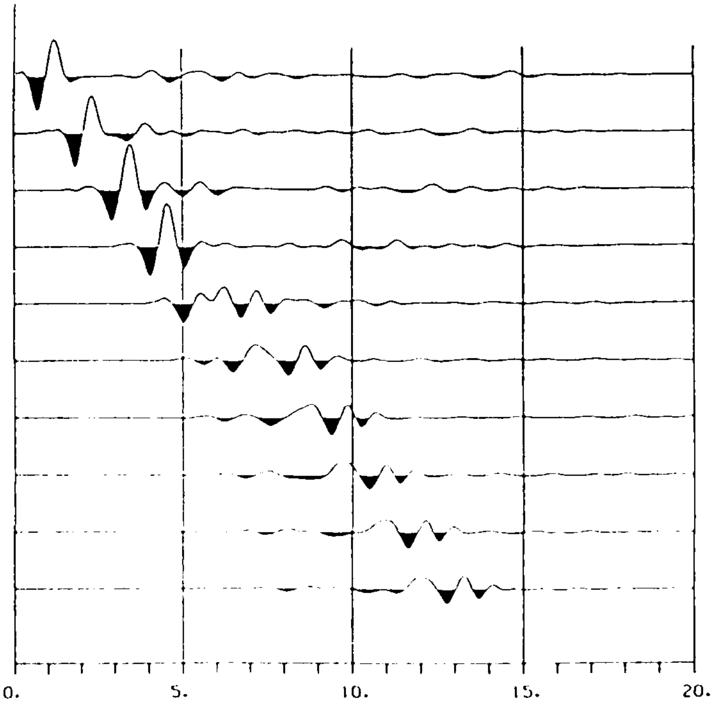

HT.HORI.g1.20%.3.2

Fig.7G

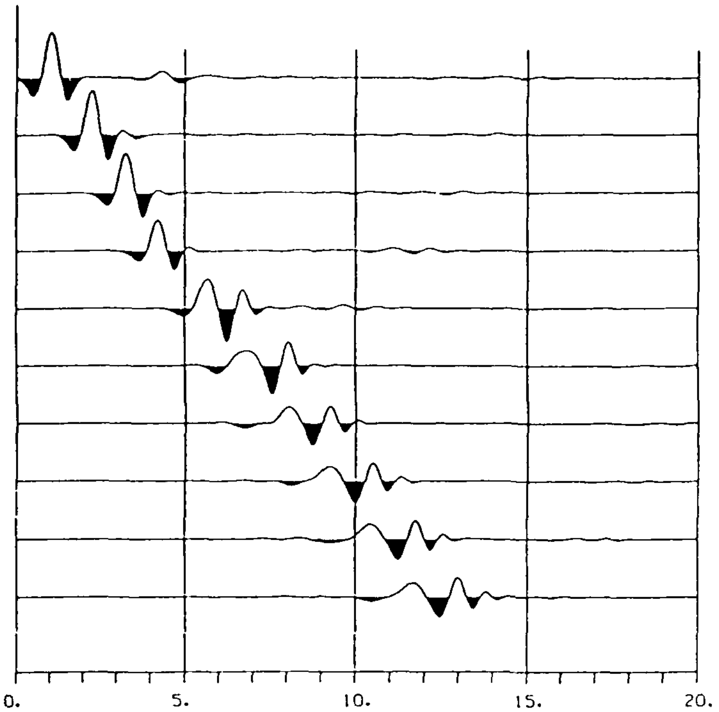

HT,VERT,a2,20%,3.2

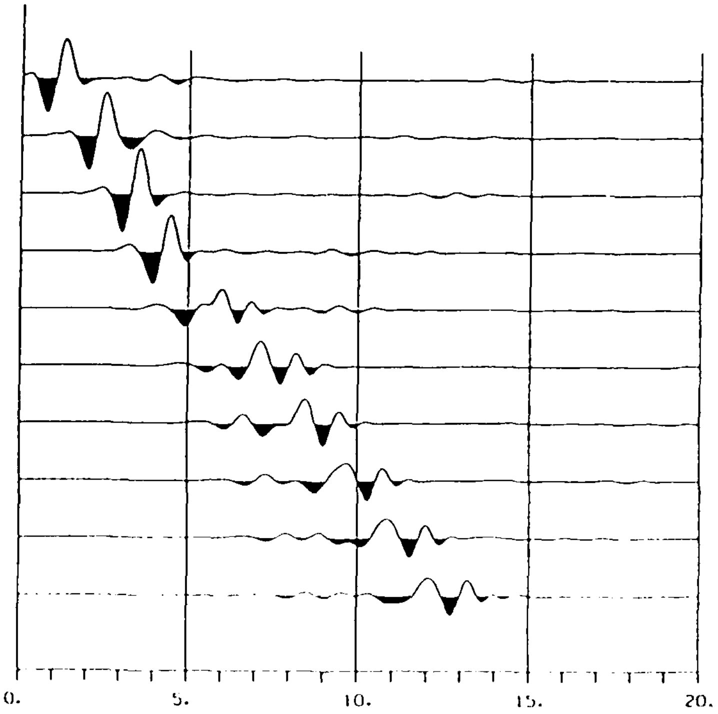

HT,HORI,a2,20%,3.2

Fig.7H

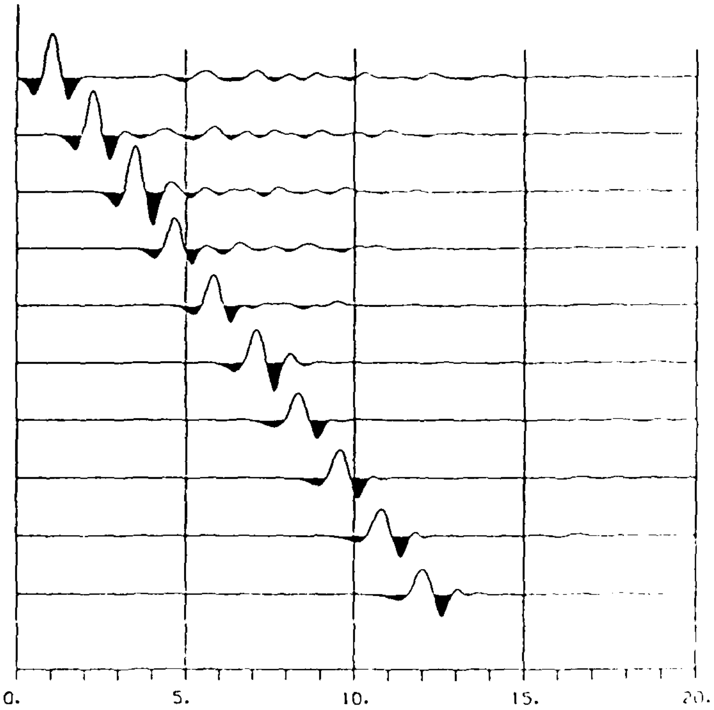

HT,VERT, ,ss,3.2

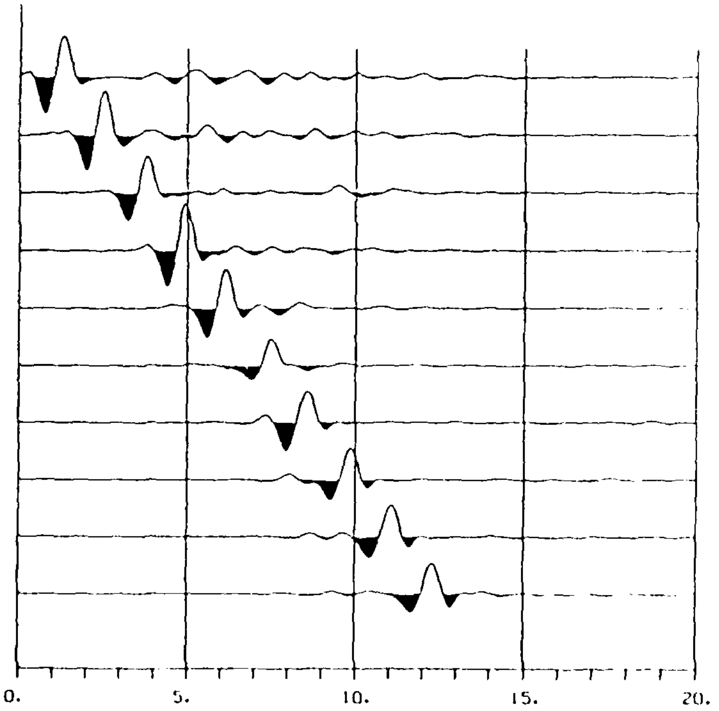

HT,HORI, ,ss,3.2

Fig.7l

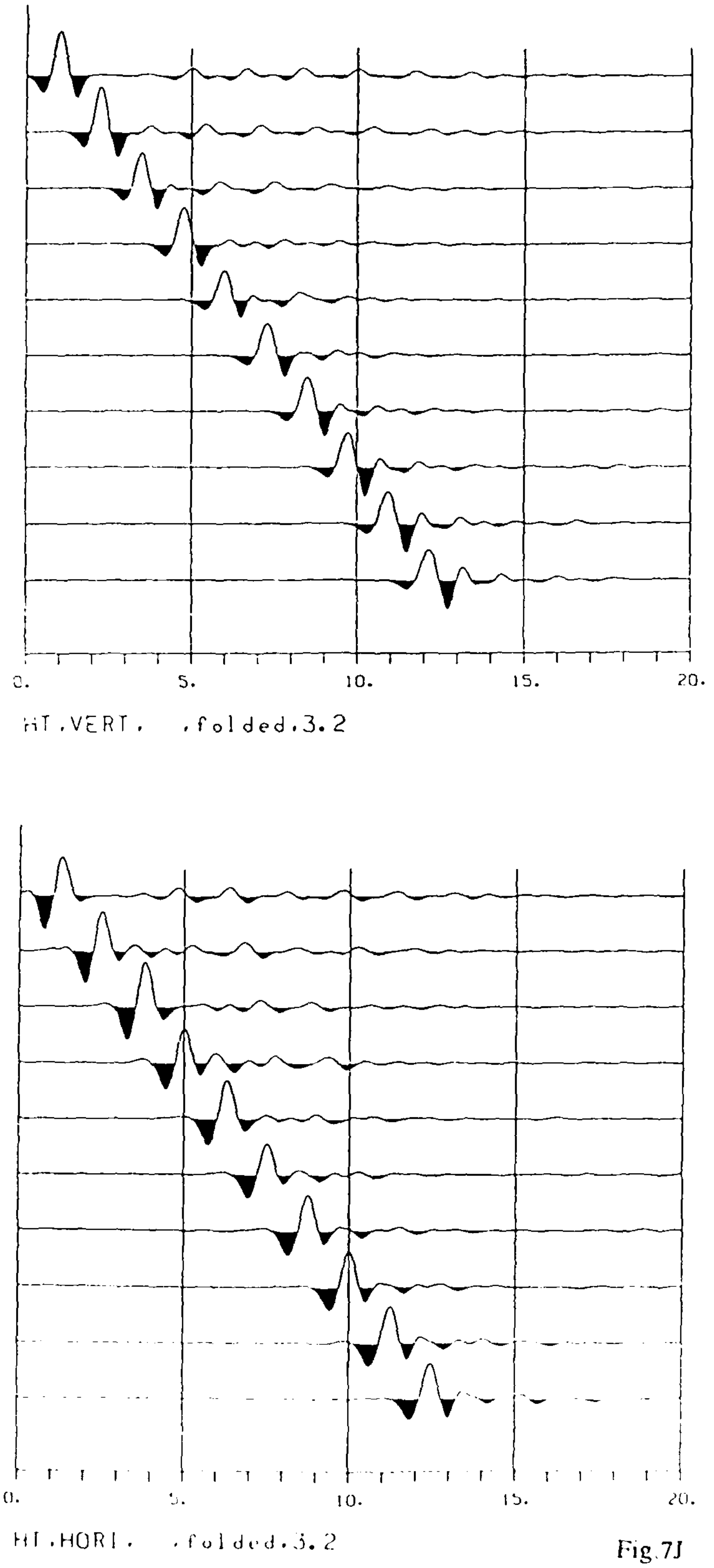

Fig.7J

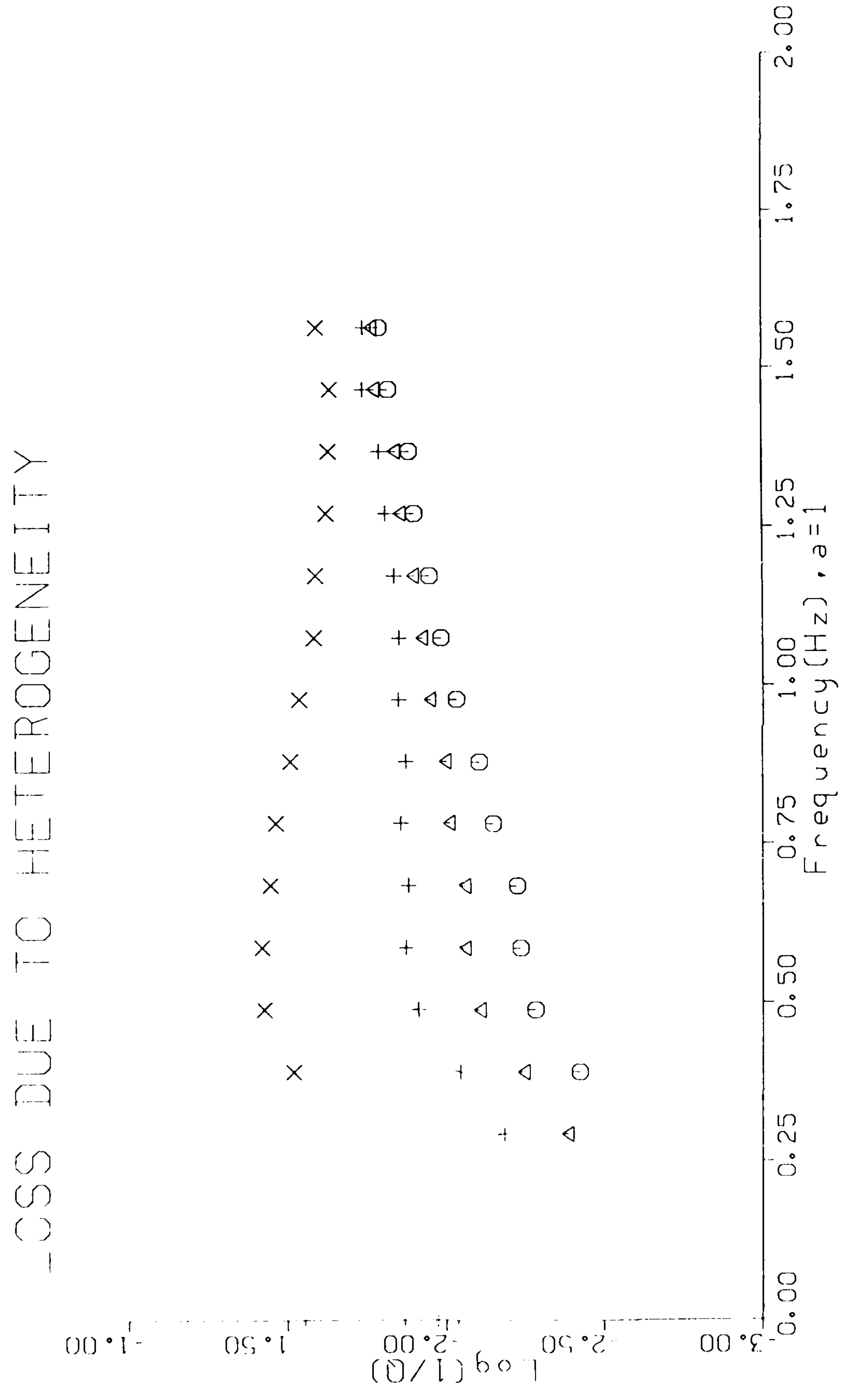
LOSS DUE TO HETEROGENEITY
Frequency(Hz), a=1
0.00
0.25
0.50
0.75
1.00
1.25
1.50
1.75
2.00
Log(1/Q)
-3.00
-2.50
-2.00
-1.50
-1.00

Fig.8A

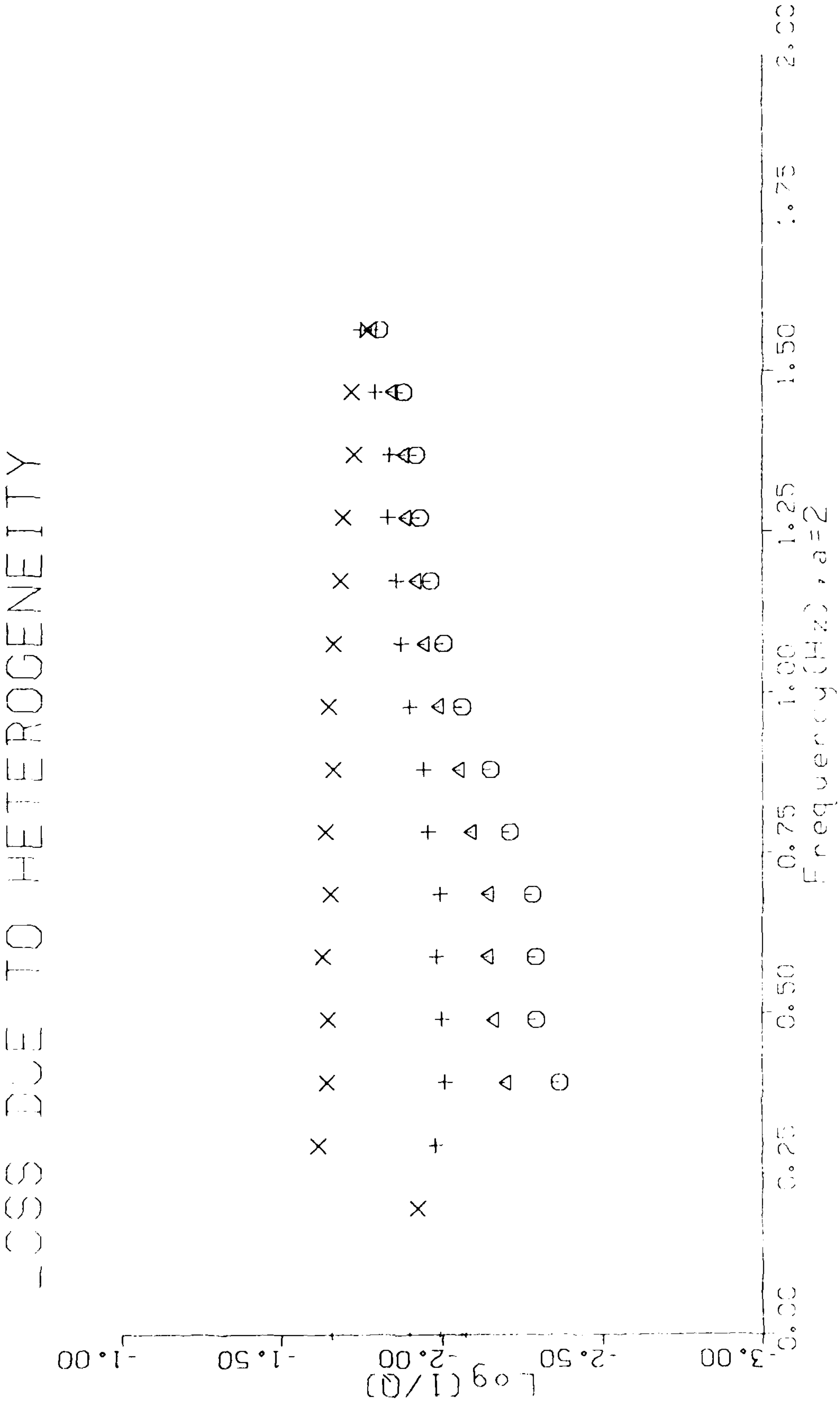
LOSS DUE TO HETEROGENEITY
Frequency(Hz), a=2
0.00
0.25
0.50
0.75
1.00
1.25
1.50
1.75
2.00
Log(1/Q)
-1.00
-1.50
-2.00
-2.50
-3.00

Fig.8B

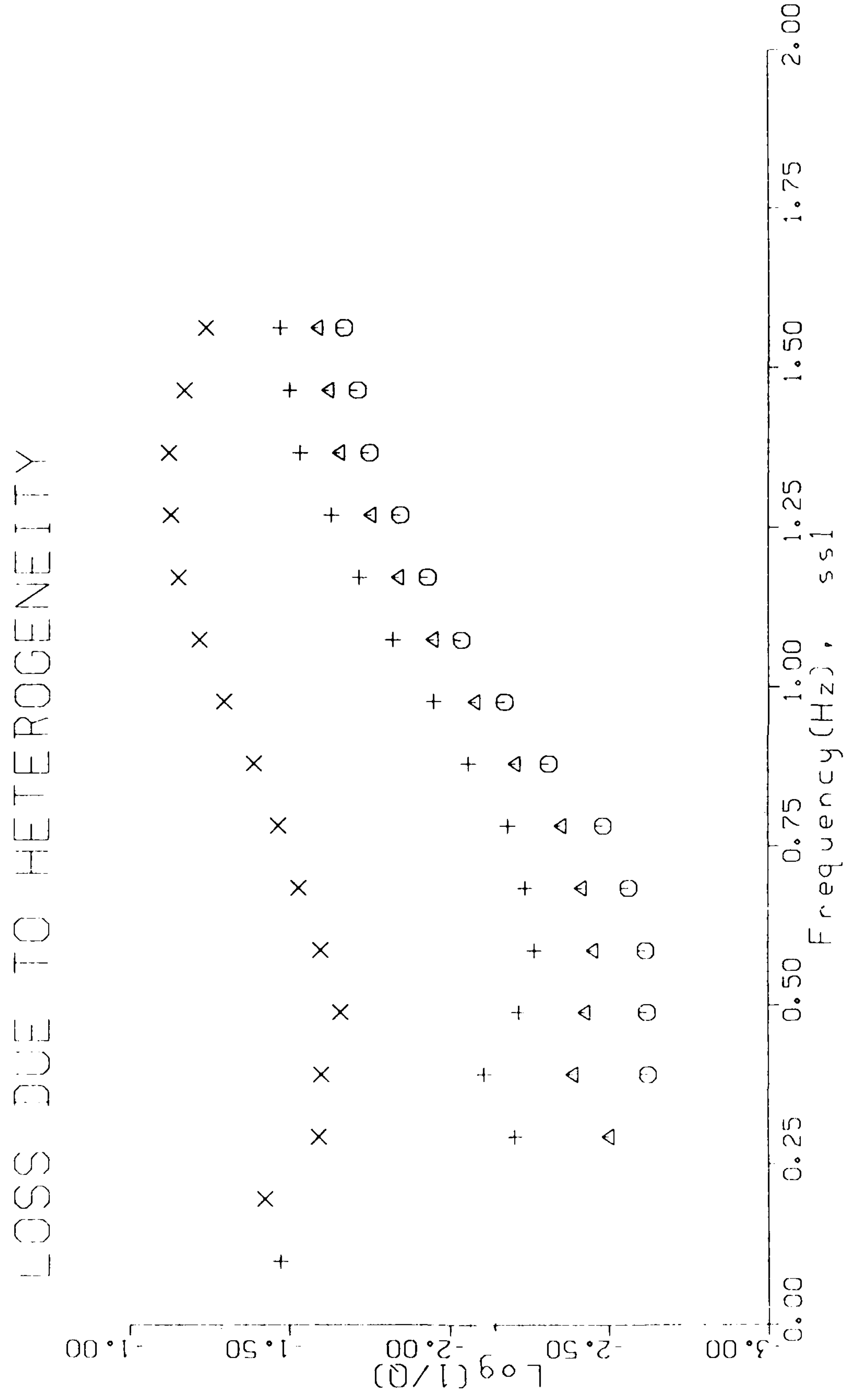
LOSS DUE TO HETEROGENEITY
Frequency(Hz), ss1
0.00
0.25
0.50
0.75
1.00
1.25
1.50
1.75
2.00
Log(1/Q)
-1.00
-1.50
-2.00
-2.50
-3.00

Fig.8C

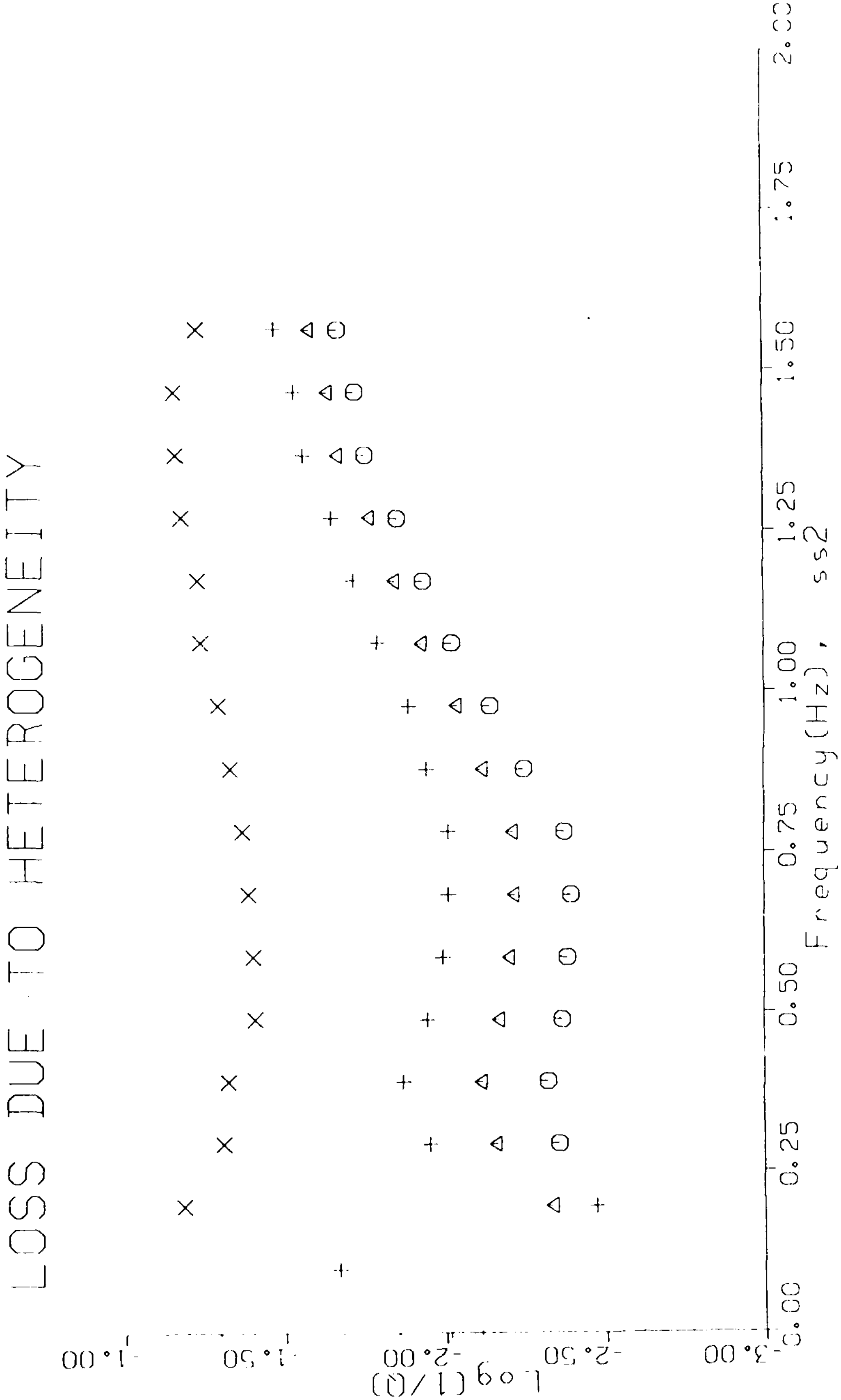
LOSS DUE TO HETEROGENEITY
Frequency (Hz), ss2
0.00
0.25
0.50
0.75
1.00
1.25
1.50
1.75
2.00
Log (1/Q)
-3.00
-2.50
-2.00
-1.50
-1.00

Fig.8D

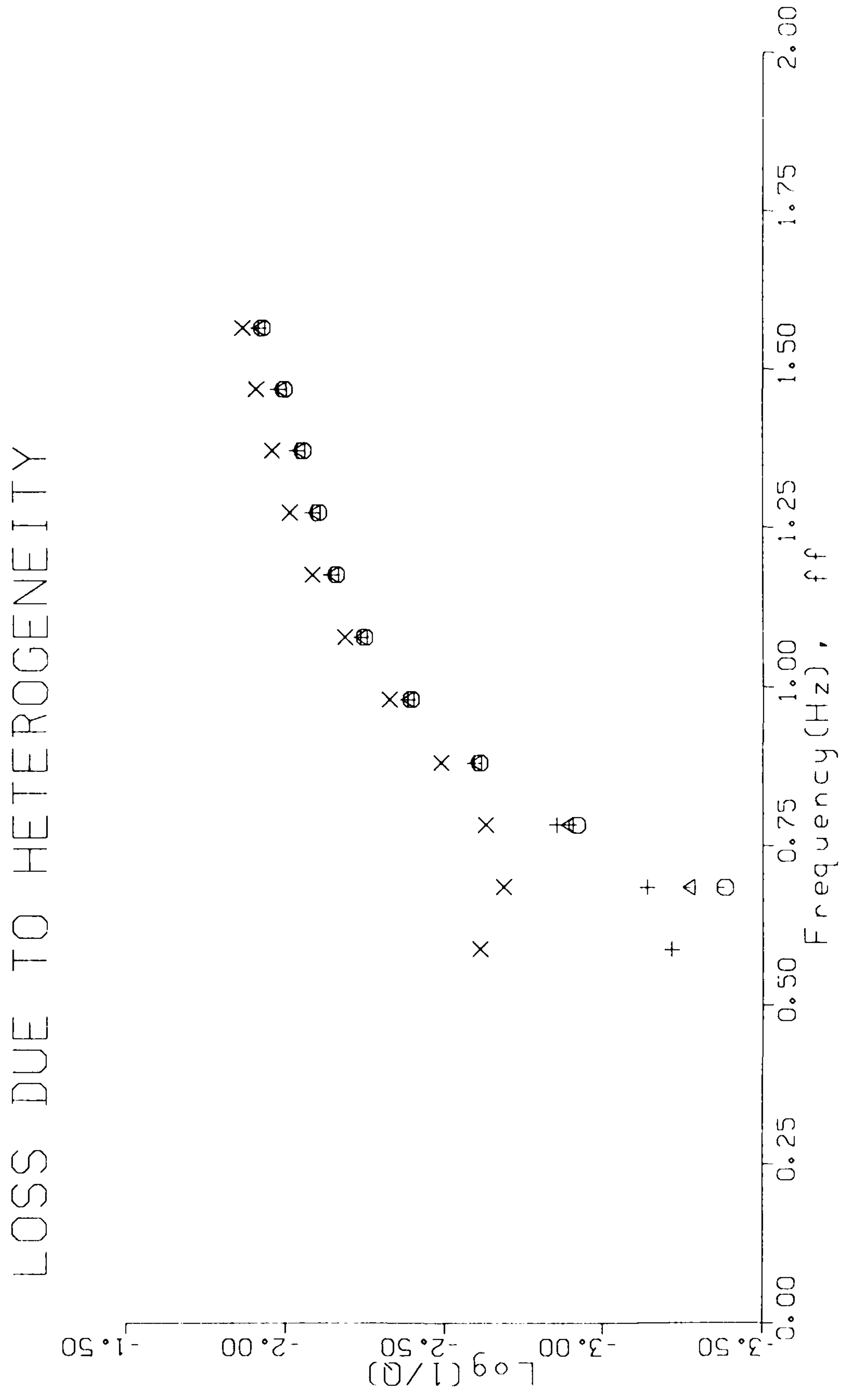
LOSS DUE TO HETEROGENEITY
Frequency(Hz), ff
0.00
0.25
0.50
0.75
1.00
1.25
1.50
1.75
2.00
Log(1/Q)
-3.50
-3.00
-2.50
-2.00
-1.50

Fig.8E

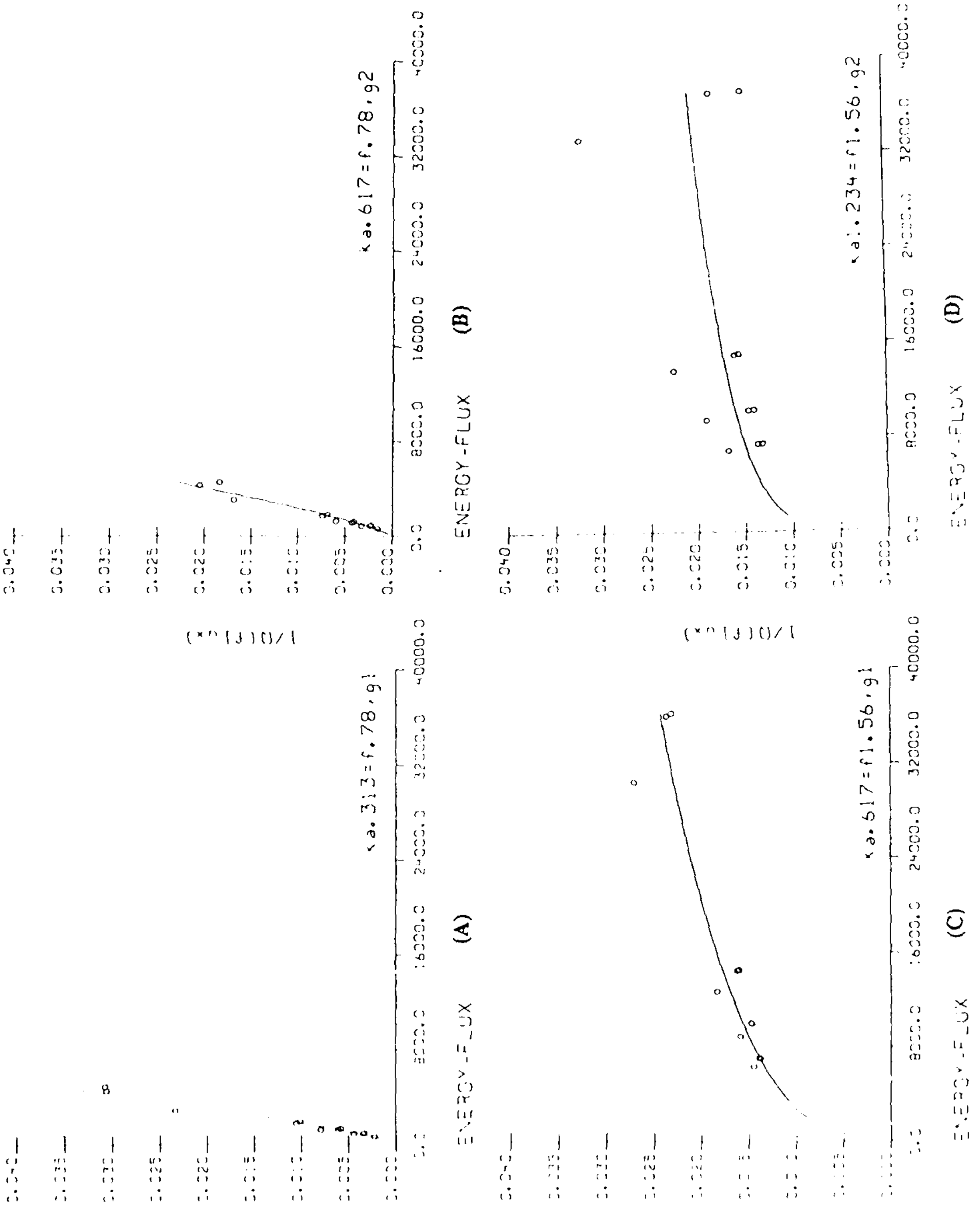
ka.313=f.78,g1
ka.617=f.78,g2
ka.617=f1.56,g1
ka1.234=f1.56,g2
ENERGY-FLUX
1/Q(f,ux)
0.000
0.005
0.010
0.015
0.020
0.025
0.030
0.035
0.040
0.0
8000.0
16000.0
24000.0
32000.0
40000.0
(A)
(B)
(C)
(D)

Fig.9

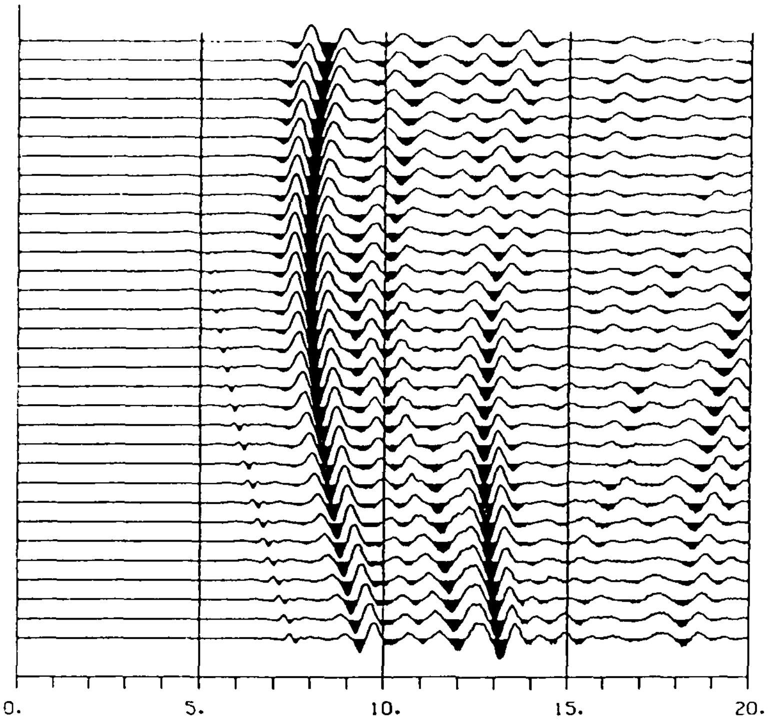

deepDILA,1km,g=1,5%,3.2

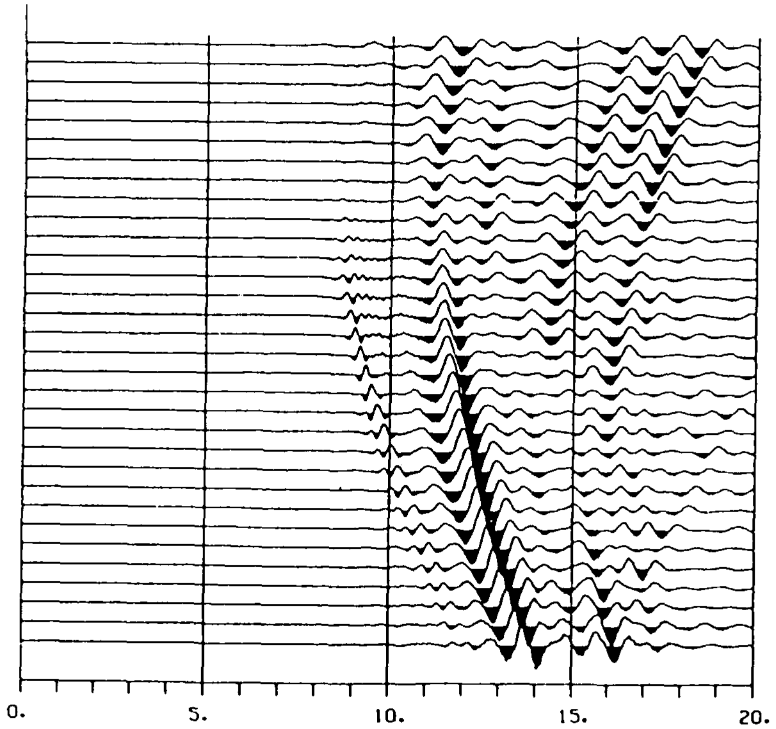

deepROTA,1km,g=1,5%,3.2

Fig.10A

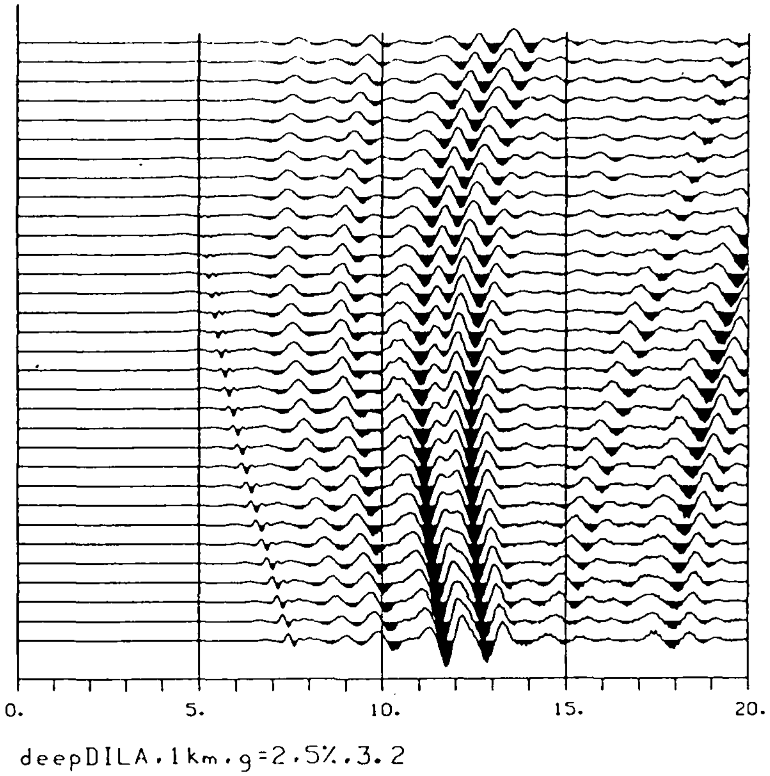

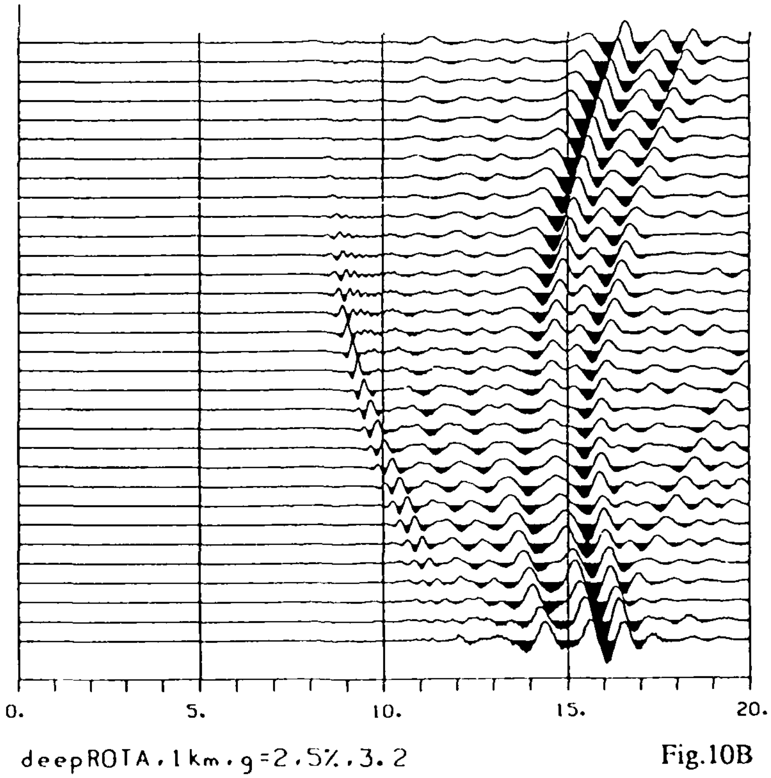

Fig.10B

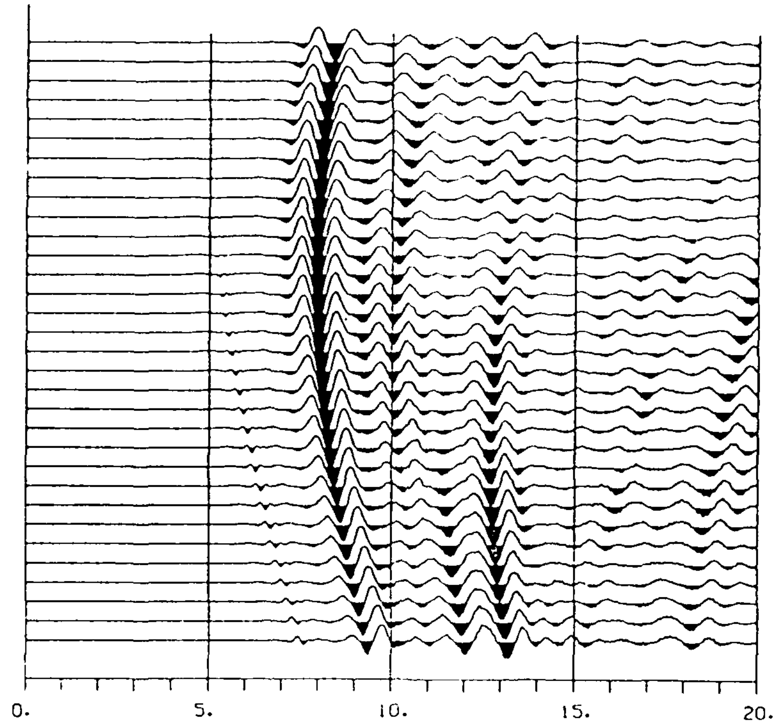

deepDILA.1km.g=1.7%.3.2

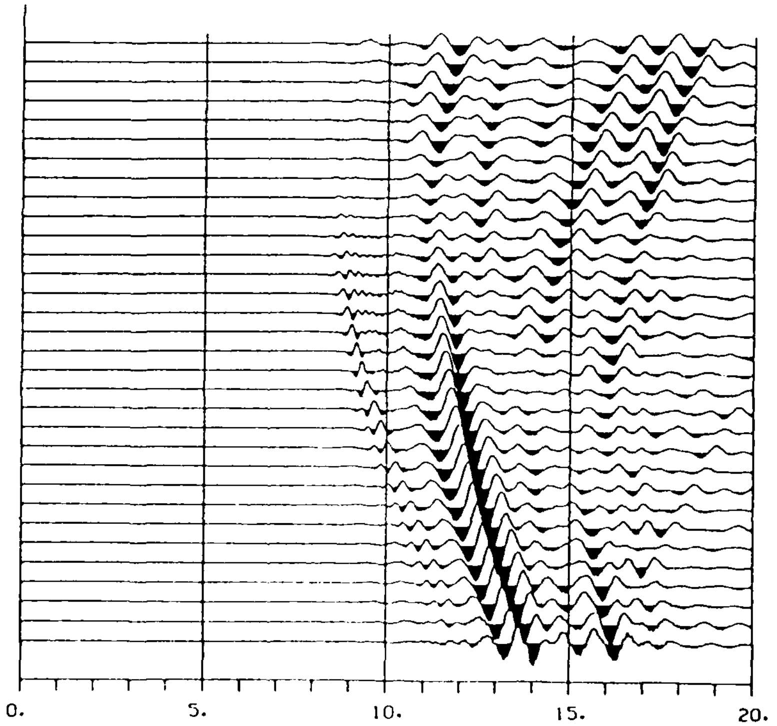

deepROTA.1km.g=1.7%.3.2

Fig.10C

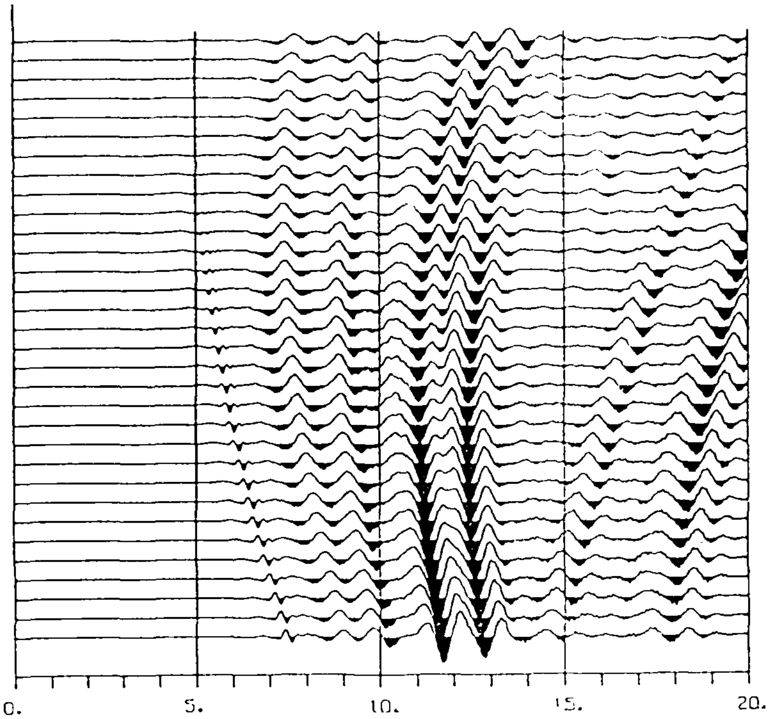

deepDILA,1km,g=2,7%,3.2

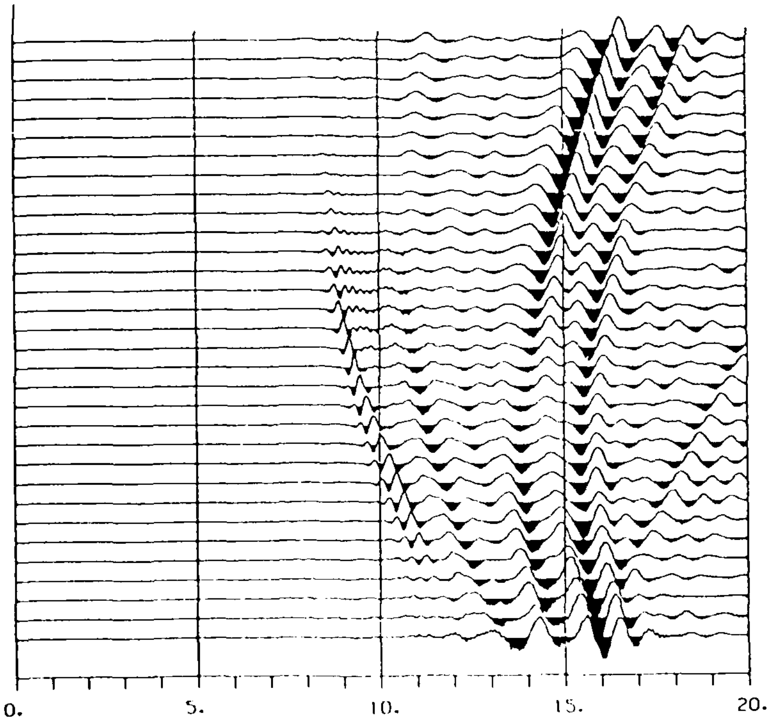

deepROTA,1km,g=2,7%,3.2

Fig.10D

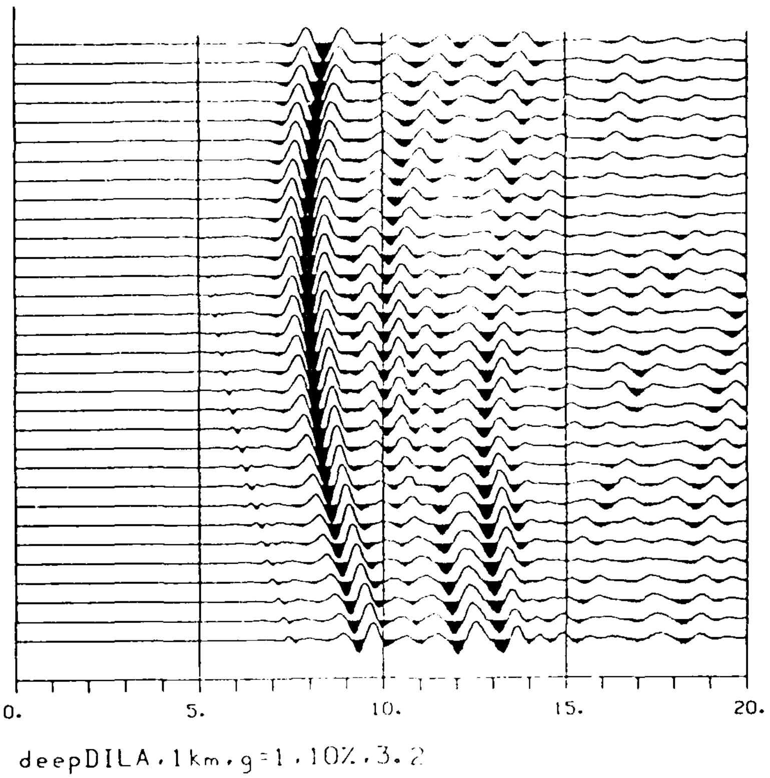
0.
5.
10.
15.
20.
deepDILA,1km,g=1,10%,3.2

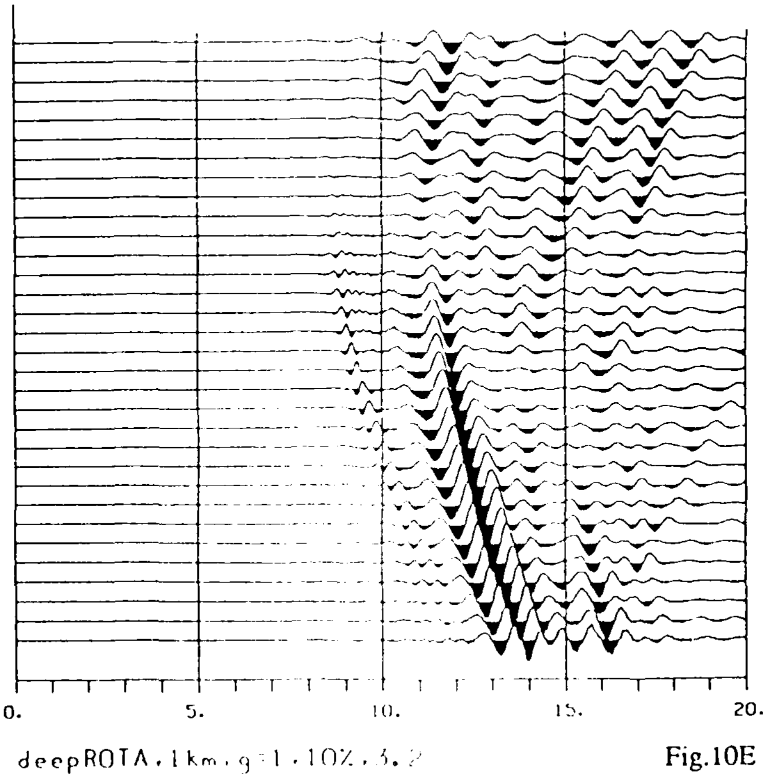
0.
5.
10.
15.
20.
deepROTA,1km,g=1,10%,3.2

Fig.10E

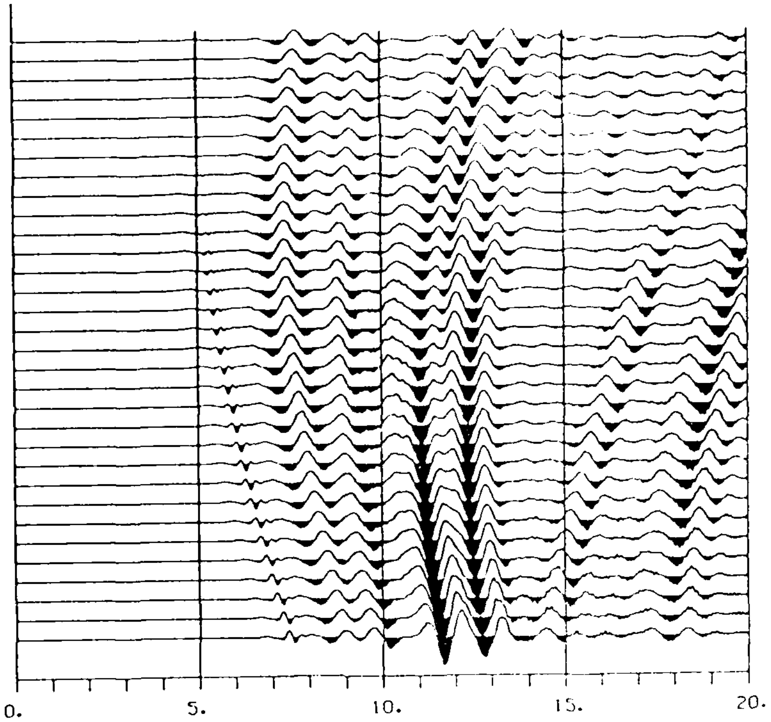

deepDILA,1km,g=2,10%,3.2

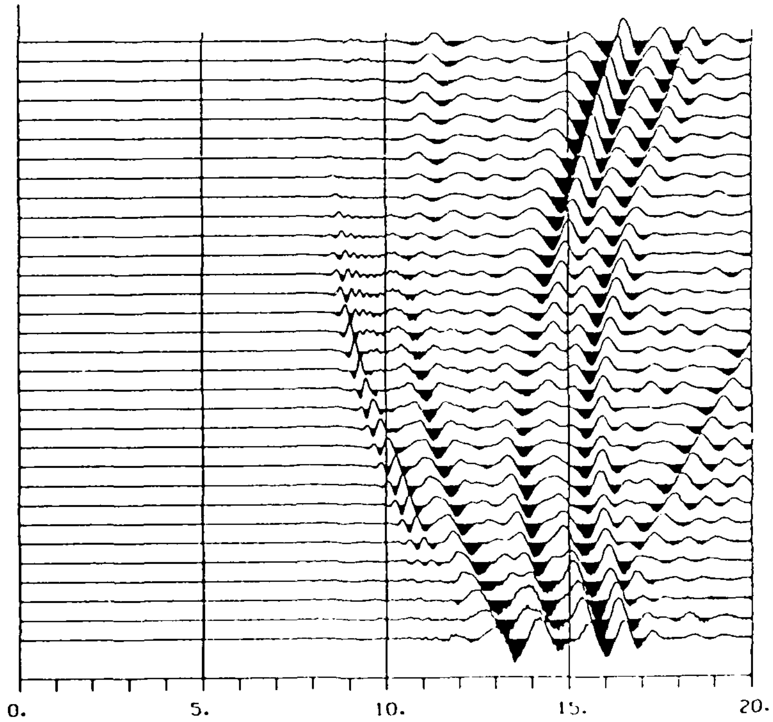

deepROTA,1km,g=2,10%,3.2

Fig.10F

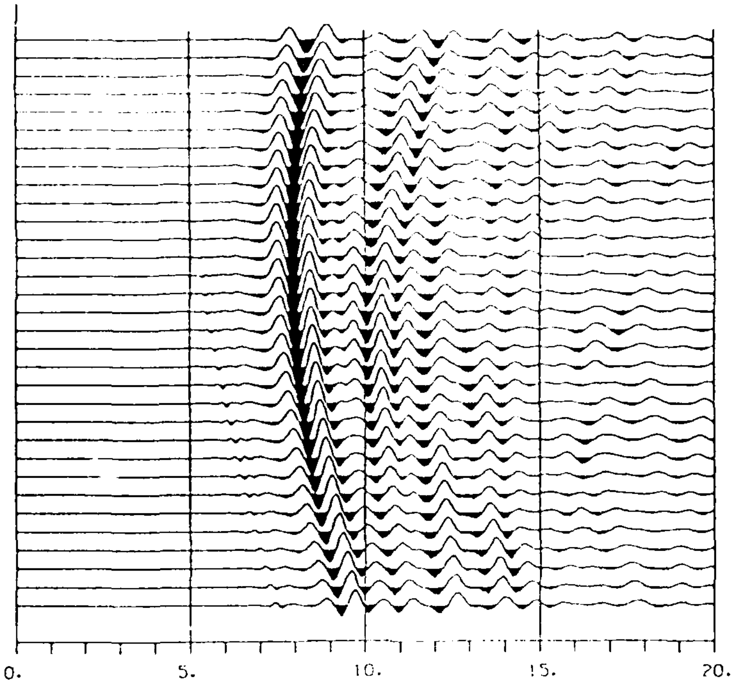

deepDILA,1km,g=1,20%,3.2

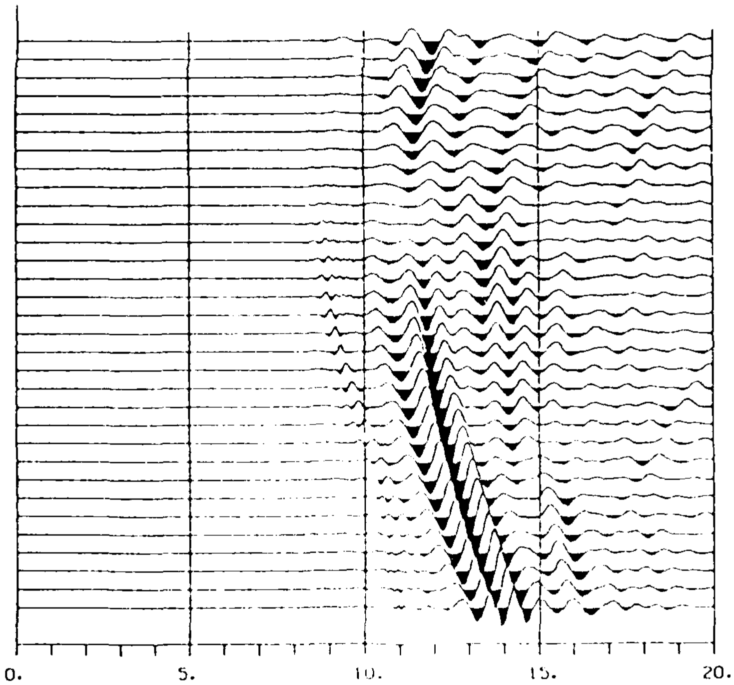

deepROTA,1km,g=1,20%,3.2

Fig.10G

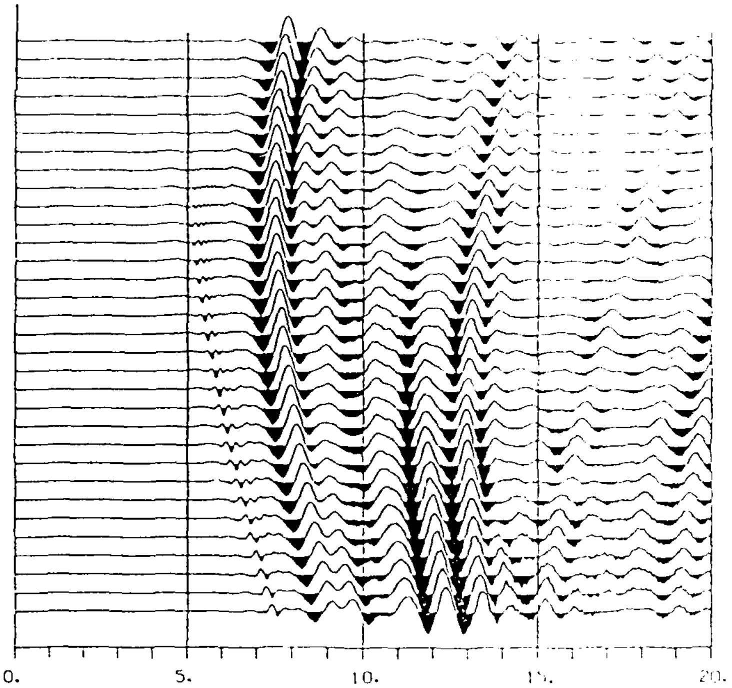

deep(R=>P),1km,(a2,20%,3.2)

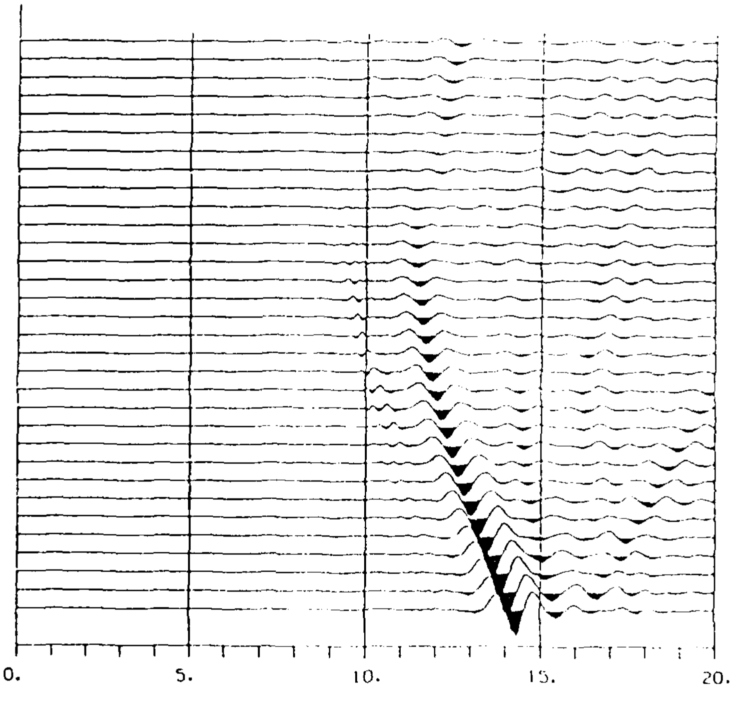

deep(R=>S),1km,(a2,20%,3.2)

Fig.10H

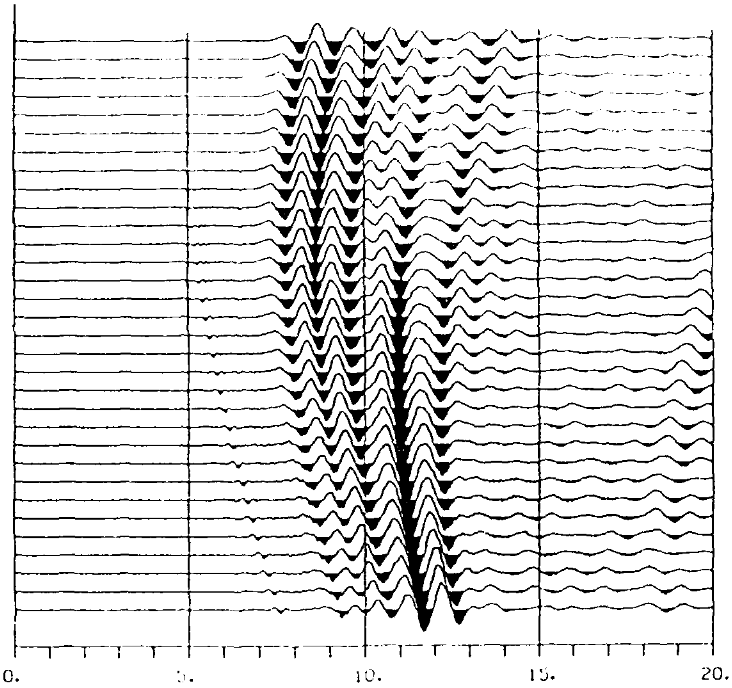

deep(R=>P),1km,(ss,3.2)

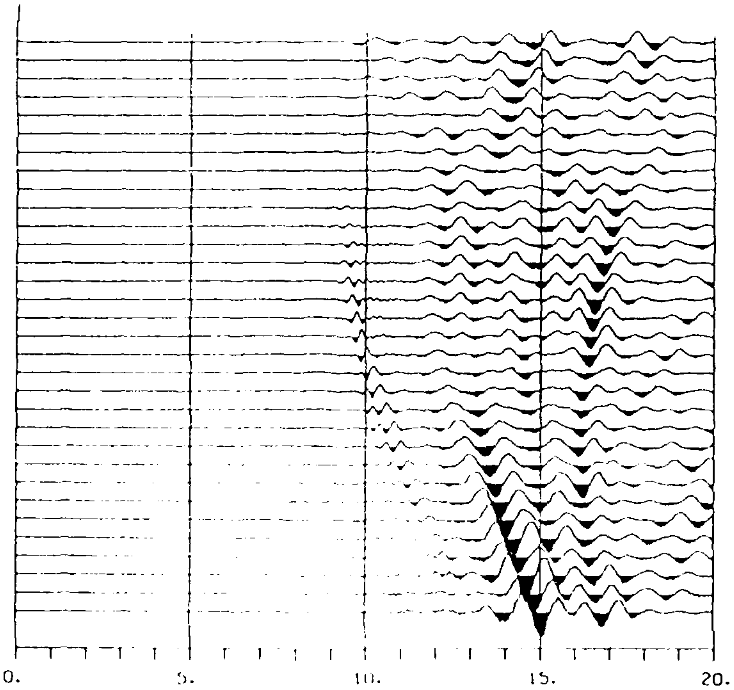

deep(R=>S),1km,(ss,3.2)

Fig.101

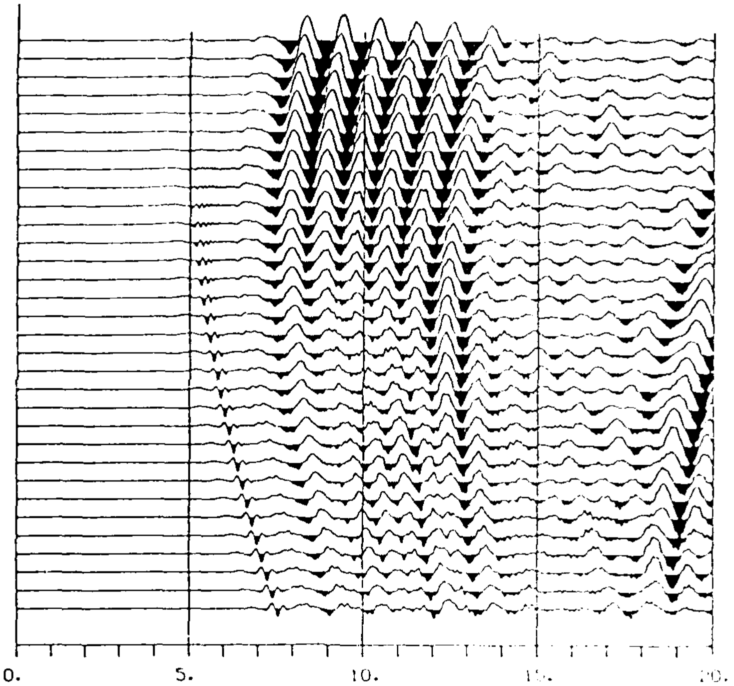

deep(R=>P),1km,(folded,3.2)

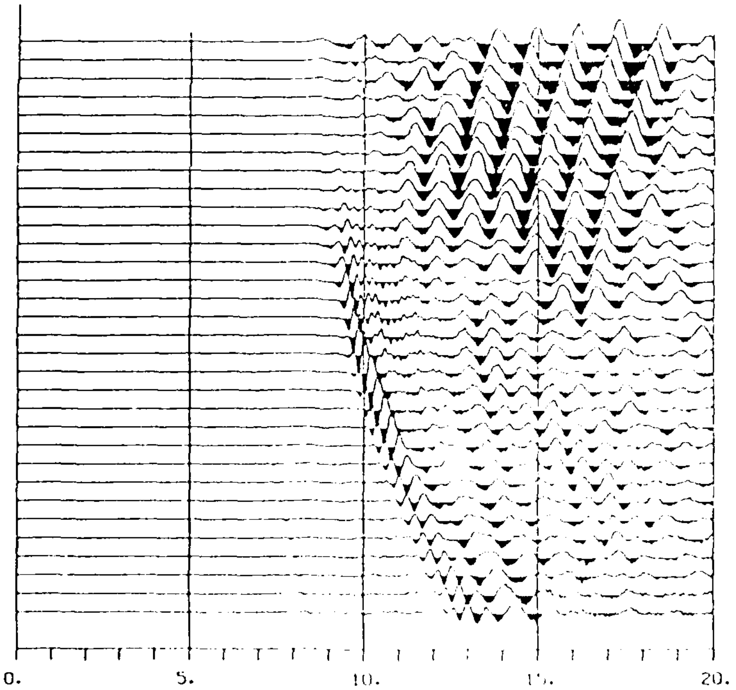

deep(R=>S),1km,(folded,3.2)

Fig.10J

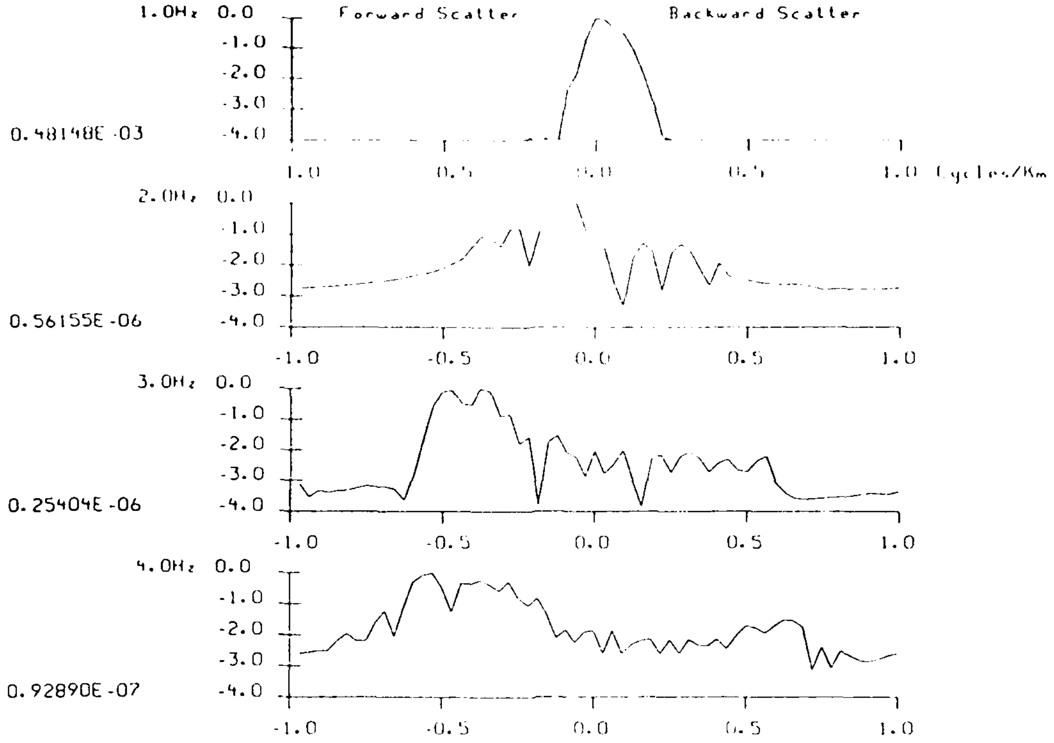

deep(R=>P)..5km,(a1km,5%,3.2km)

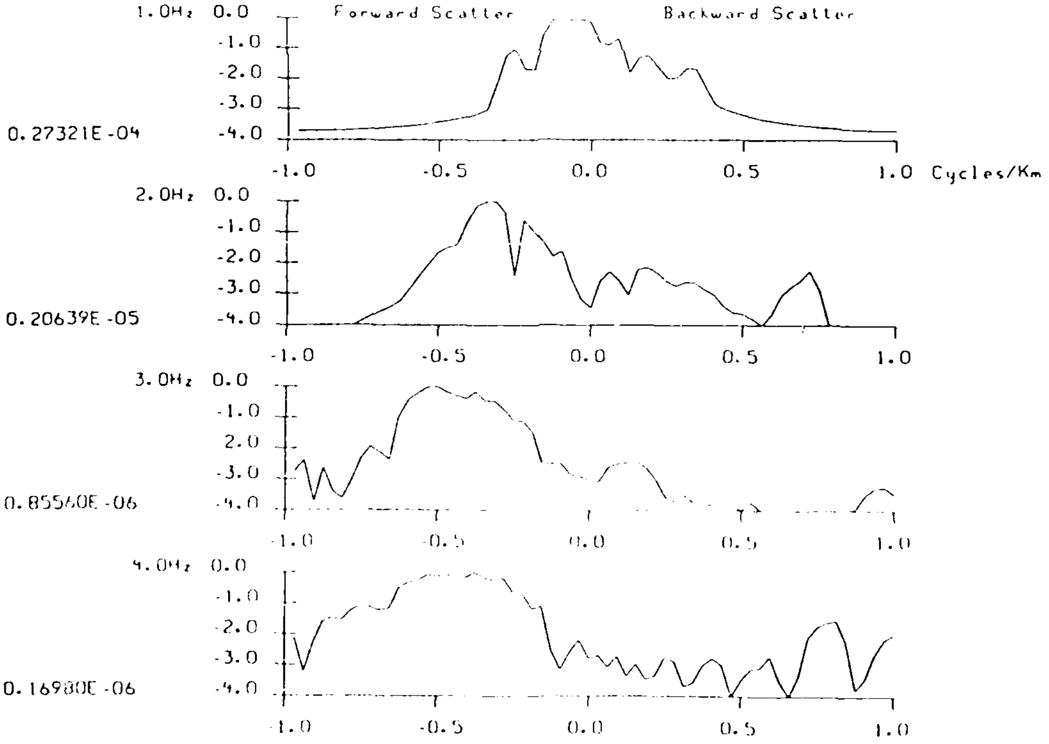

deep(R=>S)..5km,(a1km,5%,3.2km)

NORMALIZED Log(POWER) WAVENUMBER SPECTRA Fig.11A

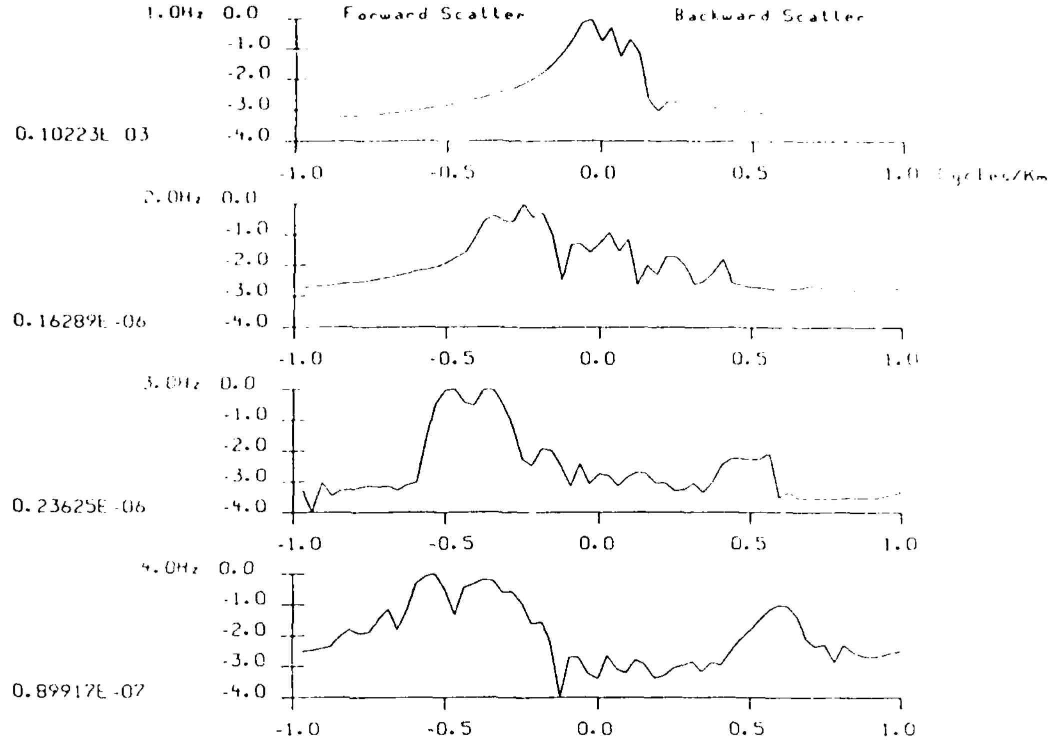

deep(R=>P),.5km,(a2km,5%,3.2km)

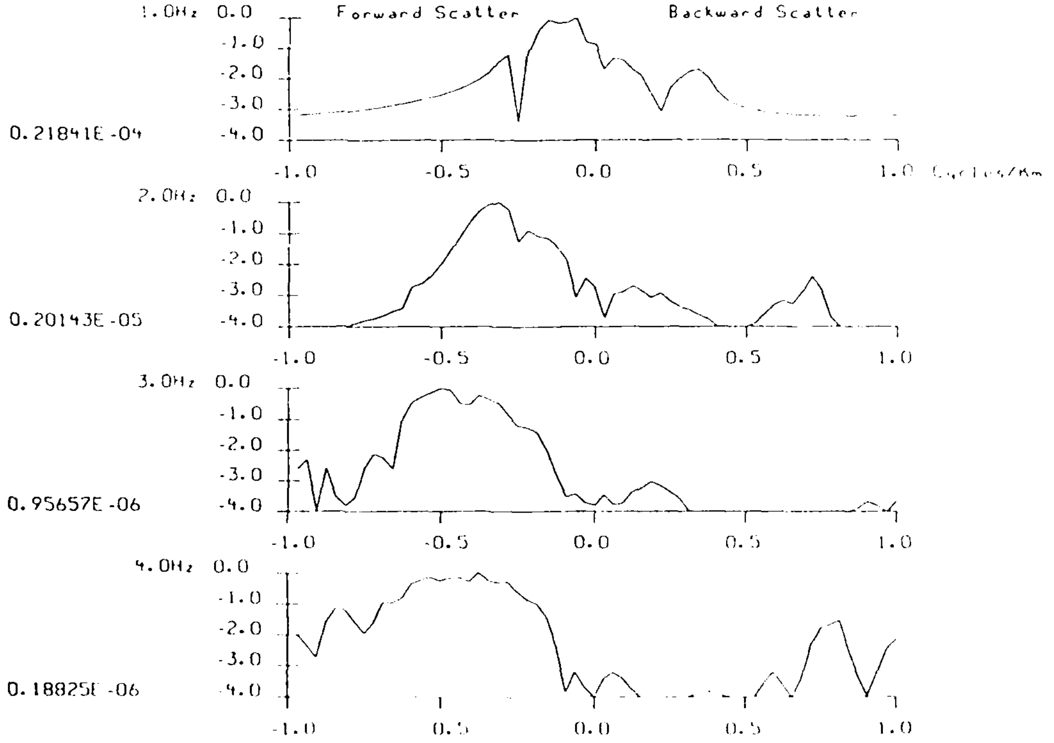

deep(R=>S),.5km,(a2km,5%,3.2km)

NORMALIZED Log(POWER) WAVENUMBER SPECTRA Fig.11B

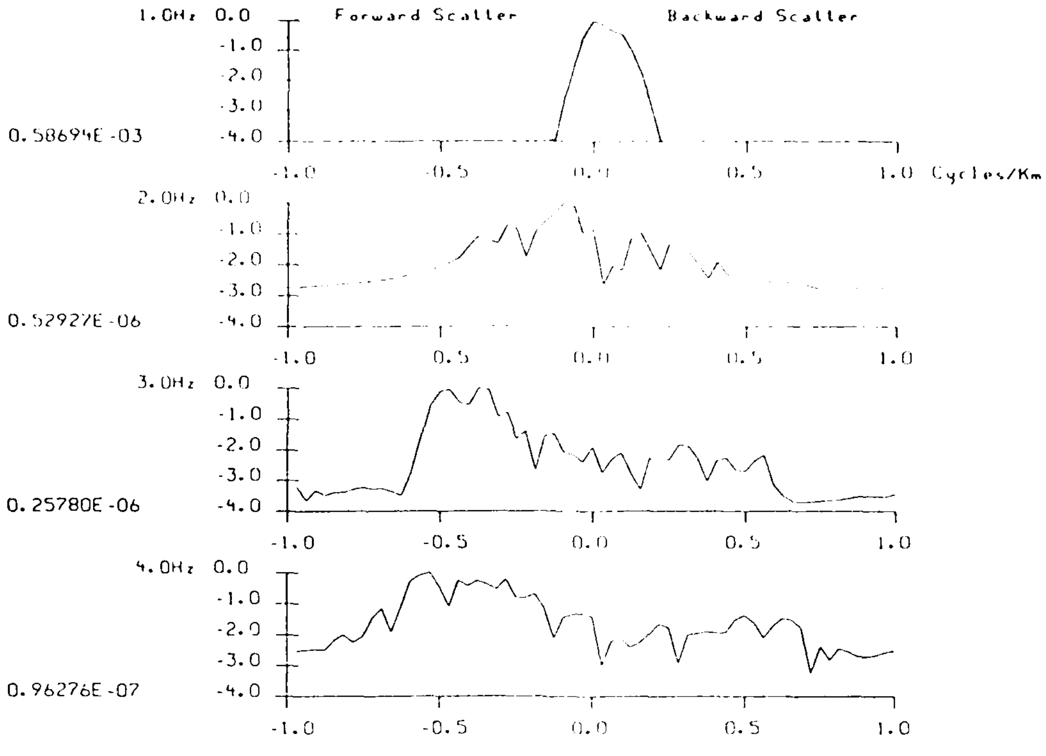

deep(R=>P)..5km,(a1km,7%,3.2km)

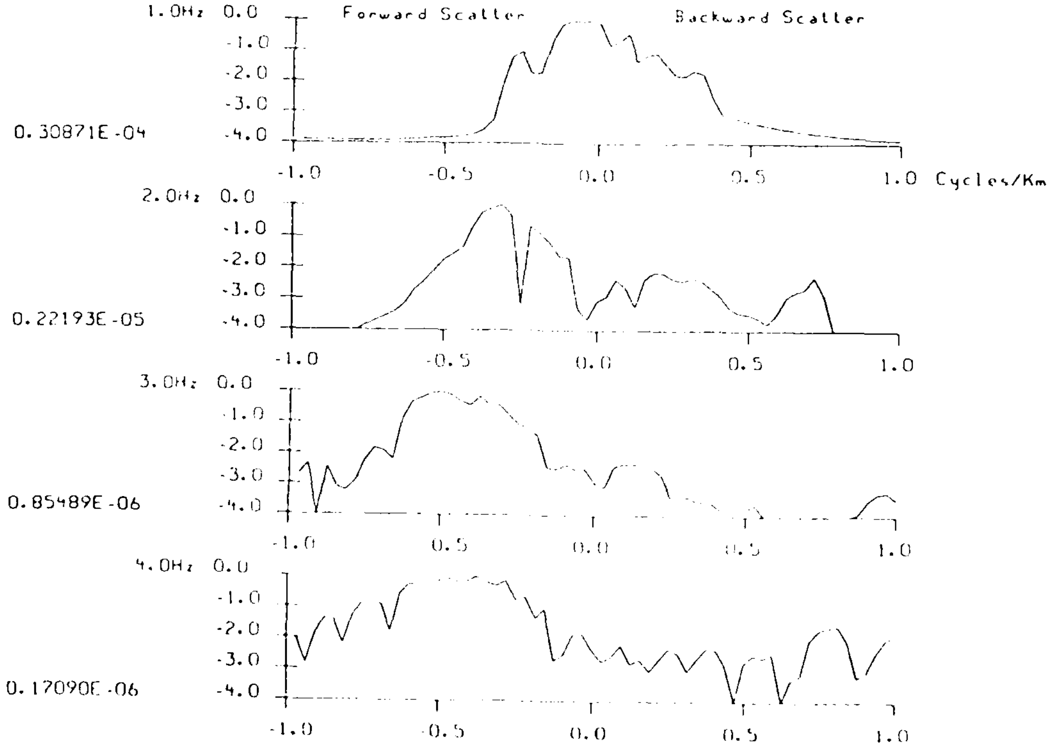

deep(R=>S)..5km,(a1km,7%,3.2km)

NORMALIZED Log(POWER) WAVENUMBER SPECTRA Fig.11C

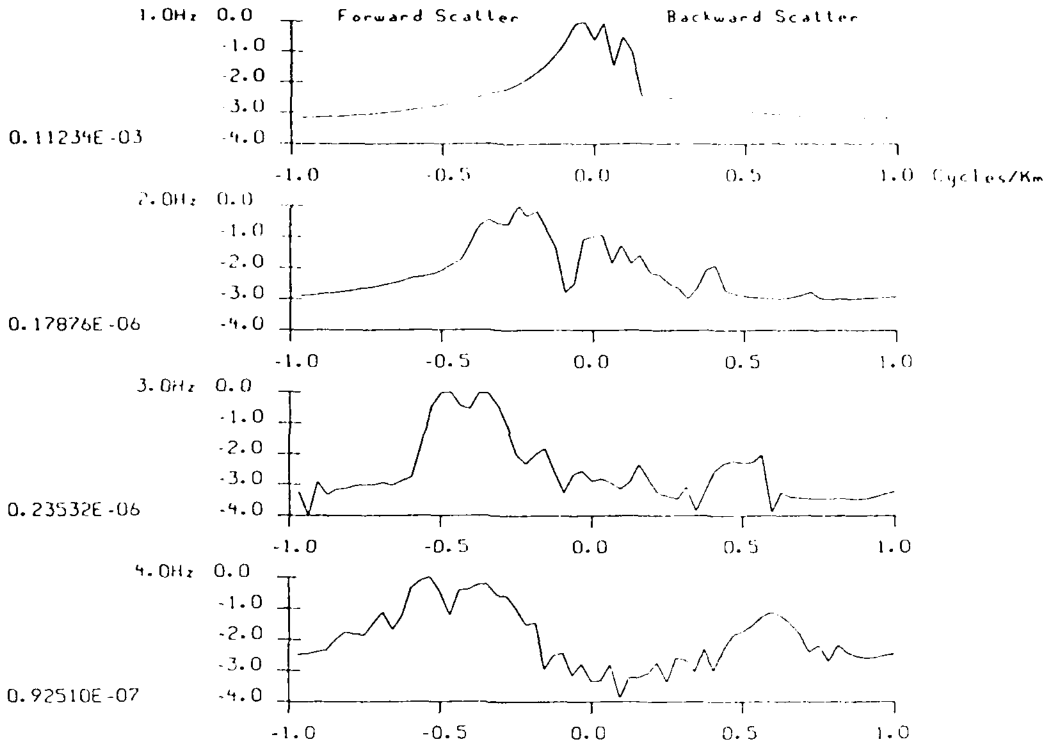

deep(R=>P),.5km,(a2km,7%,3.2km)

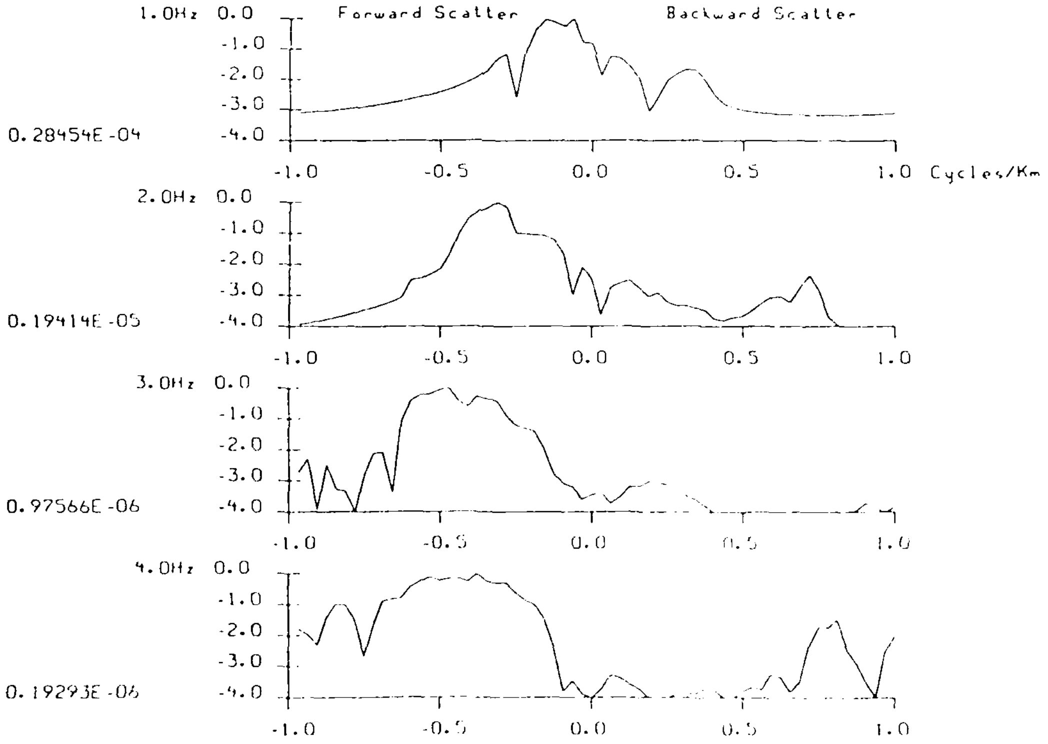

deep(R=>S),.5km,(a2km,7%,3.2km)

NORMALIZED Log(POWER) WAVENUMBER SPECTRA Fig.1 ')

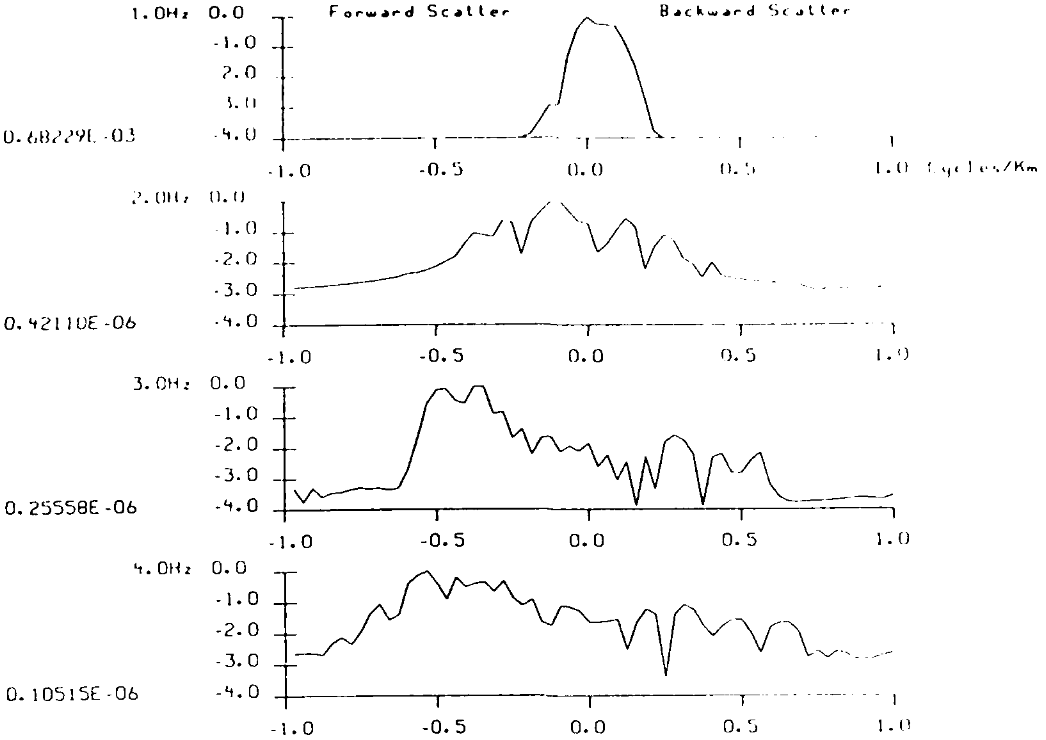

deep(R=>P)..5km,(a1km,10%,3.2km)

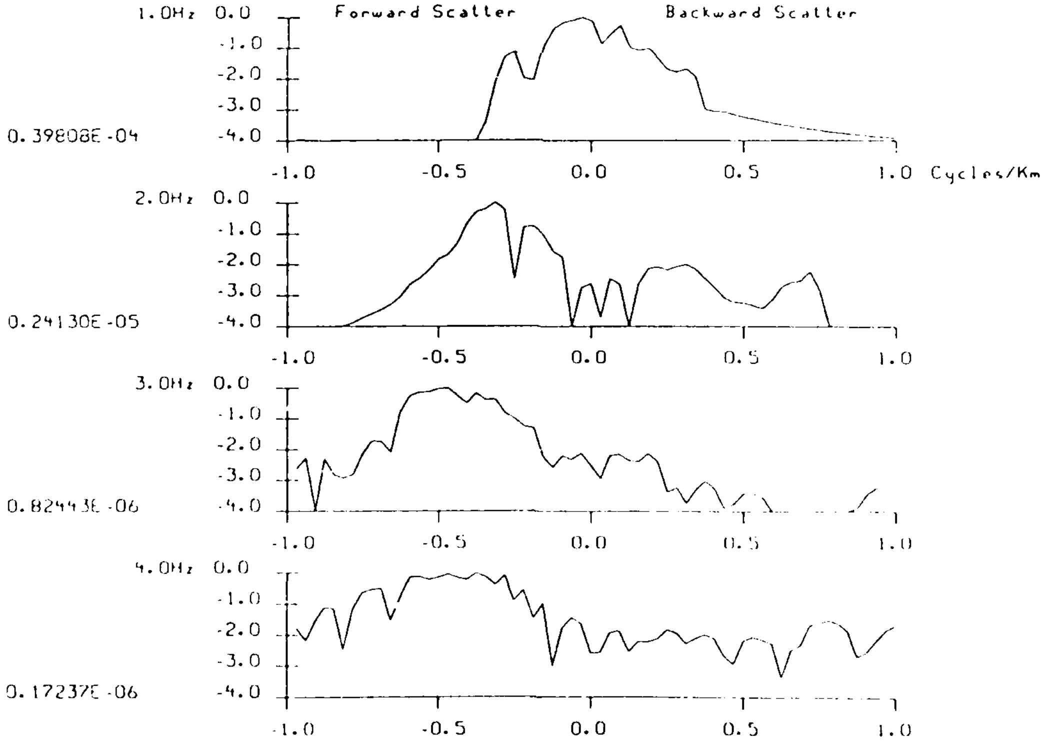

deep(R=>S)..5km,(a1km,10%,3.2km)

NORMALIZED Log(POWER) WAVENUMBER SPECTRA Fig.11E

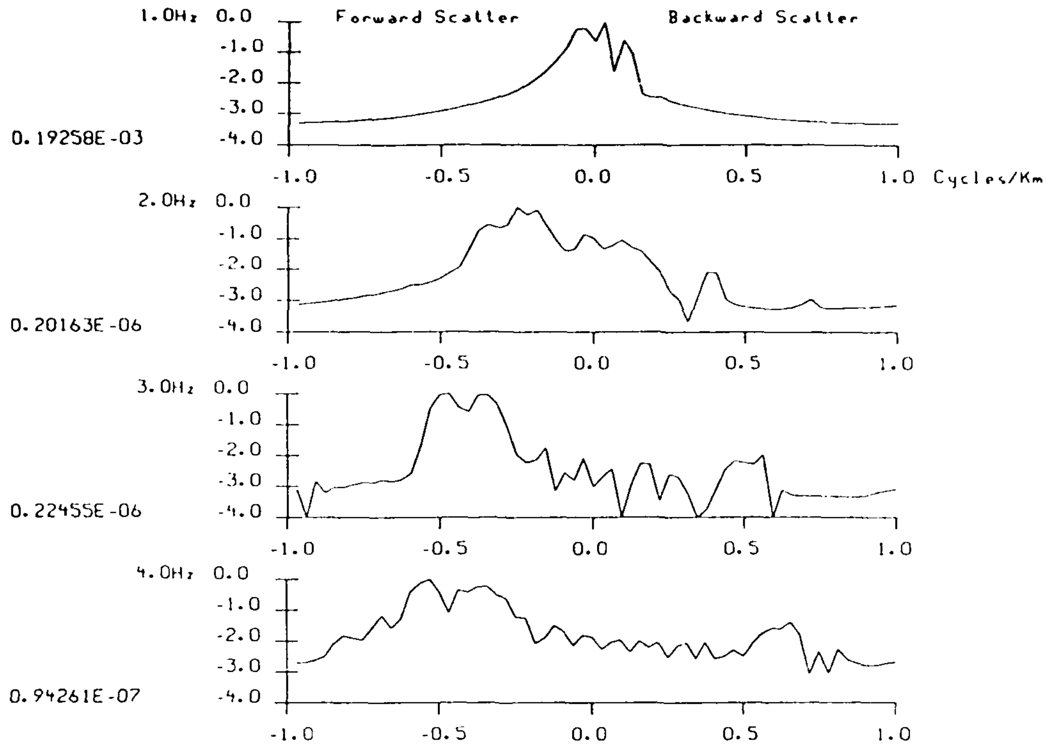

deep(R=>P),.5km,(a2km,10%,3.2km)

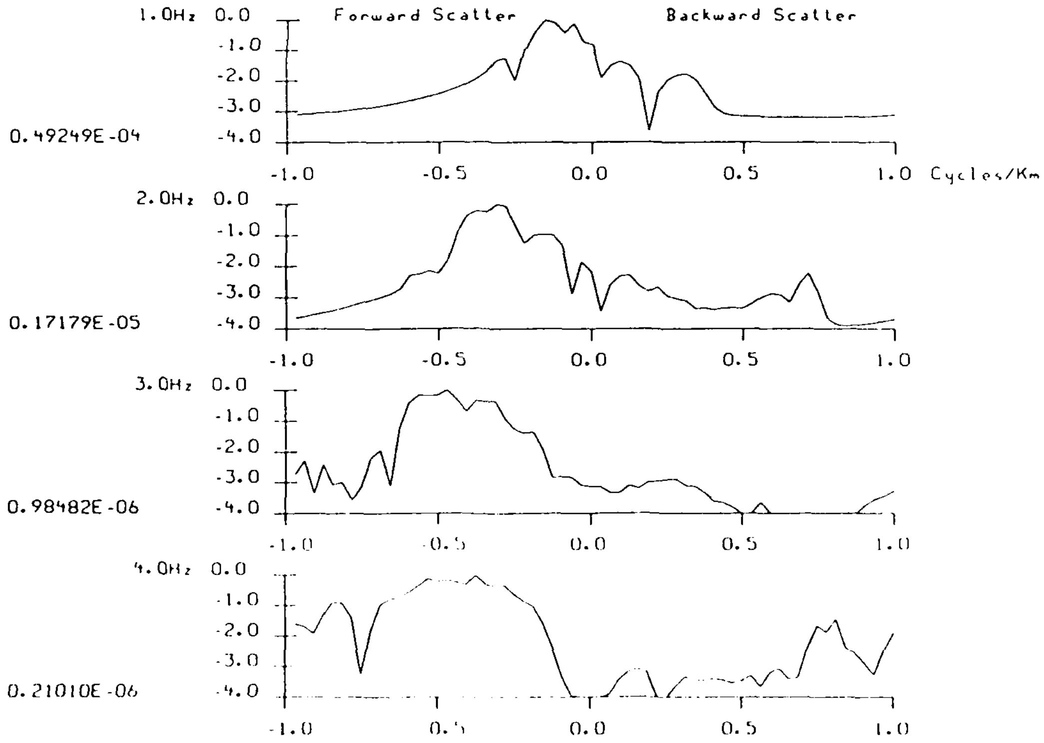

deep(R=>S),.5km,(a2km,10%,3.2km)

NORMALIZED Log(POWER) WAVENUMBER SPECTRA Fig.11F

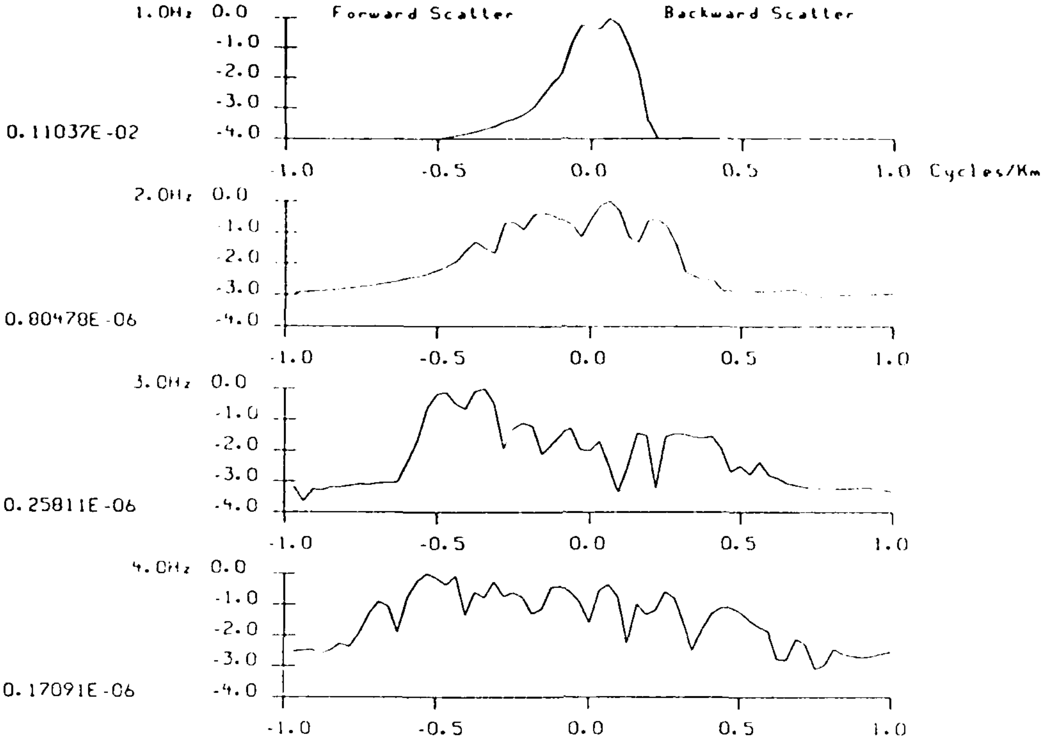

deep(R=>P),.5km,(a1km,20%,3.2km)

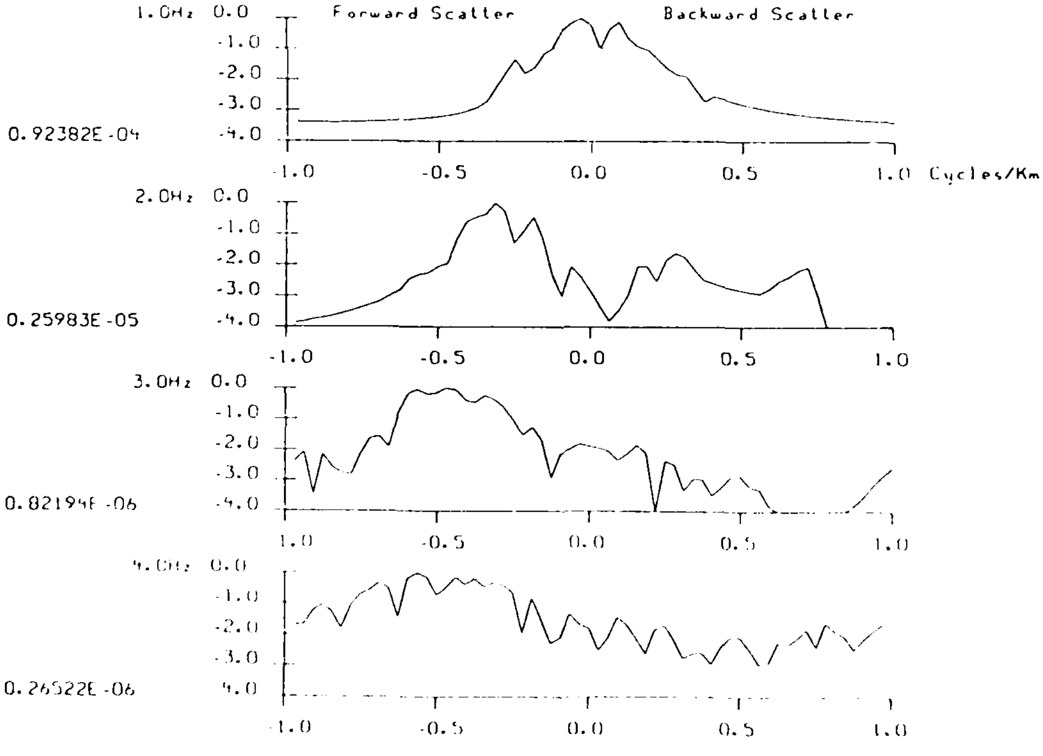

deep(R=>S),.5km,(a1km,20%,3.2km)

NORMALIZED Log(POWER) WAVENUMBER SPECTRA Fig.11G

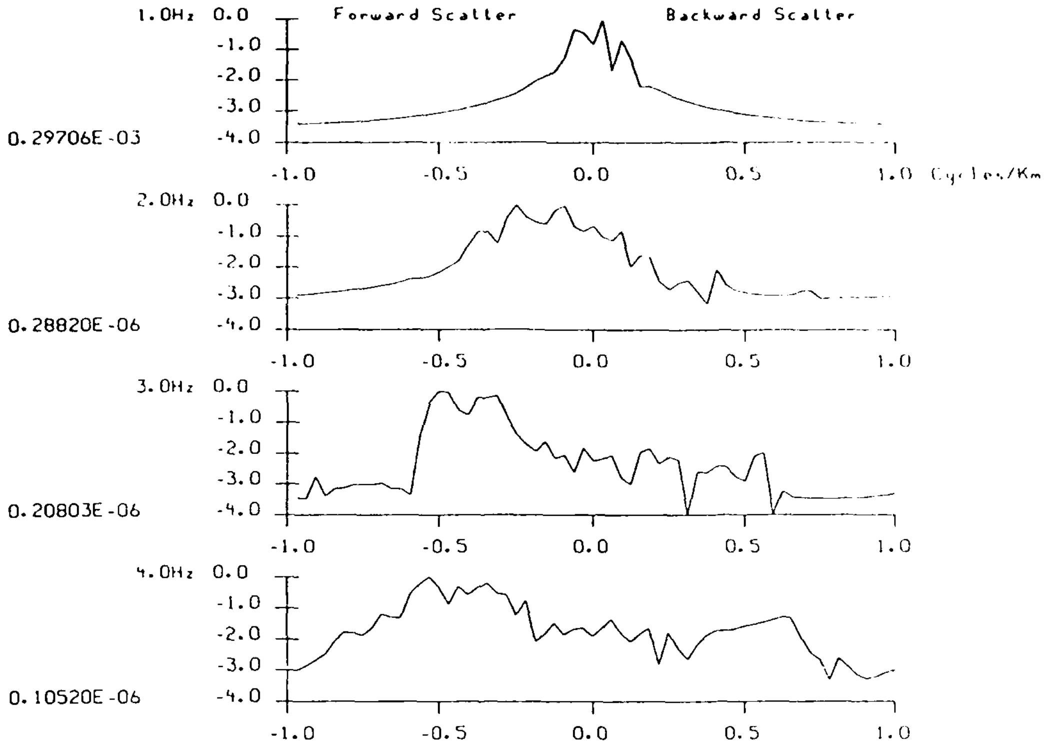

deep(R=>P)..5km,(a2km,20%,3.2km)

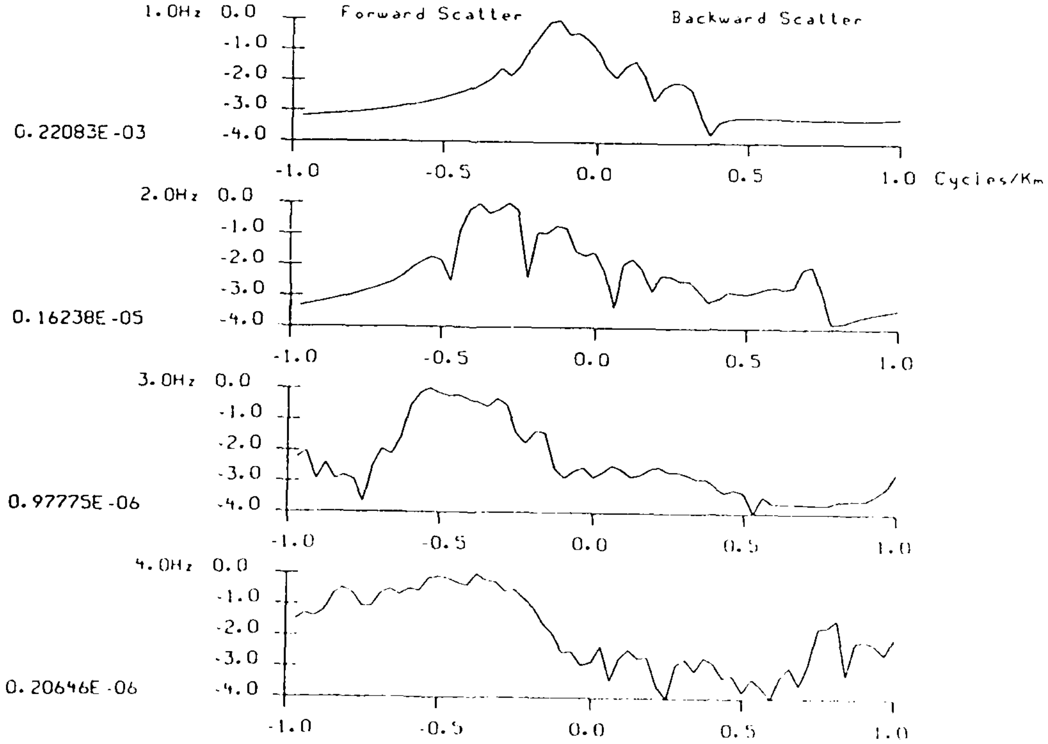

deep(R=>S)..5km,(a2km,20%,3.2km)

NORMALIZED Log(POWER) WAVENUMBER SPECTRA Fig.11H

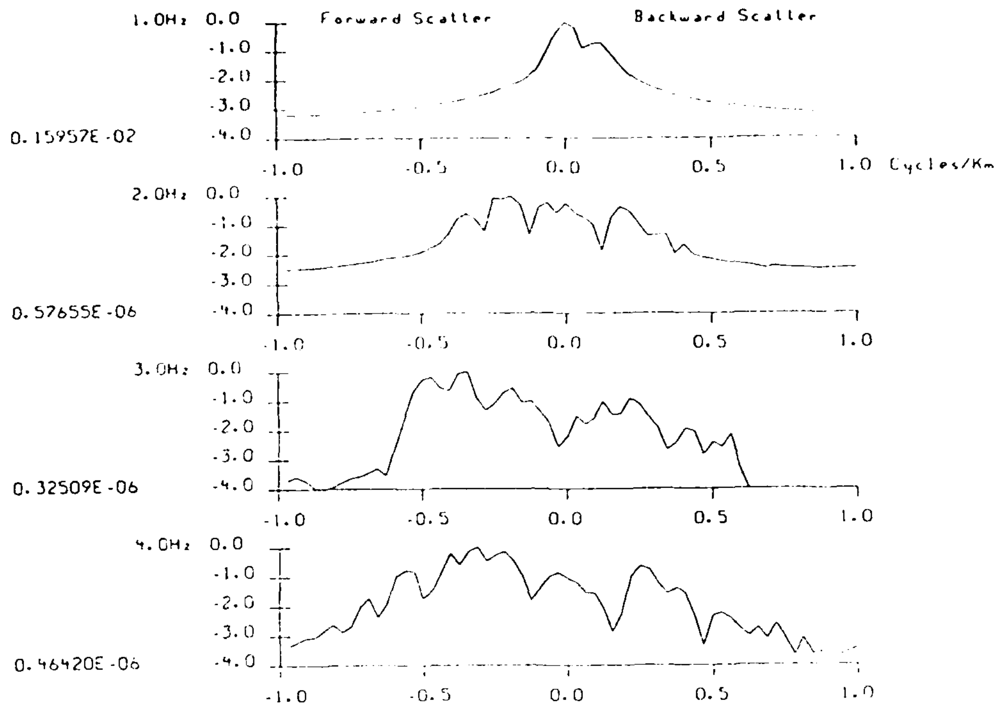

deep(R=>P)..5km,(ss,3.2km)

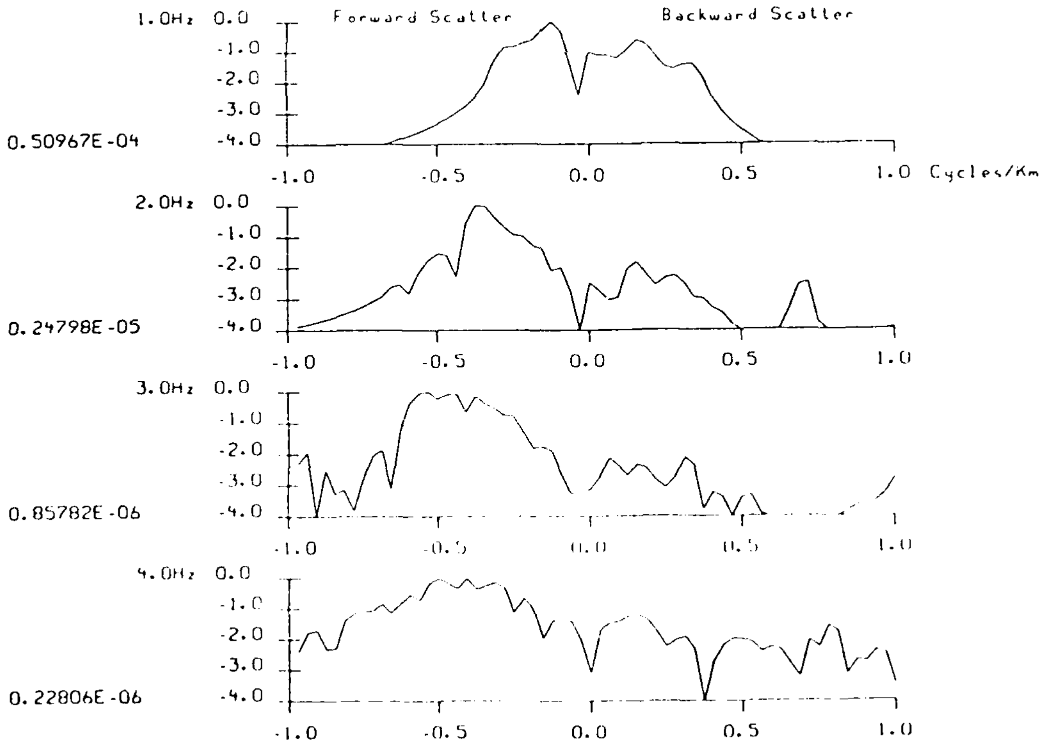

deep(R=>S)..5km,(,ss,3.2km)

NORMALIZED Log(POWER) WAVENUMBER SPECTRA Fig.111

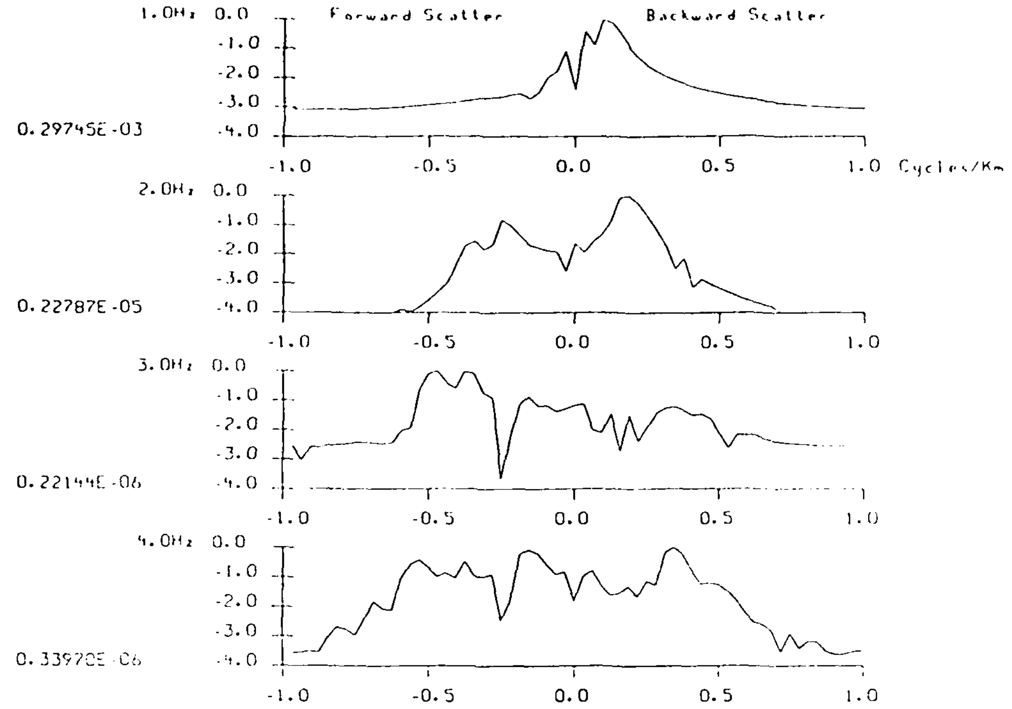

deep(R=>P)..5km,(,folded,3.2km)

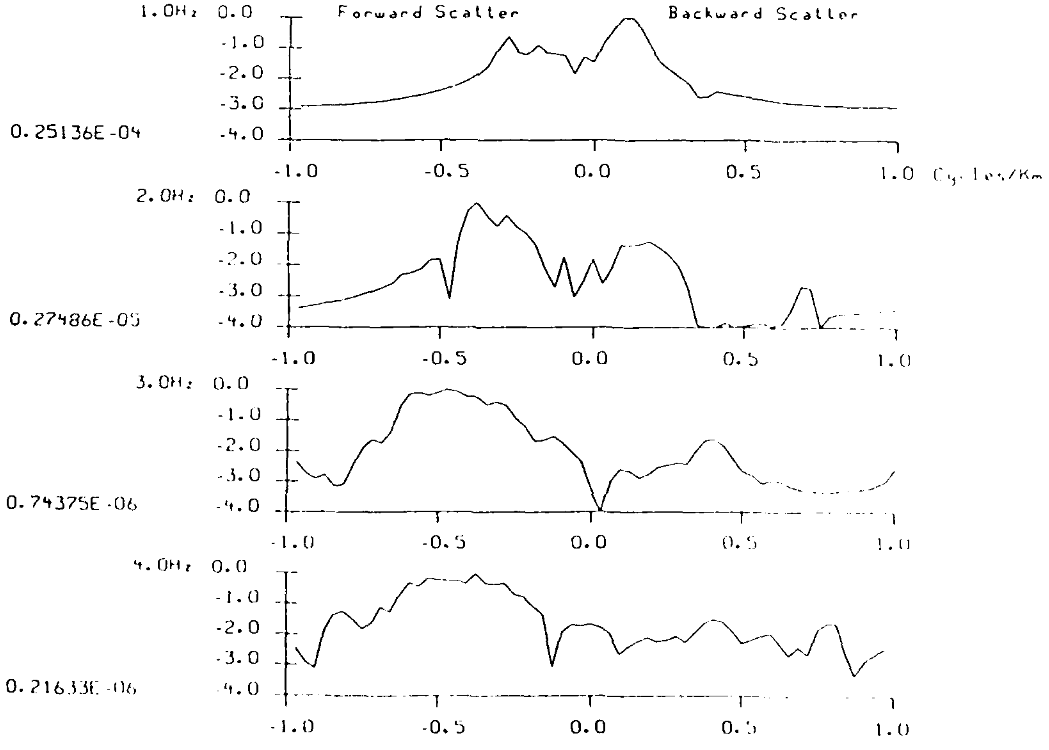

deep(R=>S)..5km,(,folded,3.2km)

NORMALIZED Log(POWER) WAVENUMBER SPECTRA Fig.11J

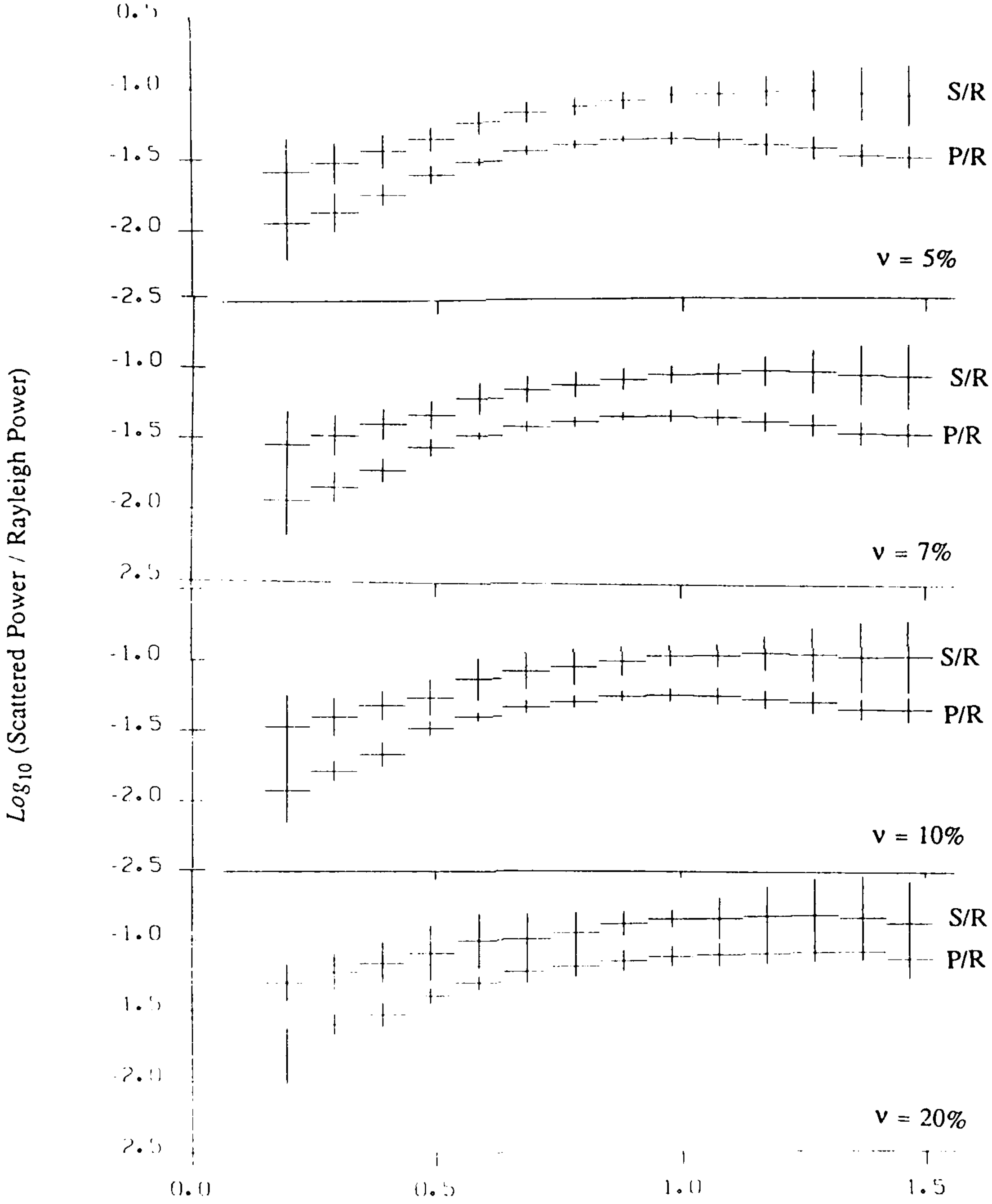

Power Spectral Ratios
Gaussian Autocorrelation Models (a=1km) Fig.12A

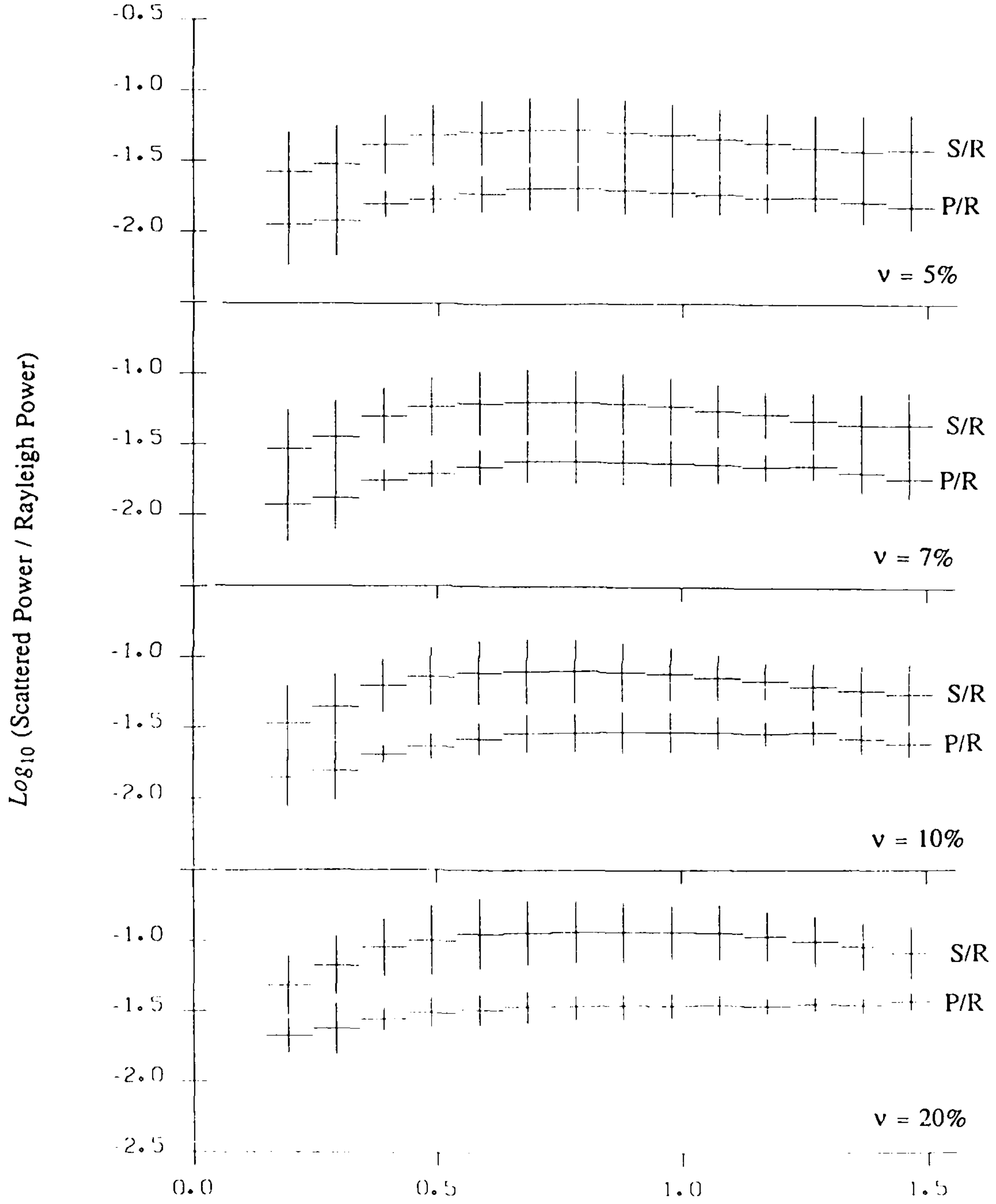

Fig.12B

Power Spectral Ratios
Gaussian Autocorrelation Models (a=2km)

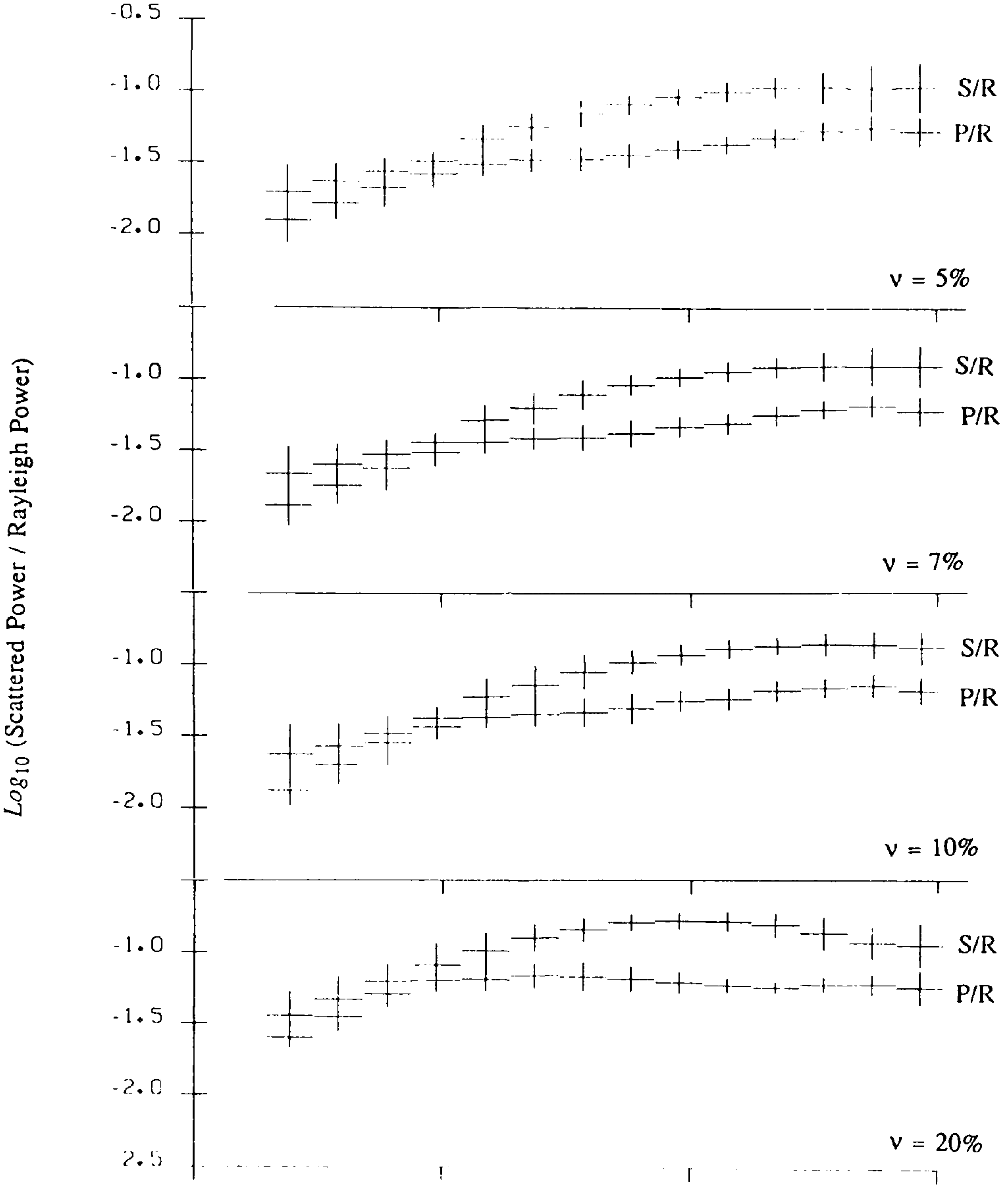

Fig.12C

Power Spectral Ratios
Self-Similar Models (a=1km)

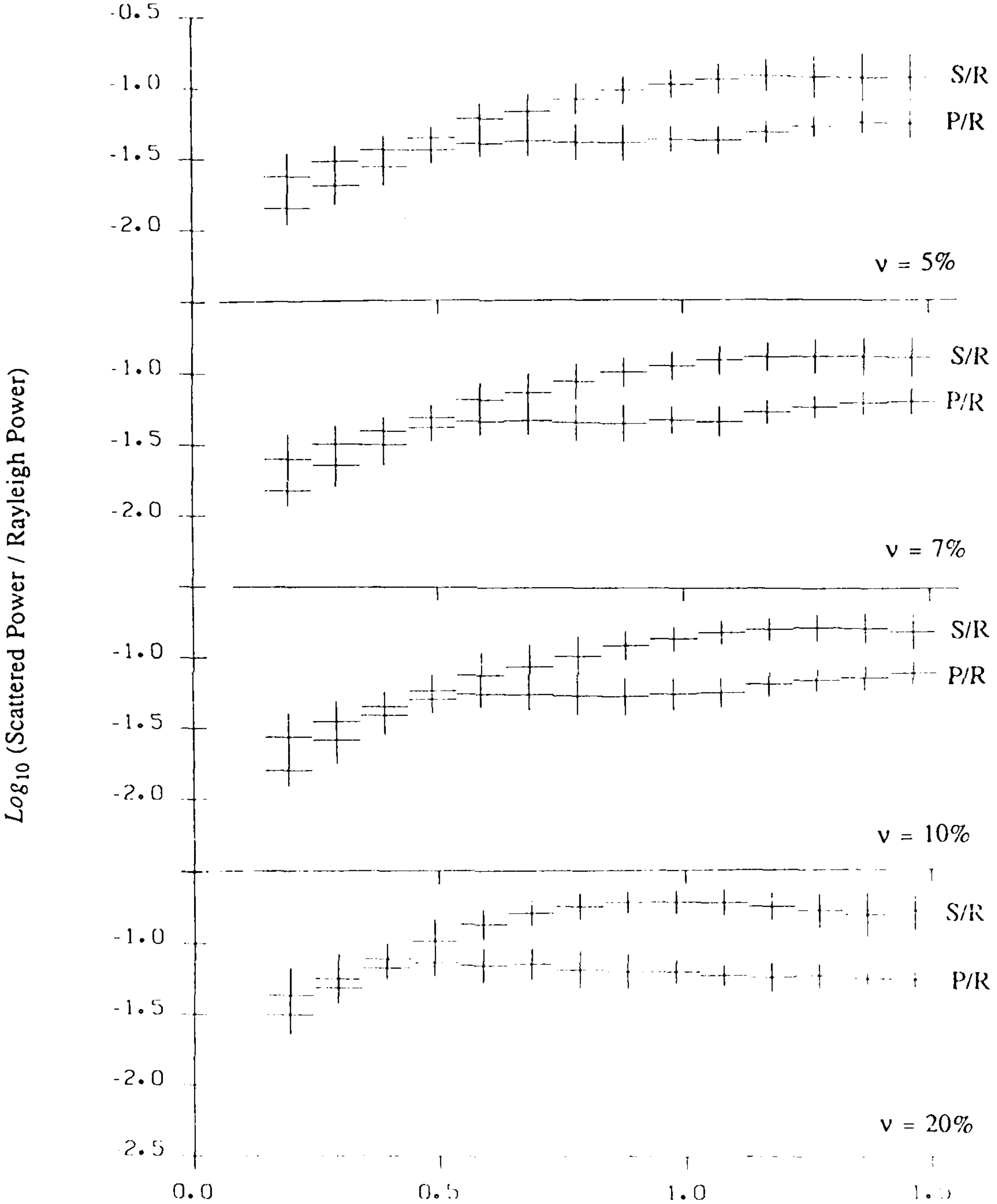

Power Spectral Ratios
Self-Similar Models (a=2km)

Fig.12D

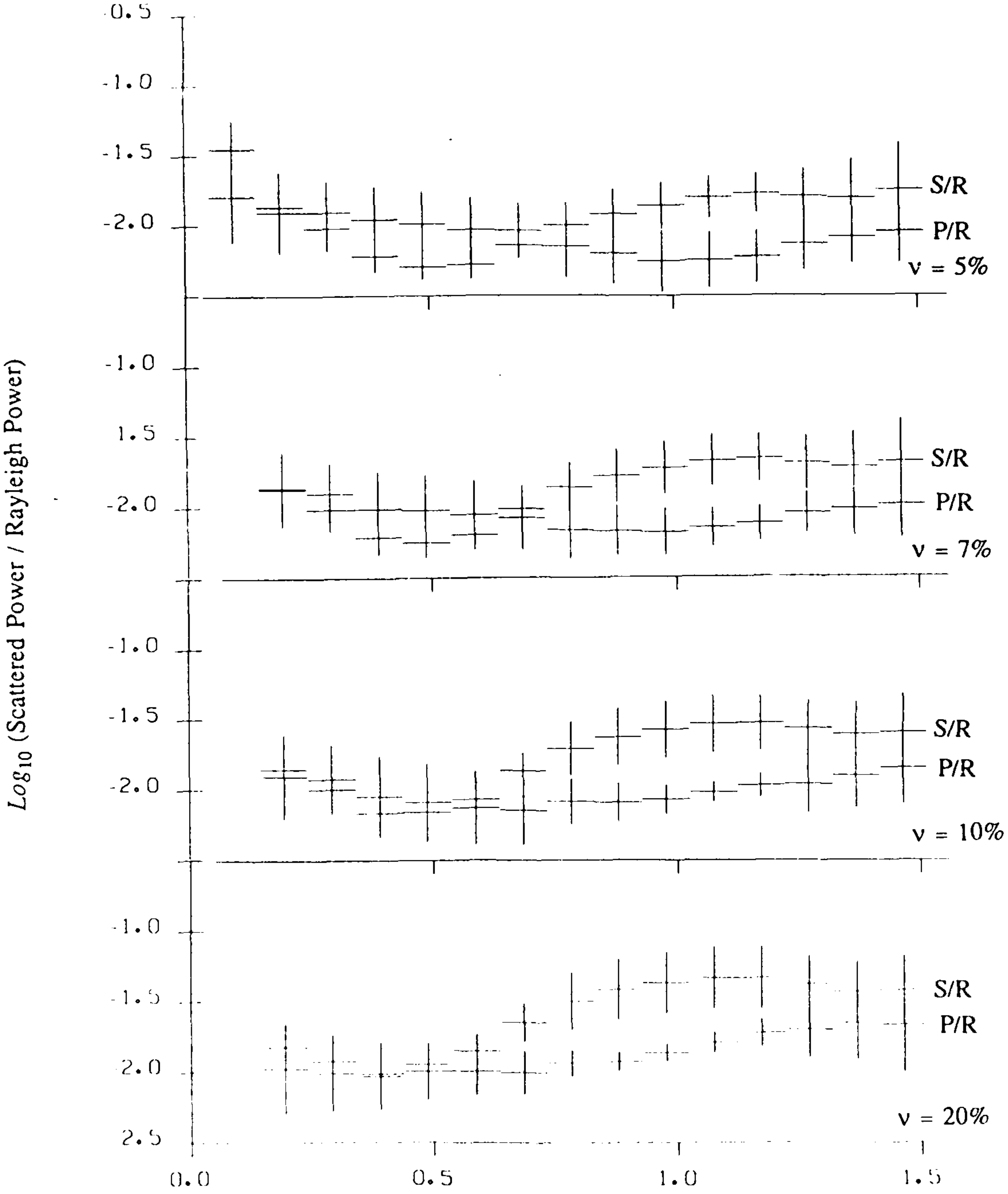

Power Spectral Ratios
Folded Models

Fig.12E

Professor Keiiti Aki
Center for Earth Sciences
University of Southern California
University Park
Los Angeles, CA 90089-0741

Professor Charles B. Archambeau
Cooperative Institute for Resch
in Environmental Sciences
University of Colorado
Boulder, CO 80309

Dr. Thomas C. Bache Jr.
Science Applications Int'l Corp.
10210 Campus Point Drive
San Diego, CA 92121 (2 copies)

Dr. Douglas R. Baumgardt
Signal Analysis & Systems Div.
ENSCO, Inc.
5400 Port Royal Road
Springfield, VA 22151-2388

Dr. S. Bratt
Science Applications Int'l Corp.
10210 Campus Point Drive
San Diego, CA 92121

Dr. Lawrence J. Burdick
Woodward-Clyde Consultants
P.O. Box 93245
Pasadena, CA 91109-3245 (2 copies)

Professor Robert W. Clayton
Seismological Laboratory/Div. of
Geological & Planetary Sciences
California Institute of Technology
Pasadena, CA 91125

Dr. Vernon F. Cormier
Department of Geology & Geophysics
U-45, Roon 207
The University of Conneticut
Storrs, Connecticut 06268

Dr. Zoltan A. Der
ENSCO, Inc.
5400 Port Royal Road
Springfield, VA 22151-2388

Professor John Ferguson
Center for Lithospheric Studies
The University of Texas at Dallas
P.O. Box 830688
Richardson, TX 75083-0688

Professor Stanley Flatte'
Applied Sciences Building
University of California, Santa Cruz
Santa Cruz, CA 95064

Professor Steven Grand
Department of Geology
245 Natural History Building
1301 West Green Street
Urbana, IL 61801

Professor Roy Greenfield
Geosciences Department
403 Deike Building
The Pennsylvania State University
University Park, PA 16802

Professor David G. Harkrider
Seismological Laboratory
Div of Geological & Planetary Sciences
California Institute of Technology
Pasadena, CA 91125

Professor Donald V. Helmberger
Seismological Laboratory
Div of Geological & Planetary Sciences
California Institute of Technology
Pasadena, CA 91125

Professor Eugene Herrin
Institute for the Study of Earth
& Man/Geophysical Laboratory
Southern Methodist University
Dallas, TX 75275

Professor Robert B. Herrmann
Department of Earth & Atmospheric
Sciences
Saint Louis University
Saint Louis, MO 63156

Professor Lane R. Johnson
Seismographic Station
University of California
Berkeley, CA 94720

Professor Thomas H. Jordan
Department of Earth, Atmospheric
and Planetary Sciences
Mass Institute of Technology
Cambridge, MA 02139

Dr. Alan Kafka
Department of Geology &
Geophysics
Boston College
Chestnut Hill, MA 02167

AD-A194 961 FINITE-DIFFERENCE SIMULATIONS OF RAYLEIGH-WAVE 2/2
SCATTERING BY SHALLOW HETE..(U) TELEDYNE GEOTECH
ALEXANDRIA VA ALEXANDRIA LABS K L MCLAUGHLIN ET AL.
UNCLASSIFIED NOV 87 TGAL-87-02 AFGL-TR-87-0322 F/G 8/11 NL

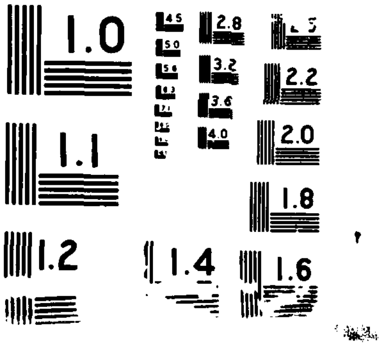
1.0
4.5
5.0
5.6
2.8
3.2
3.6
4.0
2.2
2.0
1.1
1.8
1.2
1.4
1.6

Professor Leon Knopoff
University of California
Institute of Geophysics
& Planetary Physics
Los Angeles, CA 90024

Professor Charles A. Langston
Geosciences Department
403 Deike Building
The Pennsylvania State University
University Park, PA 16802

Professor Thorne Lay
Department of Geological Sciences
1006 C.C. Little Building
University of Michigan
Ann Harbor, MI 48109-1063

Dr. Randolph Martin III
New England Research, Inc.
P.O. Box 857
Norwich, VT 05055

Dr. Gary McCartor
Mission Research Corp.
735 State Street
P.O. Drawer 719
Santa Barbara, CA 93102 (2 copies)

Professor Thomas V. McEvilly
Seismographic Station
University of California
Berkeley, CA 94720

Dr. Keith L. McLaughlin
Teledyne Geotech
314 Montgomery Street
Alexandria, VA 22314

Professor William Menke
Lamont-Doherty Geological Observatory
of Columbia University
Palisades, NY 10964

Professor Brian J. Mitchell
Department of Earth & Atmospheric
Sciences
Saint Louis University
Saint Louis, MO 63156

Mr. Jack Murphy
S-CUBED
A Division of Maxwell Laboratory
11800 Sunrise Valley Drive
Suite 1212
Reston, VA 22091 (2 copies)

Professor Otto W. Nuttli
Department of Earth &
Atmospheric Sciences
Saint Louis University
Saint Louis, MO 63156

Professor J. A. Orcutt
Institute of Geophysics and Planetary
Physics, A-205
Scripps Institute of Oceanography
Univ. of California, San Diego
La Jolla, CA 92093

Professor Keith Priestley
University of Nevada
Mackay School of Mines
Reno, Nevada 89557

Professor Charles G. Sammis
Center for Earth Sciences
University of Southern California
University Park
Los Angeles, CA 90089-0741

Dr. Jeffrey L. Stevens
S-CUBED,
A Division of Maxwell Laboratory
P.O. Box 1620
La Jolla, CA 92038-1620

Professor Brian Stump
Institute for the Study of Earth & Man
Geophysical Laboratory
Southern Methodist University
Dallas, TX 75275

Professor Ta-liang Teng
Center for Earth Sciences
University of Southern California
University Park
Los Angeles, CA 90089-0741

Professor M. Nafi Toksoz
Earth Resources Lab
Dept of Earth, Atmospheric and
Planetary Sciences
Massachusetts Institute of Technology
42 Carleton Street
Cambridge, MA 02142

Professor Terry C. Wallace
Department of Geosciences
Building #11
University of Arizona
Tucson, AZ 85721

Professor Francis T. Wu
Department of Geological Sciences
State University of new York
At Binghamton
Vestal, NY 13901

OCT87

OTHERS (United States)

Dr. Monem Abdel-Gawad
Rockwell Internat'l Science Center
1049 Camino Dos Rios
Thousand Oaks, CA 91360

Professor Shelton S. Alexander
Geosciences Department
403 Deike Building
The Pennsylvania State University
University Park, PA 16802

Dr. Muawia Barazangi
Geological Sciences
Cornell University
Ithaca, NY 14853

Mr. William J. Best
907 Westwood Drive
Vienna, VA 22180

Dr. N. Biswas
Geophysical Institute
University of Alaska
Fairbanks, AK 99701

Dr. G. A. Bollinger
Department of Geological Sciences
Virginia Polytechnical Institute
21044 Derring Hall
Blacksburg, VA 24061

Dr. James Bulau
Rockwell Int'l Science Center
1049 Camino Dos Rios
P.O. Box 1085
Thousand Oaks, CA 91360

Mr. Roy Burger
1221 Serry Rd.
Schenectady, NY 12309

Dr. Robert Burridge
Schlumberger-Doll Resch Ctr.
Old Quarry Road
Ridgefield, CT 06877

Science Horizons, Inc.
ATTN: Dr. Theodore Cherry
710 Encinitas Blvd., Suite 101
Encinitas, CA 92024 (2 copies)

Professor Jon F. Claerbout
Professor Amos Nur
Dept. of Geophysics
Stanford University
Stanford, CA 94305 (2 copies)

Dr. Anton W. Dainty
AFGL/LWH
Hanscom AFB, MA 01731

Professor Adam Dziewonski
Hoffman Laboratory
Harvard University
20 Oxford St.
Cambridge, MA 02138

Professor John Ebel
Dept of Geology & Geophysics
Boston College
Chestnut Hill, MA 02167

Dr. Alexander Florence
SRI International
333 Ravenwood Avenue
Menlo Park, CA 94025-3493

Dr. Donald Forsyth
Dept. of Geological Sciences
Brown University
Providence, RI 02912

Dr. Anthony Gangi
Texas A&M University
Department of Geophysics
College Station, TX 77843

Dr. Freeman Gilbert
Institute of Geophysics &
Planetary Physics
Univ. of California, San Diego
P.O. Box 109
La Jolla, CA 92037

Mr. Edward Giller
Pacific Seirra Research Corp.
1401 Wilson Boulevard
Arlington, VA 22209

Dr. Jeffrey W. Given
Sierra Geophysics
11255 Kirkland Way
Kirkland, WA 98033

Dr. Arthur Lerner-Lam
Lamont-Doherty Geological Observatory
of Columbia University
Palisades, NY 10964

Dr. L. Timothy Long
School of Geophysical Sciences
Georgia Institute of Technology
Atlanta, GA 30332

Dr. George R. Mellman
Sierra Geophysics
11255 Kirkland Way
Kirkland, WA 98033

Dr. Bernard Minster
Institute of Geophysics and Planetary
  Physics, A-205
Scripps Institute of Oceanography
Univ. of California, San Diego
La Jolla, CA 92093

Dr. Geza Nagy
SRI International
333 Ravenswood Avenue
Menlo Park, CA 94025-3493

Dr. Jack Oliver
Department of Geology
Cornell University
Ithaca, NY 14850

Dr. Robert Phinney/Dr. F.A. Dahlen
Dept of Geological
  Geophysical Sci. University
Princeton University
Princeton, NJ 08540 (2 copies)

Professor Paul G. Richards
Lamont-Doherty Geological
  Observatory of Columbia Univ.
Palisades, NY 10964

Dr. Norton Rimer
S-CUBED
A Division of Maxwell Laboratory
P.O. 1620
La Jolla, CA 92038-1620

Professor Larry J. Ruff
Department of Geological Sciences
1006 C.C. Little Building
University of Michigan
Ann Arbor, MI 48109-1063

Dr. Alan S. Ryall, Jr.
Center of Seismic Studies
1300 North 17th Street
Suite 1450
Arlington, VA 22209-2308 (4 copies)

Dr. David G. Simpson
Lamont-Doherty Geological Observ.
  of Columbia University
Palisades, NY 10964

Dr. Bob Smith
Department of Geophysics
University of Utah
1400 East 2nd South
Salt Lake City, UT 84112

Dr. S. W. Smith
Geophysics Program
University of Washington
Seattle, WA 98195

Rondout Associates
ATTN: Dr. George Sutton,
Dr. Jerry Carter, Dr. Paul Pomeroy
P.O. Box 224
Stone Ridge, NY 12484 (4 copies)

Dr. L. Sykes
Lamont Doherty Geological Observ.
Columbia University
Palisades, NY 10964

Dr. Pradeep Talwani
Department of Geological Sciences
University of South Carolina
Columbia, SC 29208

Dr. R. B. Tittmann
Rockwell International Science Center
1049 Camino Dos Rios
P.O. Box 1085
Thousand Oaks, CA 91360

Weidlinger Associates
ATTN: Dr. Gregory Wojcik
620 Hansen Way, Suite 100
Palo Alto, CA 94304

Professor John H. Woodhouse
Hoffman Laboratory
Harvard University
20 Oxford St.
Cambridge, MA 02138

Dr. Gregory B. Young
ENSCO, Inc.
5400 Port Royal Road
Springfield, VA 22151-2388

Dr. Peter Basham
Earth Physics Branch
Geological Survey of Canada
1 Observatory Crescent
Ottawa, Ontario
CANADA K1A OY3

Dr. Eduard Berg
Institute of Geophysics
University of Hawaii
Honolulu, HI 96822

Dr. Michel Bouchon - Universite
Scientifique et Medicale de Grenob
Lab de Geophysique - Interne et
Tectonophysique - I.R.I.G.M-B.P.
38402 St. Martin D'Heres
Cedex FRANCE

Dr. Hilmar Bungum/NTNF/NORSAR
P.O. Box 51
Norwegian Council of Science,
Industry and Research, NORSAR
N-2007 Kjeller, NORWAY

Dr. Michel Campillo
I.R.I.G.M.-B.P. 68
38402 St. Martin D'Heres
Cedex, FRANCE

Dr. Kin-Yip Chun
Geophysics Division
Physics Department
University of Toronto
Ontario, CANADA M5S 1A7

Dr. Alan Douglas
Ministry of Defense
Blacknest, Brimpton,
Reading RG7-4RS
UNITED KINGDOM

Dr. Manfred Henger
Fed. Inst. For Geosciences & Nat'l Res.
Postfach 510153
D-3000 Hannover 51
FEDERAL REPUBLIC OF GERMANY

Dr. E. Husebye
NTNF/NORSAR
P.O. Box 51
N-2007 Kjeller, NORWAY

Tormod Kvaerna
NTNF/NORSAR
P.O. Box 51
N-2007 Kjeller, NORWAY

Mr. Peter Marshall, Procurement
Executive, Ministry of Defense
Blacknest, Brimpton,
Reading FG7-4RS
UNITED KINGDOM (3 copies)

Dr. Ben Menaheim
Weizman Institute of Science
Rehovot, ISRAEL 951729

Dr. Svein Mykkeltveit
NTNF/NORSAR
P.O. Box 51
N-2007 Kjeller, NORWAY (3 copies)

Dr. Robert North
Geophysics Division
Geological Survey of Canada
1 Observatory crescent
Ottawa, Ontario
CANADA, K1A OY3

Dr. Frode Ringdal
NTNF/NORSAR
P.O. Box 51
N-2007 Kjeller, NORWAY

Dr. Jorg Schlittenhardt
Federal Inst. for Geosciences & Nat'l Res.
Postfach 510153
D-3000 Hannover 51
FEDERAL REPUBLIC OF GERMANY

University of Hawaii
Institute of Geophysics
ATTN: Dr. Daniel Walker
Honolulu, HI 96822

Dr. Ramon Cabre, S.J.
c/o Mr. Ralph Buck
Economic Consular
American Embassy
APO Miami, Florida 34032

Professor Peter Harjes
Institute for Geophysik
Rhur University/Bochum
P.O. Box 102148, 4630 Bochum 1
FEDERAL REPUBLIC OF GERMANY

Professor Brian L.N. Kennett
Research School of Earth Sciences
Institute of Advanced Studies
G.P.O. Box 4
Canberra 2601
AUSTRALIA

Dr. B. Massinon
Societe Radiomana
27, Rue Claude Bernard
7,005, Paris, FRANCE (2 copies)

Dr. Pierre Mechler
Societe Radiomana
27, Rue Claude Bernard
75005, Paris, FRANCE

Dr. Ralph Alewine III
DARPA/NMRO
1400 Wilson Boulevard
Arlington, VA 22209-2308

Dr. Peter Basham
Geological Survey of Canada
1 Observatory Creseut
Ottowa, Ontario
CANADA K1A 0Y3

Dr. Robert Blandford
DARPA/NMRO
1400 Wilson Boulevard
Arlington, VA 22209-2308

Sandia National Laboratory
ATTN: Dr. H. B. Durham
Albuquerque, NM 87185

Dr. Jack Evernden
USGS-Earthquake Studies
345 Middlefield Road
Menlo Park, CA 94025

U.S. Geological Survey
ATTN: Dr. T. Hanks
Nat'l Earthquake Resch Center
345 Middlefield Road
Menlo Park, CA 94025

Dr. James Hannon
Lawrence Livermore Nat'l Lab.
P.O. Box 808
Livermore, CA 94550

U.S. Arms Control & Disarm. Agency
ATTN: Mrs. M. Hoinkes
Div. of Multilateral Affairs
Room 5499
Washington, D.C. 20451

Paul Johnson
ESS-4, Mail Stop J979
Los Alamos National Laboratory
Los Alamos, NM 87545

Ms. Ann Kerr
DARPA/NMRO
1400 Wilson Boulevard
Arlington, VA 22209-2308

Dr. Max Koontz
US Dept of Energy/DP 331
Forrestal Building
1000 Independence Ave.
Washington, D.C. 20585

Dr. W. H. K. Lee
USGS
Office of Earthquakes, Volcanoes,
& Engineering
Branch of Seismology
345 Middlefield Rd
Menlo Park, CA 94025

Dr. William Leith
USGS
Mail Stop 928
Reston, VA 22092

Dr. Robert Masse'
Box 25046, Mail Stop 967
Denver Federal Center
Denver, Colorado 80225

Dr. Keith K. Nakanishi
Lawrence Livermore National Laboratory
P.O. Box 808, L-205
Livermore, CA 94550 (2 copies)

Dr. Carl Newton
Los Alamos National Lab.
P.O. Box 1663
Mail Stop C335, Group E553
Los Alamos, NM 87545

Dr. Kenneth H. Olsen
Los Alamos Scientific Lab.
Post Office Box 1663
Los Alamos, NM 87545

Howard J. Patton
Lawrence Livermore National Laboratory
P.O. Box 808, L-205
Livermore, CA 94550

HQ AFTAC/TG
Attn: Dr. Frank F. Pilotte
Patrick AFB, Florida 32925-6001

Mr. Jack Rachlin
USGS - Geology, Rm 3 C136
Mail Stop 928 National Center
Reston, VA 22092

Robert Reinke
AFWL/NTESG
Kirtland AFB, NM 87117-6008

HQ AFTAC/TGR
Attn: Dr. George H. Rothe
Patrick AFB, Florida 32925-6001

Donald L. Springer
Lawrence Livermore National Laboratory
P.O. Box 808, L-205
Livermore, CA 94550

Dr. Lawrence Turnbull
OSWR/NED
Central Intelligence Agency
CIA, Room 5G48
Washington, D.C. 20505

Dr. Thomas Weaver
Los Alamos Scientific Laboratory
Los Almos, NM 97544

AFGL/SULL
Research Library
Hanscom AFB, MA 01731-5000 (2 copies)

Secretary of the Air Force (SAFRD)
Washington, DC 20330
Office of the Secretary Defense
DDR & E
Washington, DC 20330

HQ DNA
ATTN: Technical Library
Washington, DC 20305

Director, Technical Information
DARPA
1400 Wilson Blvd.
Arlington, VA 22209

AFGL/XO
Hanscom AFB, MA 01731-5000

AFGL/LW
Hanscom AFB, MA 01731-5000

DARPA/PM
1400 Wilson Boulevard
Arlington, VA 22209

Defense Technical
Information Center
Cameron Station
Alexandria, VA 22314
(12 copies)

Defense Intelligence Agency
Directorate for Scientific &
Technical Intelligence
Washington, D.C. 20301

Defense Nuclear Agency/SPSS
ATTN: Dr. Michael Shore
6801 Telegraph Road
Alexandria, VA 22310

AFOSR/NPG
ATTN: Major John Prince
Bldg 410, Room C222
Bolling AFB, Wash D.C. 20332

AFTAC/CA (STINFO)
Patrick AFB, FL 32925-6001

END

DATE

FILMED

8-88

DTIC